900-0

SEMI-ANNUAL REPORT

(for July – December 1998)

Contract Number NAS5-31363

OCEAN OBSERVATIONS WITH EOS/MODIS:

Algorithm Development and Post Launch Studies

Howard R. Gordon
University of Miami
Department of Physics
Coral Gables, FL 33124

(Submitted January 1, 1999)

Semi-Annual Report (1 July – 31 December 1998) NAS5–31363

Preamble

As in earlier reports, we will continue to break our effort into six distinct units:

- Atmospheric Correction Algorithm Development
- Whitecap Correction Algorithm
- In-water Radiance Distribution
- Residual Instrument Polarization
- Pre-launch/Post-launch Atmospheric Correction Validation
- Detached Coccolith Algorithm and Post-launch Studies

This separation has been logical thus far; however, as launch of AM-1 approaches, it must be recognized that many of these activities will shift emphasis from algorithm development to validation. For example, the second, third, and fifth bullets will become almost totally validation-focussed activities in the post-launch era, providing the core of our experimental validation effort. Work under the first bullet will continue into the post-launch time frame, driven in part by algorithm deficiencies revealed as a result of validation activities.

An addition to this report is a description of our planned activities for FY99 (Appendix 1). Our next Semi-Annual Report will address the progress made on this plan.

Abstract

Significant accomplishments made during the present reporting period:

- Installed spectral optimization algorithm in the SeaDas image processing environment and successfully processed SeaWiFS imagery. The results were superior to the standard SeaWiFS algorithm (the MODIS prototype) in a turbid atmosphere off the US East Coast, but similar in a clear (typical) oceanic atmosphere.

- Inverted ACE-2 LIDAR measurements coupled with sun photometer-derived aerosol optical thickness to obtain the vertical profile of aerosol optical thickness. The profile was validated with simultaneous aircraft measurements.

- Obtained LIDAR and CIMEL measurements of typical maritime and mineral dust-dominated marine atmosphere in the U.S. Virgin Islands. Contemporaneous SeaWiFS imagery were also acquired.

Semi-Annual Report (1 July – 31 December 1998) NAS5–31363

1. Atmospheric Correction Algorithm Development.

a. Task Objectives:

During CY 1998 there are seven objectives under this task. Objectives (i) and (ii) below are considered to be the most critical. If the work planned under objective (i) is successful, a module that enables the algorithm to distinguish between weakly- and strongly-absorbing aerosols will be included in the atmospheric correction algorithm.

(i) We will continue the study of the "spectral optimization" algorithm. The initial realization of the algorithm will be to provide a flag that will signal the probable presence of absorbing aerosols, and indicate that the quality of the derived products cannot be assured. Later realizations will provide an atmospheric correction in the presence of absorbing as well as nonabsorbing aerosols.

(ii) We need to test the basic implementation of the MODIS atmospheric correction algorithm with actual ocean color imagery. We will do this with SeaWiFS imagery.

(iii) We must implement our strategy for adding the cirrus cloud correction into the existing atmospheric correction algorithm. Specific issues include (1) the phase function to be used for the cirrus clouds, (2) the details of making two passes through the correction algorithm, and (3) preparation of the required tables. These issues will be addressed as time permits in CY 1998.

(iv) The basic correction algorithm yields the product of the diffuse transmittance and the water-leaving reflectance. However, we have shown that the transmittance depends on the angular distribution of the reflectance only when the pigment concentration is very low and then only in the blue. We need to develop a model to include the effects of the subsurface BRDF for low-pigment waters in the blue.

(v) We need to study the efficacy of the present atmospheric correction algorithm for removal of the aerosol effect from the measurement of the fluorescence line height.

(vi) We need to examine methods for efficiently including earth-curvature effects into the atmospheric correction algorithm. This will most likely be a modification of the look-up tables for the top-of-the-atmosphere contribution from Rayleigh scattering.

(vii) We will examine the necessity of implementing out-of-band corrections to MODIS.

b. Work Accomplished:

(i) We consider this task to be one of our most important atmospheric correction activities of 1998 [the other is item (ii) above: testing MODIS algorithms with SeaWiFS imagery], and as such, the major part of our effort on atmospheric correction will be focussed on it. We have implemented the spectral optimization algorithm described by Chomko and Gordon [R. Chomko and H.R. Gordon, Atmospheric correction of ocean color imagery: Use of the Junge power-law aerosol size distribution with variable refractive index to handle aerosol absorption, Applied Optics, 37, 5560-5572 (1998)], in which power-law size distributions are utilized, in the SEADAS image processing environment. The power-law distribution allows a straightforward interpolation to size distributions that are not part of the candidate set. We also interpolate on the real and imaginary parts of the complex refractive index. Thus, a complete spectrum of models can be generated from a relatively small candidate set. We then use standard optimization techniques to find the best fitting set of parameters.

Although incomplete, the first test of the spectral optimization algorithm (SOA) is very encouraging. The figure on the next page compares the performance of the SOA with the NASA standard SeaWiFS algorithm (NSSA) over the Middle Atlantic Bight (MAB) for days 279 and 281 of 1997. The atmosphere over the MAB was very clear on day 281 and the NSSA and SOA yielded comparable phytoplankton pigment concentrations. In contrast, on day 279 the atmosphere over the MAB was very turbid, and there were significant differences between the NSSA- and SOA-derived pigment concentrations. Since the pigment concentration is unlikely to undergo gross changes in the MAB in two days at this time of the year, and since the SOA pigment concentrations are consistent for the two days, while the NSSA concentrations are not, these images suggest a superior performance for the SOA. We are in the process of preparing a detailed report of these results and will included it in the next semi-annual report.

We started a major effort to understand the optical properties of desert dust transported over the oceans. This is being carried out in conjunction with R. Evans. Cyril Moulin has started as a postdoc on the project in August, and is working nearly full time on this problem. The plan is to use SeaWiFS imagery from the Tropical Atlantic acquired this summer, along with the results from the Virgin Islands field experiment (see **5.b.ii**, and Appendix 2), to delineate the dust properties. In addition, we are using imagery from the Mediterranean (closer to the dust source) in conjunction with LIDAR data acquired in Rome.

(ii) We are acquiring SeaWiFS imagery on a regular basis and, with R. Evans, prepared an end-to-end test of the performance of the MODIS algorithm in its present state. To effect this we created a set of SeaWiFS-specific LUTs, but in a format required by the MODIS code. Evans'

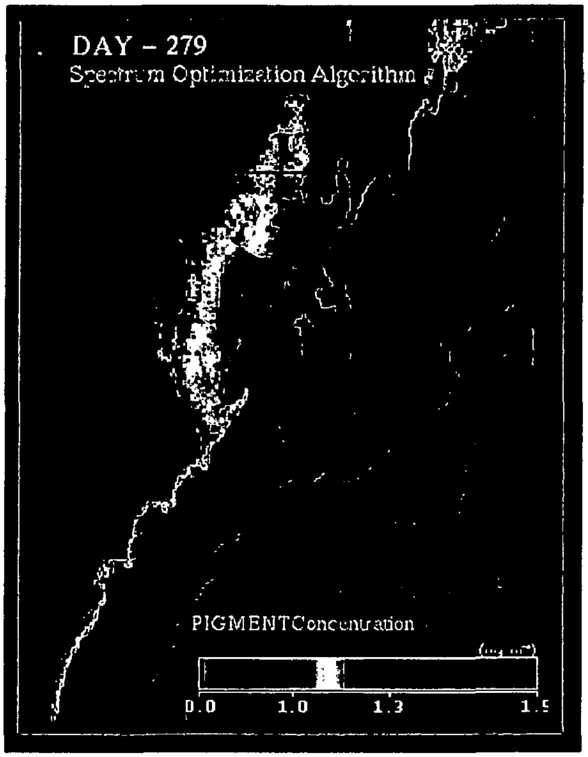
DAY - 279
Spectrum Optimization Algorithm
PIGMENTConcentration
0.0
1.0
1.3
1.5

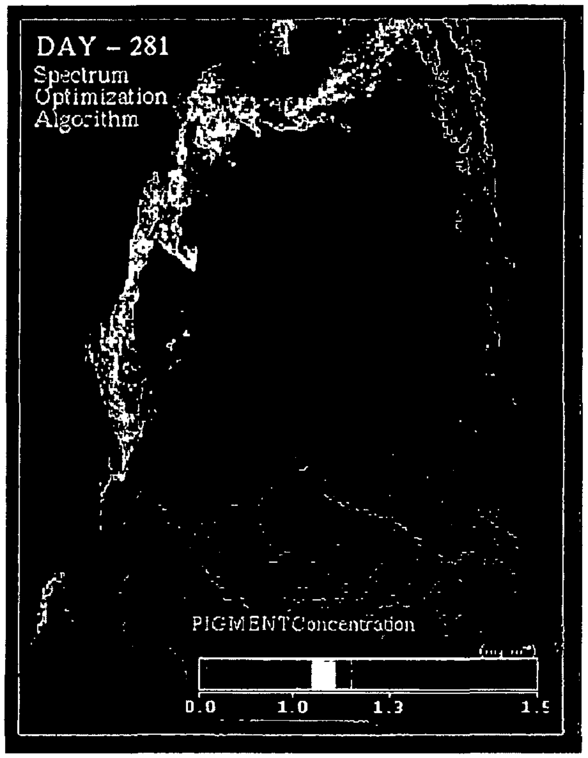
DAY - 281
Spectrum
Optimization
Algorithm
PIGMENTConcentration
0.0
1.0
1.3
1.5

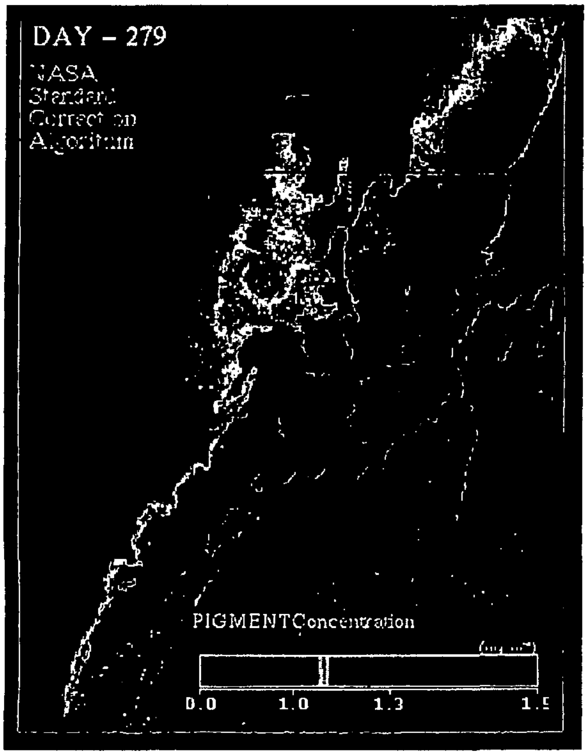
DAY - 279
NASA
Standard
Correction
Algorithm
PIGMENTConcentration
0.0
1.0
1.3
1.5

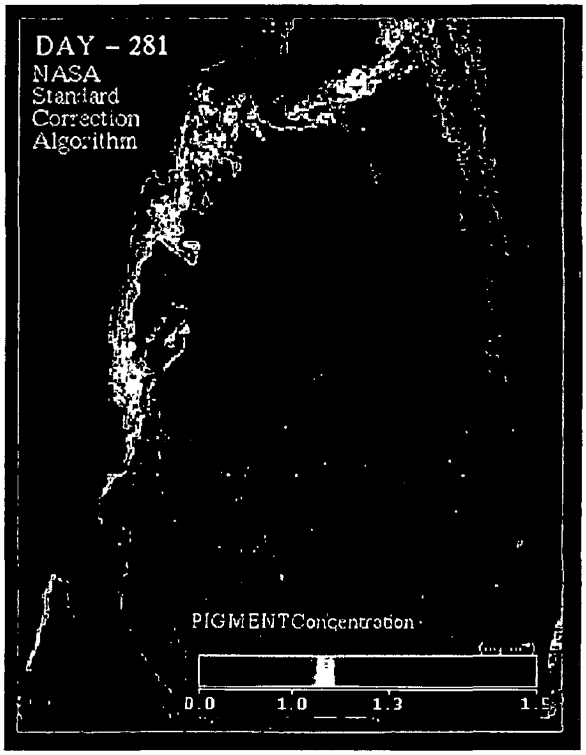
DAY - 281
NASA
Standard
Correction
Algorithm
PIGMENTConcentration
0.0
1.0
1.3
1.5

group has reformated SeaWiFS imagery into the MODIS format, and thus, we can test the MODIS codes using SeaWIFS-simulated MODIS data. Thus far the tests have been successful, i.e., MODIS code running SeaWiFS data in the MODIS format reproduced well the SeaWiFS code processing SeaWiFS data.

(iii) None. In the light of the success of our spectral optimization algorithm, we may have to make significant modifications in our original strategy. This task has been put on hold to free resources for examination of task (i). The issues will be addressed during CY 1999 with the goal of having a post-launch implementation strategy in place during CY 1999.

(iv) We continued the development of an oceanic BRDF model. Specifically, the magnitude of the Raman component has been computed as a function of the pigment concentration.

(v) No work was carried out on this task.

(vi) No work was carried out on this task.

(vii) Now that we have the MODIS relative spectral response (RSR) functions, we have started to incorporate them into the algorithms following the procedures described by Gordon (1995) ["Remote sensing of ocean color: a methodology for dealing with broad spectral bands and significant out-of-band response", Applied Optics, 34 8363-8374 (1995)]. We have computed the band-averaged quantities required to compute the Rayleigh reflectance $[\langle\tau_r(\lambda)\rangle_{F_0S_i}$ and $\langle F_0(\lambda)\rangle_{S_i}$ (See

Table 1: Band-averaged quantities needed to compute the Rayleigh reflectance and the Ozone transmittance for the MODIS bands.

λ (nm)	Band (i)	$\langle\tau_r(\lambda)\rangle_{F_0S_i}$	$\langle F_0(\lambda)\rangle_{S_i}$ mW/cm$^2\mu$m sr	$\langle k_{Oz}(\lambda)\rangle_{F_0S_i}$ ($\times$1000)
412	8	0.3167	170.37	1.47
443	9	0.2377	186.50	3.78
488	10	0.1610	191.82	22.21
531	11	0.1135	188.57	65.66
551	12	0.0999	187.16	83.22
667	13	0.0446	154.15	48.69
678	14	0.0417	149.88	39.95
748	15	0.0286	128.07	12.02
869	16	0.0156	97.30	3.75

Gordon (1995) for the notation)] and the Ozone transmittance $[\langle k_{Oz}(\lambda)\rangle_{F_0 S_i}]$. These are provided in Table 1.

In addition, we examined the influence of the water vapor absorption bands on the computation of the Rayleigh reflectance. For MODIS, the error in ignoring water vapor (up to a concentration of 3.3 g/cm^2) is a maximum of 0.25% (for Band 15). For the other spectral bands, the error is $< 0.1\%$. In contrast, for SeaWiFS the maximum error is 0.55%.

c. Data/Analysis/Interpretation: See item **b** above.

d. Anticipated Future Actions:

(i) We will continue testing the new spectral optimization algorithm using SeaWiFS imagery. In particular, we need to evaluate it with more imagery and different aerosol types. Also, we need to understand the reason for the dramatic improvement of the SOA over the NSSA in the figure following page 4, along with understanding why the performance of the NSSA (the MODIS prototype) is so poor in this case.

(ii) We shall continue testing the prototype MODIS algorithm with SeaWiFS imagery until MODIS imagery becomes available.

(iii) None. The cirrus cloud issue in the presence of our "spectral optimization" method needs to be explored. We will resolve the "spectral optimization" questions first.

(iv) An ocean BRDF model is being tested by comparison with experimental data obtained at the MOBY site and during MOCE-4. This testing will continue into CY 1999. (See **5** below).

(v) None.

(vi) None.

(vii) We will derive the functions needed to incorporate the out-of-band influence on the aerosol component of the atmospheric correction algorithm (Gordon, 1995), and provide LUT's for Rayleigh reflectance that are specific to the MODIS band characteristics.

f. Publications:

R. Chomko and H.R. Gordon, Atmospheric correction of ocean color imagery: Use of the Junge power-law aerosol size distribution with variable refractive index to handle aerosol absorption, *Applied Optics*, **37**, 5560–5572 (1998).

H.R. Gordon, Contribution of raman scattering to water-leaving radiance: A reexamination. (Submitted to *Applied Optics*.)

2. Whitecap Correction Algorithm (with K.J. Voss).

As the basic objectives of the experimental portion of this task have been realized (acquiring whitecap radiometric data at sea), experimental work is being suspended until the validation phase, except insofar as the radiometer is being operated at sea when it is sufficiently important to do so, e.g., the SeaWiFS Initialization Cruise (MOCE-4). Our goal is to maintain experience in operating and maintaining the instrumentation in preparation for the validation phase of the contract. In addition, we need to reanalyze the Tropical Pacific whitecap data because of the surprisingly low reflectance increase due to whitecaps that we measured there. This is a unique data set, as it was acquired in the trade winds with moderately high winds (8-12 m/s) and practically unlimited fetch and duration. This will better bound the limits of oceanic whitecap reflectance.

a. Near-term Objectives:

Operate the radiometer at sea to maintain experience in preparation for the validation phase. Reanalyze data acquired during the Tropical Pacific cruise.

b. Task Progress:

A strategy has been developed that we believe will improve the analysis of the whitecap data; however, the postdoc identified for the reanalysis has accepted a position elsewhere (due to uncertainties in MODIS funding), so no progress has been made on whitecap data analysis of either the Tropical Pacific or MOCE-4 cruises.

c. Data/Analysis/Interpretation: See item b above.

d. Anticipated Future Actions:

We will begin the reanalysis of the Tropical Pacific data with the goal of submitting a revised manuscript on whitecap reflectance by the end of the summer.

e. Publications: None.

3. In-water Radiance Distribution (with K.J. Voss).

a. Task Objectives:

The main objective in this task is to obtain upwelling radiance distribution data at sea for a variety of solar zenith angles to understand how the water-leaving radiance varies with viewing angle and sun angle. This is the experimental component of our BRDF modeling.

b. Work accomplished:

No new measurements were made of oceanic BRDF's during this reporting period.

c. Data/Analysis/Interpretation: None (but see **1.b.(iv)**).

d. Anticipated future actions:

We will be participating in INDOEX during January to April of 1999, as well as the MODIS initalization cruise. Oceanic BRDF's will be included in our suite of measurements. We will concentrate on data analysis after INDOEX.

e. Problems/Corrective actions: None.

f. Publications: None.

4. Residual Instrument Polarization.

The basic question here is: if the MODIS responds to the state of polarization state of the incident radiance, given the polarization-sensitivity characteristics of the sensor, how much will this degrade the performance of the algorithm for atmospheric correction, and how can we correct for these effects?

a. Task Objectives: None.

b. Work Accomplished: None.

c. Data/Analysis/Interpretation: None.

d. Anticipated Future Actions:

This task is now basically complete. All that remains is incorporating the SBRS/MCST polarization-sensitivity data into the existing polarization correction module, when they become available.

e. Problems/Corrective Actions: None

f. Publications: None.

5. Pre-launch/Post-launch Atmospheric Correction Validation (with K.J. Voss).

a. Task Objectives:

The long-term objectives of this task are four-fold:

(i) First, we need to study aerosol optical properties over the oceans to assess the applicability of the aerosol models used in the atmospheric correction algorithm. Effecting this required obtaining long-term time series of the aerosol optical properties in typical maritime environments. This was achieved using a CIMEL sun/sky radiometer. This radiometer is identical to those used in the AERONET Network (in which we are a participant).

(ii) Second, we must be able to measure the aerosol optical properties from a ship during the initialization/calibration/validation cruises. The CIMEL-type instrumentation could not be used (due to the motion of the ship) for this purpose. The required instrumentation consisted of an all-sky camera (which can measure the entire sky radiance, with the exception of the solar aureole region) from a moving ship, an aureole camera (specifically designed for ship use) and a hand-held sun photometer.

In the case of strongly-absorbing aerosols, we have shown that knowledge of the aerosol vertical structure is critical. Thus, we need to be able to measure the vertical distribution of aerosols during validation exercises as well as to build a climatology of the vertical distribution of absorbing aerosols. This is accomplished with a LIDAR system, which we have modified for ship operations. This LIDAR is also needed to detect the presence (or absence) of thin cirrus during the initialization/calibration/validation cruises.

(iii) The third objective was to determine how accurately the radiance at the top of the atmosphere can be determined based on measurements of sky radiance and aerosol optical thickness at the sea surface. This required a critical examination of the effect of radiative transfer on "vicarious" calibration exercises.

(iv) The forth objective is to utilize data from other sensors that have achieved orbit (OCTS, POLDER, SeaWiFS ...) to validate and fine-tune the correction algorithm.

b. Work Accomplished:

(i) We have been operating the CIMEL instrument in the Dry Tortugas continuously during most of 1998. It has worked well (even surviving Hurricane Georges). These data are avaliable as part of AERONET, and have been used by others to study the validity of aerosol retrievals with SeaWiFS, e.g., Wang et al., "Remote sensing of the aerosol optical thickness from SeaWiFS in comparison with insitu measurements," Submitted to APLS99, 18-22 Jan., 1999, Meribel, France.

(ii) The Micro Pulse Lidar (MPL) along with a CIMEL were deployed in the U.S. Virgin Islands during June and July 1998 to try to observe the vertical distribution and optical properties of Saharan dust. Successful observations were made during both dust and dust-free periods. A report describing the experiment is provided in Appendix 2. We had to have the MPL unit repaired (it failed after the Virgin Islands experiment) and have procured a spare power supply to ensure against similar failures in the winter-spring INDOEX experiment. The unit is now back in Miami being prepared for INDOEX.

Aureole and sky camera data acquired during the MOCE-4 cruise are still being reduced. A paper describing our aureole camera has been prepared and submitted for publication to *JAOT*. It is included as Appendix 3.

(iii) The theoretical aspects of this work have been completed. The next phase is to use surface measurements to predict top-of-atmosphere radiance.

(iv) We have prepared a duplicate version of the MODIS algorithm code to use the SeaWiFS spectral bands. This is being used to test the MODIS code with SeaWiFS data. (See Section **1-ii.**)

c. Data/Analysis/Interpretation:

(i) A paper based on a long-term study of aerosols over the ocean has been submitted to *JGR* and is included here as Appendix 4. It confirms the notion that high aerosol optical thicknesses over the Tropical Atlantic and Caribbean are almost always due to mineral dust.

(ii) Preliminary analysis of our MPL data from the U.S. Virgin Islands deployment is provided in Appendix 2.

Analysis of the data resulting from our participation in ACE-2 (June-July 1997) is nearly complete, and several publications are being prepared. Our main contribution was in providing calibrated MPL and CIMEL data to delineate the vertical distribution of the aerosol and the optical properties. Appendix 5 is a draft of a paper comparing our MPL prediction of the vertical distribution of the aerosol optical depth with direct aircraft measurements. It is being submitted to a special issue of *Tellus* devoted to ACE-2. As far as we know, this is the first such successful comparison. It shows that the profile of optical depth can be retrieved from the MPL given surface optical depth measurements, e.g., by a sun photometer.

d. Anticipated Future Actions:

(i) We will continue to keep the CIMEL operating in the Dry Tortugas, including the monthly maintenance checks.

(ii) Our main focus will be our participation in INDOEX. Reduction of the data from the Virgin Islands, as well as MOCE-4 will be suspended until the end of INDOEX.

(iii) We attempt to use data acquired during MOCE-4 (once the analysis is complete) to effect the vicarious calibration SeaWiFS Band 8 (865 nm).

(iv) See Section **1.d.(ii)**

e. Problems/corrective actions: None.

f. Publications:

A. Smirnov, B. Holben, I. Slutsker, E.J. Welton, and P. Formenti, "Optical properties of Saharan dust during ACE 2," *Jour. Geophys. Res.*, **103D** 28,079–28,092 (1998).

E.J. Welton, K.J. Voss, D.L. Savoie, and J.M. Prospero, "Measurements of Aerosol Optical Depth over the North Atlantic Ocean: Correlations with Surface Aerosol Concentrations" (Submitted to *Jour. Geophys. Res.*).

J.M. Ritter and K.J. Voss, " A new instrument to measure the solar aureole from an unstable platform." (Submitted to *Jour. Atmos. Ocean. Tech.*).

B. Schmid, P.B. Russell, J.M. Livingston, S. Gasso, D.A. Hegg, D.R. Collins, R.C. Flagan, J.H. Seinfeld, E. Ostrom, K.J. Noone, P.A. Durkee, H.H. Jonsson, E.J. Welton, K.J. Voss, H.R. Gordon, P. Formenti, M.O. Andreae, V.N. Kapustin, T.S. Bates, and P.K. Quinn, "Clear column closure studies of urban-marine and mineral-dust aerosols using aircraft, ship, and ground-based measurements in ACE-2," (Submitted to ALPS99, 18–22 January 1999, Meribel, France).

B. Schmid, J.M. Livingston, P.B. Russell, P.A. Durkee, H.H. Jonsson, D.R. Collins, R.C. Flagan, J.H. Seinfeld, S.A. Gasso, D.A. Hegg, E. Ostrom, K.J. Noone, E.J. Welton, K.J. Voss, H.R. Gordon,

P. Formenti, and M.O. Andreae, "Clear sky closure studies of lower tropospheric aerosol and water vapor during ACE-2 using airborne sunphotometer, airborne in-situ, space-borne, and ground-based measurements." (To be submitted to *Tellus* Special Issue on ACE-2)

E.J. Welton, K.J. Voss, H.R. Gordon, H. Maring, A. Smirnov, B. Holben, B. Schmid, J.M. Livingston, P.B. Russell, P.A. Durkee, P. Formenti, and M.O. Andreae, "Ground-based Lidar Measurements of Aerosols During ACE-2: Instrument Description, Results, and Comparisons with other Ground-based and Airborne Measurements." (To be submitted to *Tellus* Special Issue on ACE-2)

6. Detached Coccolith Algorithm and Post Launch Studies (W.M. Balch).

a. Task Objectives:

Our MODIS work during involves understanding all aspects of the influence of suspended calcium carbonate particles on inherent optical properties in the sea. Work during this reporting period focused on several areas: processing cell count samples; merging atomic absorption data, particulate organic carbon data, and scattering data from MODIS pre-launch cruises in the Gulf of Maine; preparation, submission, or revision of three MODIS-related manuscripts; participating in another MODIS pre-launch cruise to the Gulf of Maine to examine in situ properties of calcite particle; and analysis of calcite optical properties from the Arabian Sea.

The algorithm for retrieval of the detached coccolith concentration from the coccolithophorid, E. huxleyi is described in detail in our ATBD. The key is quantification of the backscattering coefficient of the detached coccoliths. Our earlier studies focused on laboratory cultures to understand factors affecting the calcite-specific backscattering coefficient. A thorough understanding of the relationship between calcite abundance and light scattering, in situ, will provide the basis for a generic suspended calcite algorithm. As with algorithms for chlorophyll, and primary productivity, the natural variance between growth related parameters and optical properties needs to be understood before the accuracy of the algorithm can be determined. To this end, the objectives of our coccolith studies during this reporting period have been:

(1) Working up data from our June '98 MODIS Gulf of Maine cruise.

(2) Final pre-publication formatting of JGR manuscript on coccolith scattering properties.

(3) Continued microscope cell/coccolith counts for latest samples from the Gulf of Maine.

(4) Final publication of a paper on coccolith optical properties (with Ken Voss and Katherine Kilpatrick.

(5) Completion of 11 one-day pre-launch cruises in the Gulf of Maine in which samples for coccolith concentration, suspended calcium carbonate and optical properties of these particulates were enumerated.

For perspective on the directions of our work, we provide an overview of our previous activities:

Jan-June 1995: Research focus – chemostat cultures (in which algal growth rate was precisely controlled) and we examined how the optical properties of these calcifying algae changed as a function of growth.

July-Dec 1995: Research focus – shipboard measurements of suspended calcite and estimates of optical backscattering as validation of the laboratory measurements. We participated on two month-long cruises to the Arabian Sea, measuring coccolithophore abundance, production, and optical properties.

Jan-June 1996: Research focus – field calcite distributions, during two Gulf of Maine cruises, one in March and one in June.

July-Dec 1996: Research focus – participated on another cruise to the Gulf of Maine and processed samples from the Gulf of Maine.

Jan-June 1997: Research focus – continued processing samples from our previous cruises, upgraded our laser light scattering photometer used in all of the calcite scattering measurements, performed another pre-launch cruise on calcite particle optics in the Gulf of Maine, and analyzed our results from the MODIS-funded flow cytometer work.

July-December 1997: Research focus – continued building our data base on calcite-dependent scattering with a cruise to the Gulf of Maine in November 1997. Work was also performed on processing the data from the June 1997 cruise. The results from the flow cytometer work were submitted for publication.

Jan-June 1998: Research focus – worked-up results from our November '97 Cruise, participated in a pre-launch cruise in June '98, finalized data merging and processing for all previous cruises, integrated the data stream for surface radiance into the suite of optical parameters which we measure [which was one of the issues from our MODIS ATBD review that was suggested for connecting the inherent optical properties (which we measure) to the water-leaving radiance (which the satellite will measure)]. Lastly, we put considerable time into preparation and publishing of earlier results.

b. July-December 1998:

We completed work-up of our June 1998 cruise in the Gulf of Maine aboard the R/V Albatross. As with the November 1997 cruise, calcite-dependent backscattering commonly accounted for 10-20% of total backscattering. Even with the low light conditions, coccolithophores were still remarkably abundant in the Gulf of Maine. We formerly interpreted strong coccolith influence on particle optics as a "summer-only" issue but it now can be clearly considered a year-round phenomenon. Specifically, we encountered a coccolith patch in 8°C water SW of Nova Scotia. This is the last place we ever expected to see coccolithophores, given the strong mixing and cool temperatures. Since we collected AC-9 data of absorption and attenuation (which by difference gave us scattering), then we have been processing the data to calculate $\tilde{b}_b$ (the backscattering probability b_b/b) and see how this varies with the standing stock of chlorophyll and calcium carbonate.

Given the future plan for more Gulf of Maine cruises, as well as our SIMBIOS activities, we have written new software to merge the various data sets into one file that can be submitted to NASA's SeaBass data archive. The software (which performs vicarious calibrations, offset corrections, plus calculating "derived quantities" has now been through 3 sets of revisions to streamline it and make it more efficient. This software will considerably reduce the time currently required to quality control the numbers and produce hydrographic plots of the inherent optical properties (a, b, c, b_b, calcite-dependent backscattering, $\tilde{b}_b$, temperature, salinity, and fluorescence).

c. Data/Analysis/Interpretation: See **b.**

d. Anticipated Future Actions:

Work in the next reporting period will address several areas:

(1) Suspended calcite analyses from the Gulf of Maine cruise series.

(2) Publication of *JGR* manuscript on coccolith scattering properties (January 1999 issue).

(3) Completion of a cruise in the Gulf of Mexico, doing a line between Tampa and Progresso, Mexico, followed by a trip up the entire eastern U.S., back to the Gulf of Maine (March and April 1999). This will be a one month campaign.

(4) Continuation of microscope cell/coccolith counts for latest samples from the Gulf of Maine, and Gulf of Mexico.

(5) Utilization of 20 more days at sea in the Gulf of Maine during the summer and fall of 1999.

e. Problems/Corrective Actions: None

f. Publications:

Voss, K., W. M. Balch, and K. A. Kilpatrick, "Scattering and attenuation properties of Emiliania huxleyi cells and their detached coccoliths," *Limnol. Oceanogr.* **43** 870–876 (1998).

Balch, William M., David T. Drapeau, Terry L. Cucci, and Robert D. Vaillancourt, Katherine A. Kilpatrick, Jennifer J. Fritz. "Optical backscattering by calcifying algae-Separating the contribution by particulate inorganic and organic carbon fractions," *Jour. Geophys. Res.* (In press).

Milliman, J., P.J. Troy, W. Balch, A.K. Adams, Y.-H. Li, and F.T. MacKenzie, "Biologically-mediated dissolution of calcium carbonate above the chemical lysocline?" *Deep Sea Res.* (In press).

Graziano, L., W. Balch, D. Drapeau, B. Bowler, and S. Dunford, "Organic and inorganic carbon production in the Gulf of Maine" *Cont. Shelf Res.* (Submitted).

Balch, W. M., D. Drapeau, J. Fritz, and B. Bowler, "Calcification rates in the Arabian Sea," Submitted to *Deep Sea Res.* Special Issue on the Arabian Sea (Submitted).

7. Other Activities.

The PI participated in the MODIS Science Team meeting at University of Maryland (December 15 and 16, 1998). He also presented the following papers at scientific meetings.

H.R. Gordon, K.J. Voss, J.W. Brown, P.V.F. Banzon, R.E. Evans, D.K. Clark, L. Kovar, M. Yuen, M. Feinholz, and M. Yarbrough, SeaWiFS Calibration Initalization: Preliminary Results. *Ocean Optics XIV*, Kona, Hawaii, November 11-13, 1998.

H.R. Gordon, The NIMBUS-7 Coastal Zone Color Scanner: A Retrospective. Invited paper, American Geophysical Union Fall Meeting, San Francisco, CA, December 6-10, 1998.

8. Publications and Submissions 1998.

H.R. Gordon, Vicarious calibration of ocean color sensors, *Remote Sensing of Environment*, **63**, 265–278 (1998).

H. Yang and H.R. Gordon, Retrieval of the Columnar Aerosol Phase Function and Single Scattering Albedo from Sky Radiance over Land: Simulations, *Applied Optics*, **37**, 978–997 (1998).

K.D. Moore, K.J. Voss, and H.R. Gordon, Spectral reflectance of whitecaps: Instrumentation, calibration, and performance in coastal waters, *Jour. Atmos. Ocean. Tech.*, **15**, 496–509 (1998).

D.J. Diner, J.C. Beckert, T.H. Reilly, C.J. Bruegge, J.E. Conel, R.A. Kahn, J.V. Martonchik, T.P. Ackerman, R. Davies, G.A.W. Gerstl, H.R. Gordon, J-P. Muller, R. Myneni, P.J. Sellers, B. Pinty, and M.M. Vestraete, Multi-angle Imaging SpectroRadiometer (MISR) Instrument Description and Experiment Overview, *IEEE Transactions on Geoscience and Remote Sensing*, **36**, 1072–1087 (1998).

J.V. Martonchik, D.J. Diner, R.A. Kahn, T.P. Ackerman, M.M. Verstrate, B. Pinty, and H.R. Gordon, Techniques for the Reetrieval of Aerosol Properties Over Land and Ocean Using Multiangle Imaging, *IEEE Transactions on Geoscience and Remote Sensing*, **36**, 1212–1227 (1998).

W.E. Esaias, M.R. Abbott, Otis B. Brown, J.W. Campbel, K.L. Carder, D.K. Clark, R.L. Evans, F.E. Hoge, H.R. Gordon, W.M. Balch, R. Letelier, and P. Minnett, An overview of MODIS capabilities for ocean science observations, *IEEE Transactions on Geoscience and Remote Sensing*, **36**, 1250–1265 (1998).

J.V. Martonchik, D.J. Diner, B. Pinty, M.M. Verstrate, R.B. Myneni, Y. Knyazikhim, and H.R. Gordon, Determination of Land and Ocean Reflective, Radiative, and Biophysical Properties Using Multiangle Imaging, *IEEE Transactions on Geoscience and Remote Sensing*, **36**, 1266-1281 (1998).

R. Chomko and H.R. Gordon, Atmospheric correction of ocean color imagery: Use of the Junge power-law aerosol size distribution with variable refractive index to handle aerosol absorption, *Applied Optics*, **37**, 5560–5572 (1998).

Voss, K., W. M. Balch, and K. A. Kilpatrick, "Scattering and attenuation properties of Emiliania huxleyi cells and their detached coccoliths," *Limnol. Oceanogr.* **43** 870–876 (1998).

A. Smirnov, B. Holben, I. Slutsker, E.J. Welton, and P. Formenti, "Optical properties of Saharan dust during ACE 2," *Jour. Geophys. Res.*, **103D** 28,079–28,092 (1998).

Balch, William M., David T. Drapeau, Terry L. Cucci, and Robert D. Vaillancourt, Katherine A. Kilpatrick, Jennifer J. Fritz. "Optical backscattering by calcifying algae-Separating the contribution by particulate inorganic and organic carbon fractions," *Jour. Geophys. Res.* (In press).

Milliman, J., P.J. Troy, W. Balch, A.K. Adams, Y.-H. Li, and F.T. MacKenzie, "Biologically-mediated dissolution of calcium carbonate above the chemical lysocline?" *Deep Sea Res.* (In press).

H.R. Gordon, Contribution of raman scattering to water-leaving radiance: A reexamination. (Submitted to *Applied Optics.*)

E.J. Welton, K.J. Voss, D.L. Savoie, and J.M. Prospero, "Measurements of Aerosol Optical Depth over the North Atlantic Ocean: Correlations with Surface Aerosol Concentrations" (Submitted to *Jour. Geophys. Res.*).

B. Schmid, P.B. Russell, J.M. Livingston, S. Gasso, D.A. Hegg, D.R. Collins, R.C. Flagan, J.H. Seinfeld, E. Ostrom, K.J. Noone, P.A. Durkee, H.H. Jonsson, E.J. Welton, K.J. Voss, H.R. Gordon, P. Formenti, M.O. Andreae, V.N. Kapustin, T.S. Bates, and P.K. Quinn, "Clear column closure studies of urban-marine and mineral-dust aerosols using aircraft, ship, and ground-based measurements in ACE-2," (Submitted to ALPS99, 18–22 January 1999, Meribel, France).

J.M. Ritter and K.J. Voss, " A new instrument to measure the solar aureole from an unstable platform." (Submitted to *Jour. Atmos. Ocean. Tech.*).

Graziano, L., W. Balch, D. Drapeau, B. Bowler, and S. Dunford, "Organic and inorganic carbon production in the Gulf of Maine" *Cont. Shelf Res.* (Submitted).

Balch, W. M., D. Drapeau, J. Fritz, and B. Bowler, "Calcification rates in the Arabian Sea," Submitted to *Deep Sea Res.* Special Issue on the Arabian Sea (Submitted).

B. Schmid, J.M. Livingston, P.B. Russell, P.A. Durkee, H.H. Jonsson, D.R. Collins, R.C. Flagan, J.H. Seinfeld, S.A. Gasso, D.A. Hegg, E. Ostrom, K.J. Noone, E.J. Welton, K.J. Voss, H.R. Gordon, P. Formenti, and M.O. Andreae, "Clear sky closure studies of lower tropospheric aerosol and water vapor during ACE-2 using airborne sunphotometer, airborne in-situ, space-borne, and ground-based measurements." (To be submitted to *Tellus* Special Issue on ACE-2)

E.J. Welton, K.J. Voss, H.R. Gordon, H. Maring, A. Smirnov, B. Holben, B. Schmid, J.M. Livingston, P.B. Russell, P.A. Durkee, P. Formenti, and M.O. Andreae, "Ground-based Lidar Measurements of Aerosols During ACE-2: Instrument Description, Results, and Comparisons with other Ground-based and Airborne Measurements." (To be submitted to *Tellus* Special Issue on ACE-2)

APPENDIX 1

NASA/GSFC Contract No. NAS5-31363

OCEAN OBSERVATIONS WITH EOS/MODIS
Algorithm Development and Post Launch Studies

Howard R. Gordon
University of Miami
Department of Physics
Coral Gables, FL 33124

Plans for FY 99

Preamble

The coming Fiscal Year (1999) was to be heavily focused on validation of MODIS-derived products. However, the delay of the launch of EOS AM1 requires some modification of the plan. Our approach for the coming year is to use SeaWiFS for *validating algorithms* (rather than MODIS-derived products) in a manner similar to the way the MODIS Land and Atmospheres Groups have already been using the MAS. In addition, the delay in the launch will allow us additional time to enhance the already existing algorithms prior to launch.

We break our effort for FY 99 into five distinct (although interrelated) units:

- Atmospheric Correction Algorithm Development
- Whitecap Correction Algorithm
- In-water Radiance Distribution (BRDF)
- Pre-launch/Post-launch Atmospheric Correction Validation
- Detached Coccolith Algorithm

In what follows, it will be seen that addressing the various tasks within these units requires fundamental studies, a through examination of SeaWiFS imagery, use of SeaWiFS imagery as a tool, and a maintenance of measurement and data-analysis capability through the prelaunch era into the formal validation phase. Developing the required capability of, and experience in, processing SeaWiFS imagery will also facilitate the efficient handling of MODIS imagery (e.g., for QA) in the post-launch era.

Atmospheric Correction Algorithm Development

Objectives and Proposed Activities (FY '99)

During FY '99 there are several objectives under this task. They are focused on ensuring the correctness of the basic correction algorithm and its implementation, improving the basic algorithm to provide for an accurate correction in the presence of strongly-absorbing aerosols, and addressing several MODIS-specific issues.

1. Validate/Improve the Basic MODIS Algorithm using SeaWiFS

We will begin the algorithm validation and improvement process using SeaWiFS imagery.

As we have been able to successfully process SeaWiFS imagery (reformatted to MODIS) using our MODIS code, we can be assured that the implementation is correct. Thus, we will concentrate on the science of the correction algorithm by using SeaWiFS to validate the water-leaving radiances and indicate any potential problems and potential improvements. For example, we have found using SeaWiFS data acquired during the "initialization" cruise in January and February of 1998, that using the 670-865 nm bands (the "6-8" algorithm) resulted in a somewhat better atmospheric correction than using the 765-865 nm bands (the "7-8" algorithm). This has important implications for MODIS, because it uses an algorithm that is similar to the 7-8 algorithm in SeaWiFS. However, the SeaWiFS band at 765 nm overlaps the O_2 "A" absorption band, while the corresponding MODIS band (748 nm) avoids it. Thus, we need to know whether the better performance of the 6-8 compared to 7-8 algorithm of SeaWiFS is due to the O_2 "A" band, or a more fundamental problem that could have an impact on MODIS.

2. Implement and Test the "Spectral Matching Algorithm"

We will continue our basic study of the "spectral matching" algorithm. Unlike the basic MODIS algorithm, the spectral matching algorithm has the potential for atmospheric correction in the presence of strongly-absorbing aerosols.

The spectral matching algorithm [Gordon *et al.*, "Remote sensing ocean color and aerosol properties: resolving the issue of aerosol absorption," *Applied Optics*, **36**, 8670-8684 (1997); Chomko and Gordon, "Atmospheric correction of ocean color imagery: Use of the Junge power-law aerosol size distribution with variable refractive index to handle aerosol absorption," *Applied Optics*, **37**, 5560-5572 (1998)] has already been implemented in an image processing environment. We will test its efficacy and document its performance (compared to the basic MODIS algorithm) using SeaWiFS imagery in regions in which the aerosol properties may be highly variable on a day-to-day basis, but the water properties are reasonably stable, e.g., the Middle Atlantic Bight (MAB) or the Tropical Atlantic and Caribbean. Our focus will be as complete an assessment as possible, so a decision can be made concerning its replacement of, or inclusion in, the basic MODIS algorithm. At a minimum, it will be used to provide a flag in the MODIS algorithm that will signal the probable presence of absorbing aerosols, and indicate that the quality of the derived products cannot be assured. However, the long-term goal is that it replace the basic algorithm.

3. Optical Properties of Wind-Blown Dust

We need quantitative estimates of the optical properties of wind-blown dust, e.g., from Africa, to provide a proper model to effect atmospheric correction using the standard MODIS algorithm.

The optical properties of wind-blown dust are required to effect atmospheric correction using the standard MODIS algorithm, and possibly the spectral matching algorithm as well. We have a unique opportunity now to use SeaWiFS imagery that was acquired over the Caribbean this year's particularly intense dust periods of July and August, simultaneous with our surface measurements of the aerosol vertical profile (using LIDAR) and aerosol optical thickness (using a CIMEL sun/sky radiometer) made from St. Johns, VI, to develop a model for African dust.

4. MODIS-Specific Issues

We need to address the detection and removal of thin cirrus clouds, methods for efficiently including earth-curvature effects, out-of-band corrections, BRDF effects on the diffuse *transmittance, correct for polarization sensitivity of MODIS, and the efficacy of atmospheric correction for removal of the aerosol effect from the measurement of the fluorescence line height.*

Of the issues listed under this heading, the first that we will pursue is the MODIS out-of-band corrections. As we now have the MODIS relative spectral response (RSR) functions from MCST, we can complete their incorporation into the algorithms following the procedures described by Gordon (1995) ["Remote sensing of ocean color: a methodology for dealing with broad spectral bands and significant out-of-band response", *Applied Optics*, **34**, 8363-8374 (1995)].

The second is incorporating the SBRS/MCST polarization-sensitivity data into the atmospheric correction module. This will be effected as described in Gordon, *et al.*, (1997) ["Atmospheric Correction of Ocean Color Sensors: Analysis of the Effects of Residual Instrument Polarization Sensitivity," *Applied Optics*, **36**, 6938-6948 (1997)].

The third issue to be examined is the BRDF effect. As described below (In-water Radiance Distribution), we propose to use our measurements of the BRDF to develop a model that can be applied to MODIS imagery. This model will be used to address the BRDF on the diffuse transmittance.

The forth issue in importance is efficiently including earth-curvature effects in the MODIS algorithm. Following Ding and Gordon ["Atmospheric correction of ocean color sensors: Effects of earth curvature," *Applied Optics,* **33**, 7096-7106 (1994)] this will most likely be a modification of the look-up tables for the top-of-the-atmosphere contribution from Rayleigh scattering. However, before actually embarking on an implementation, we will examine SeaWiFS imagery at high latitudes to assess the impact of neglecting earth-curvature in the algorithm.

Finally, because of uncertainty in the performance of MODIS Band 26, and because we need to assess whether our radiative transfer codes are sufficiently accurate to study removal of the aerosol effect from the measurement of the fluorescence line height, we will examine this issue and thin cirrus clouds only if time permits.

An updated Algorithm Theoretical Basis Document (ATBD) for the Normalized Water Leaving Radiance algorithm will be prepared and submitted by April 30, 1999.

Whitecap Correction Algorithm

Objectives and Proposed Activities (FY '99)

Our basic goal for the rest of the project is to maintain experience in operating and maintaining the instrumentation in preparation for the validation phase of the contract, and to complete the analysis of the whitecap data acquired thus far.

5 Maintaining Measurement Capability

We need to maintain our ability to make whitecap measurements.

The basic objectives of the experimental portion of this task has been realized (acquiring whitecap radiometric data at sea), experimental work is being suspended until the validation phase, except insofar as the radiometer is being operated at sea when it is sufficiently important to do so, e.g., it was operated during the SeaWiFS Initialization Cruise (MOCE-4). This requires personnel capable of both maintaining and operating the instrumentation.

6. Reduction and Analysis of Existing Data

We need to complete the analysis of the data already acquired.

We have a significant amount of whitecap data that is yet to be reduced and analyzed. In addition, we need to reanalyze the Tropical Pacific whitecap data because of the surprisingly low reflectance increase due to whitecaps that we measured there. This is a unique data set, as it was acquired in the trade winds with moderately high winds (8-12 m/s) and practically unlimited fetch and duration. We have now developed an alternative method of analysis that we believe is more robust and will provide greater confidence in the results. Earlier this year, the SeaWiFS Project informed us that the present whitecap algorithm was causing the atmospheric correction algorithm to fail in the South Atlantic. We provided an algorithm adjustment (based on our earlier analysis of the Tropical Pacific whitecap data), and were informed by them that the algorithm appeared to be working much better after the adjustment. This example underscores the importance of *a detailed examination of as much SeaWiFS imagery as possible prior to the launch of MODIS.*

In-water Radiance Distribution (BRDF)

Objectives and Proposed Activities (FY '99)

During FY '99 our objectives for this task are: maintaining experience in operating and maintaining the instrumentation in preparation for the validation phase of the contract; acquiring more field data; and using the field data to develop a model of the BRDF as a function of the solar zenith angle and the water's chlorophyll concentration.

7. Maintaining Measurement Capability

We need to maintain our ability to make BRDF measurements.

This requires personnel capable of both maintaining and operating the instrumentation, as well as reducing the data.

8. Acquisition of More Field Data

To build and thoroughly test a BRDF model, we need to acquire data over a wider range of chlorophyll concentrations.

We will operate the Radiance Distribution Camera System (RADS) whenever the opportunity to acquire data over a wider range of chlorophyll concentrations presents itself. For example, we plan to participate in INDOEX in the Indian Ocean in January-February 1999. This will also provide an independent data set for validation of the MODIS algorithm using SeaWIFS. We will, of course, participate in the MODIS initialization cruise.

9. Build a BRDF Model

We need to develop a model relating the subsurface radiance distribution (BRDF) to the chlorophyll concentration of the water

The data acquired during the SeaWiFS initialization cruise showed that, at a solar zenith angle of ~37° (the mean encountered during the cruise) and a chlorophyll concentration of ~ 0.1 mg/m^3 (the approximate mean encountered during the cruise), an error of ~5% in the normalized water-leaving radiance $[L_w(\lambda)]_N$ would be made if the measurement was carried out at nadir rather than at the angle appropriate to the viewing direction of the sensor. Since most investigators are only capable of measuring the in-water upwelling radiance at nadir, direct comparison of their measurements with MODIS (or SeaWiFS) data will result in an error at, or above, the level of error that is acceptable for the MODIS product. This error can be reduced by using a model (based on the chlorophyll concentration and solar zenith angle) to either correct the nadir measurement to the appropriate viewing angle, or to correct the MODIS product to provide the normalized water-leaving radiance *at nadir*. In either case, a model is required and we propose to build one that includes both elastic and inelastic (Raman) scattering, as it is evident that a considerable portion of the radiance in the blue-green (>10%) results from inelastic processes. In addition we will compare our measurements with the f/Q model of Morel [Morel and Gentili, "Diffuse reflectance of oceanic waters. III. Implication of bidirectionality for the remote sensing problem," *Applied Optics*, **35**, 4850--4862 (1996)] (which is being used in other models in the community). Construction of such a model may require that the in-water light field be simulated with a radiative transfer code that includes polarization.

Pre-launch/Post-launch Atmospheric Correction Validation

Objectives and Proposed Activities (FY '99)

The original objectives of this task were fourfold: (1) study aerosol optical properties over the oceans to assess the applicability of the aerosol models proposed for use in the atmospheric correction algorithm; (2) measure the aerosol optical properties (including their vertical distribution) from a ship during the initialization/calibration/validation cruises; (3) determine how accurately the radiance at the top of the atmosphere can be estimated based on measurements of sky radiance and aerosol optical thickness at the sea surface (i.e., vicarious calibration); and (4) utilize data from other sensors that have achieved orbit (OCTS, POLDER, SeaWiFS ...) to validate and fine-tune the correction algorithm. We have obtained a significant amount of data toward (1), designed, constructed, or purchased, instrumentation to acquire data for (2), completed (3), and (4) was discussed under the first activity above (Atmospheric Correction Algorithm Development). Objectives for the post-launch validation phase are: maintain experience in operating and maintaining the instrumentation in preparation for the validation phase of the contract; complete analysis of data already acquired; and participate in the validation phase.

10. Maintaining Measurement Capability

We need to maintain our ability to make atmospheric measurements at sea.

This requires personnel capable of both maintaining and operating the instrumentation, as well as reducing the data. We will continue to keep the CIMEL operation in the Dry

Tortugas, including the monthly maintenance checks. We plan to use the MPL, aureole camera, and sky camera during INDOEX in January-February of 1999, and during the MODIS initialization cruise.

11. Complete Analysis of Existing Data

We need to complete the analysis of the data acquired previously.

We have been operating the CIMEL instrument in the Dry Tortugas almost continuously for several years. It worked well, largely due to the diligence of E.J. Welton in maintaining the instrument and the site. However, we have only scratched the surface in the data analysis. We have only looked at a few specific time periods, and need to examine the entire record. In particular, there are several periods when African dust was known to be present, and we can study its properties using the CIMEL data. Also, we have extracted specific days of the data set, believed to be dust, marine aerosol, or nonseasalt sulfate aerosols. On these days we are running our inversion method [Wang and Gordon, "Retrieval of the Columnar Aerosol Phase Function and Single Scattering Albedo from Sky Radiance over the Ocean: Simulations," *Applied Optics*, **32**, 4598-4609 (1993)] for recovering the phase function, to compare with that used by Nakajima *et al.* ["Retrieval of the Optical Properties of Aerosols from Aureole and Extinction Data," *Applied Optics*, **22**, 2951--2959 (1983)], used in the Aeronet Network). This work will be continuing.

Aureole and sky camera data acquired during the July Hawaii criuse are being analyzed, specifically for several locations while the cruise went near the volcanic plume to look at the retrieved size distribution of particulates in the plume. The aureole and sky cameras (including the sky polarization) were also operated during the MOCE-4 cruise, and these data are in the process of being reduced and analyzed as part of the SeaWiFS initialization.

12. Post-launch Validation

We will participate in MODIS post-launch validation.

We will use the MPL, aureole camera, and sky camera during INDOEX in January-February of 1999. In this case, SeaWiFS will be a surrogate for MODIS in the algorithm validation program. We will also participate in the MODIS initialization cruise; however, its scheduling will be dependent on the MODIS launch.

Detached Coccolith Algorithm

Objectives and Proposed Activities (FY '99)

The objectives of our FY 99 effort are to complete analysis of cruise work done to date, continue new field data in the Gulf of Maine and Gulf of Mexico, use these data to improve algorithm performance and to apply and validate the coccolithophore algorithm using SeaWiFS data.

13. Processing of completed pre-launch cruises

We have been collecting data on coccolith concentrations in several pre-launch cruises per year for the past several years. Most analyses have now been performed, and post-cruise calibrations of the scattering measurements have been done (calibration standards are always run before each cruise, but periodic distilled water checks are always run, and must be checked against published values to verify calibration). While basic

APPENDIX 2

Report:
U.S. Virgin Islands Summer 1998 Research Trip
Study of the optical properties of Saharan dust over the ocean

Period of Study: 7-15-98 to 8-12-98

Ellsworth Judd Welton
Post-doctoral Research Associate
University of Miami - Physics Department
1320 Campo Sano Dr.
Coral Gables, Fl 33146
(305)-284-2325 ext 3

1. Introduction

I conducted a field measurement program from July 15, 1998 to August 12, 1998 at the Virgin Islands Environmental Resource Station (VIERS) at Lameshur, St. John, USVI. The purpose of the program was to study the optical properties of airborne particles in the atmosphere (aerosols). Aerosols directly effect the climate by scattering and absorbing sunlight in the atmosphere and indirectly cause climate effects by serving as cloud condensation nuclei [*Russell et al.*, 1997]. Aerosols also interfere with the remote sensing of the earth's surface from satellite sensors because the signals from the surface must pass through the aerosol layers.

I am funded to provide information on the optical properties of aerosols over the ocean in order to correct satellite images of the ocean color. Ocean color measurements are made to determine biologically important ocean parameters, such as the concentration of chlorophyll *a* in a given body of water. The presence of aerosol layers over the water must be accounted for when analyzing the satellite data to insure an accurate analysis is made [*Gordon*, 1997]. In particular, I was measuring two of the key optical properties of aerosols. The first property is referred to as the aerosol optical depth (AOD) and is a measure of the amount of direct sunlight attenuated by the aerosol layers. The spectral dependence of the AOD throughout the visible and near-infared wavelengths also gives information on the size distribution of the aerosols [*Van de Hulst*, 1981]. The second property I was measuring was the vertical profile of the aerosol extinction coefficient (AEC). The AEC is the amount of sunlight scattered and absorbed per unit length by the aerosols. Knowledge of the AEC and also the altitude of the aerosol layers is vital for correct analysis of the ocean color data [*Gordon*, 1997].

The VIERS site was chosen because it is on a small, remote island that is largely free of urban influence and is one of the few easily accessible locations for the study of aerosols over the open ocean. In addition, the primary aerosol species I was interested in studying was Saharan dust. Saharan dust is transported across the Atlantic Ocean during the summer and early fall months [*Prospero*, 1995] and the Virgin Islands are ideally situated to study the dust as it moves across the Atlantic. The influx of Saharan dust perturbs the regional climates of the Caribbean and the Southeastern United States. Also, dust aerosols are difficult to incorporate into satellite correction analysis since there is little historical data on their optical properties. In addition, dust aerosols are often irregular in shape and normal analysis routines that make use of spherical particle assumptions for optical calculations produce inaccurate results [*Mishchenko et al.*, 1997]. *In-situ* data on the real optical properties of dust aerosols over the ocean is needed for the validation and correction analysis of the ocean color measurements.

This report will describe the VIERS site and discuss the instrumentation I deployed during the measurement program. I will also present data that identifies the presence of dust aerosols as well as reasonably clear days and also the altitude of the respective aerosol layers. Finally, I will discuss the measured AOD and AEC profiles of both clear and dusty periods and relate them to data taken during this period using the NASA SeaWiFS ocean color sensor [*Hooker et al.*, 1992] currently in orbit.

2. Site and Instrumentation Descriptions

VIERS [*VIERS*, www site, 1998] is located at 18.32° N latitude and 64.73° W longitude and includes a marine laboratory located on Great Lameshur Bay and a living area (campground) located a short distance inland from the bay. The elevation of the lab and the campground varies within just a few meters of sea-level, thus for the purposes of this program all data was analyzed assuming an altitude of 0 km. VIERS is bordered to the north (inland) by tall hills of maximum altitude approximately 380 m but has a relatively unobstructed view (within a few meters of sea-level) to the east and southeast (windward). VIERS is located well within the boundaries of the Virgin Islands National Park and its remote location insures that little to no urban aerosols are present.

I deployed three instruments at VIERS during the measurement program. The first two instruments were sunphotometers which are used to measure the AOD and it's spectral dependence. A hand-held sunphotometer was used for the first two weeks, and an automatic sky scanning sunphotometer (Cimel) was used for the remainder of the program. The Cimel [*Holben et al.*, 1994] was not functioning during the first two weeks of the program due to problems with it's motor. The Cimel sunphotometer is shown in Figure 1 while operating on the VIERS lab roof.

Figure 1

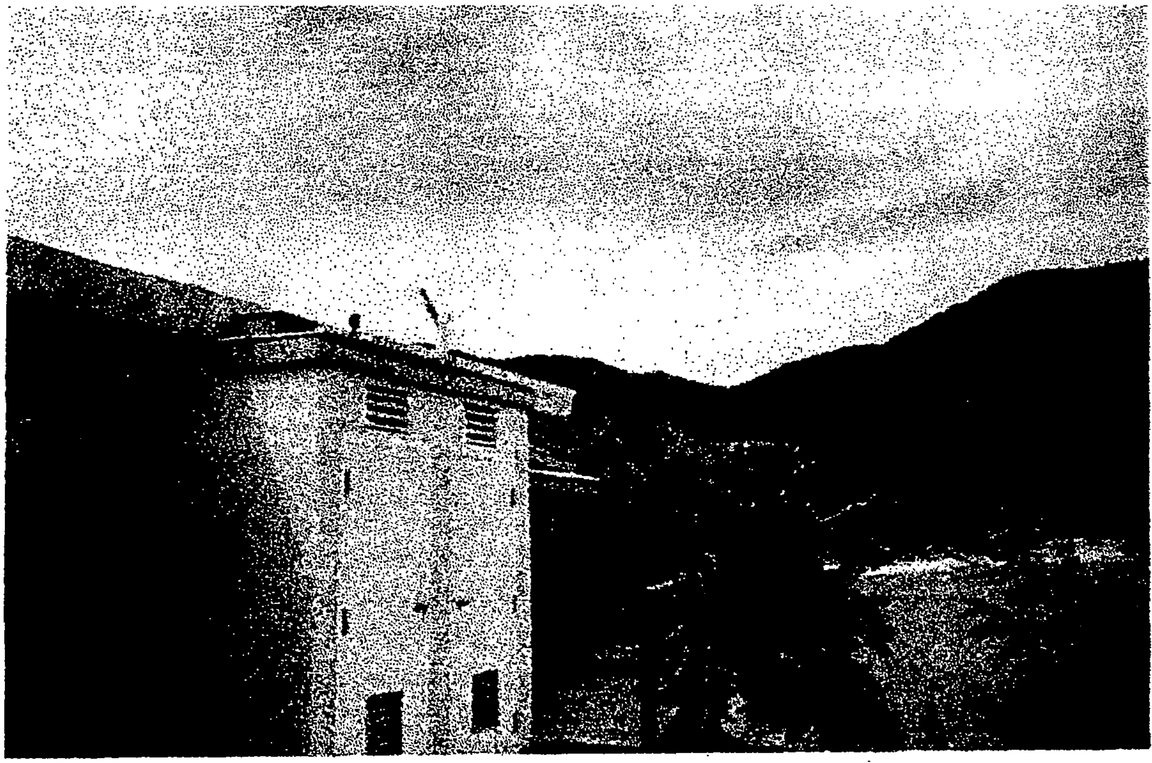

Figure 1. The Cimel sunphotometer is shown operating on the roof of the VIERS lab. The Cimel is the gray tube pointing skyward from the top of the roof.

The other instrument was a micro-pulse lidar system [*Spinhirne et al.*, 1995] and is shown in Figure 2 while operating at the VIERS campground. The lidar was used to acquire the vertical profiles of the AEC and AOD. The lidar operated throughout the program. However, a problem developed during the first week and resulted in condensation forming on the mirror surfaces of the lidar transmitter-receiver (T-R). Massive condensation on the mirrors prevents successful operation of the lidar, therefore a lidar data was only taken during periods relatively free of visible mirror condensation.

Figure 2

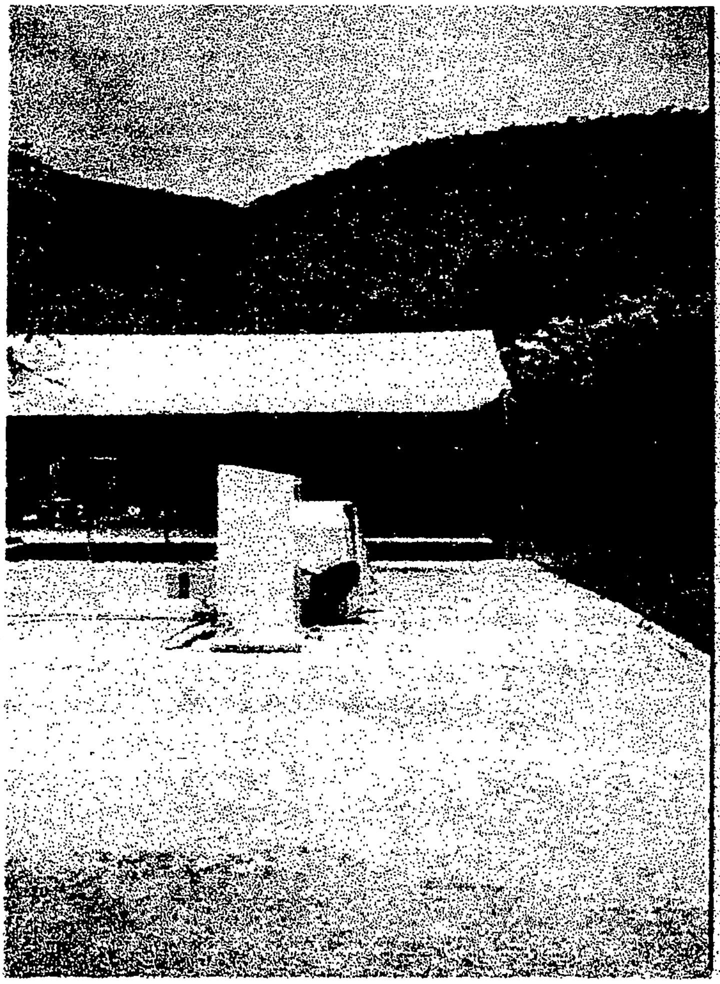

Figure 2. The lidar system is shown operating at the VIERS campground.

3. Cimel and Lidar Data

The data acquired with the Cimel was processed by the AERONET [*NASA-a*, www site, 1998] group at NASA Goddard Space Flight Center and then supplied to me. The Cimel measured the spectral dependence of the AOD from July 29, 1998 to August 8, 1998. This AOD data was used to identify dust dominant periods from clean (normally only sea-salt aerosols) periods using criteria I developed in my Ph.D. dissertation [*Welton*, 1998]. Analysis of the Cimel AOD data as well as a few hand-held sunphotometer AOD measurements has shown that July 27, August 6, and August 8 were clean days free of dust, while July 29, July 31, and August 1 were days with moderate to heavy dust. Consultation of my notes from these days also shows both clean and hazy visual conditions on the appropriate days.

The lidar data acquired on the clean and dusty days mentioned above was analyzed to determine the vertical profile of the AEC at times coincident with the Cimel measurement. The AOD measured with the Cimel was used to calculate the AEC profiles from the lidar data using an algorithm I had developed in my Ph.D. dissertation [*Welton*, 1998]. The best coincident Cimel and lidar data was available on August 1 for the dusty days and August 8 for the clean days. These days were chosen based on overlapping Cimel and lidar measurement times as well as the absence of cirrus clouds (identification of cirrus clouds is possible by inspection of the lidar data) which falsely increase the AOD. The AEC profiles and AOD are shown in Figure 3 for August 1 and August 8.

Figure 3

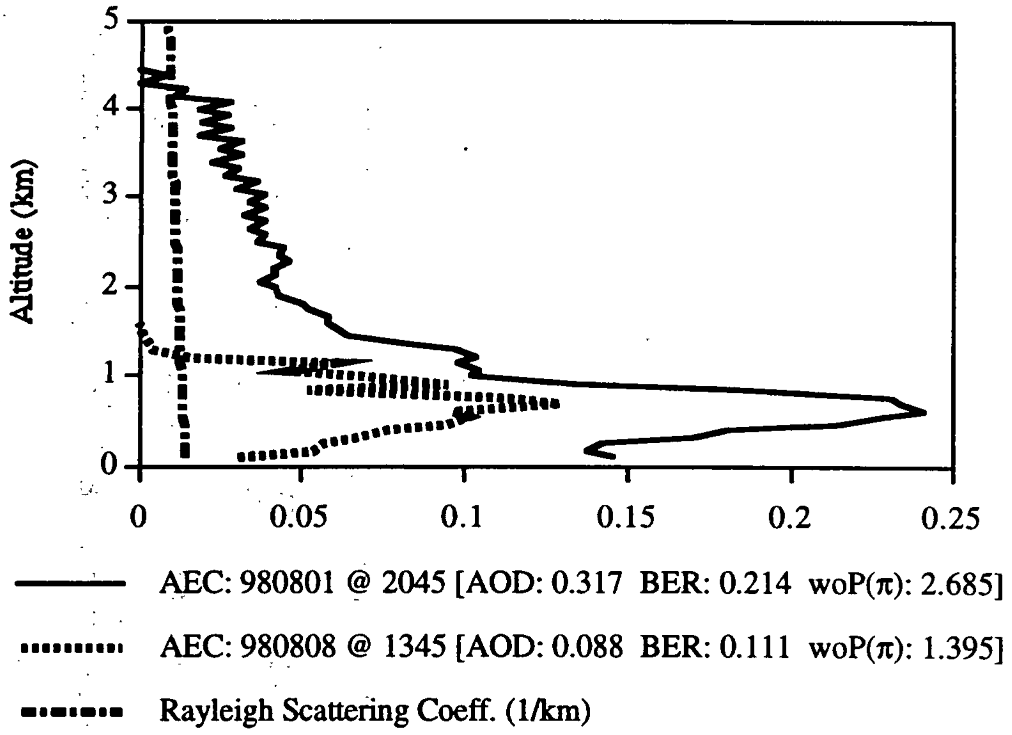

Figure 3. AEC profiles for the August 1 dust period (980801) and the August 8 clean period (980808). The profile due to molecular scattering (Rayleigh) is shown for comparison. The AOD measured on each day is given in the brackets.

The AEC values obtained during the dust period on August 1 are much greater than those measured during clean conditions on August 8. Also, the August 1 AEC values are the same magnitude as dust AEC values I obtained with the lidar during the Aerosol Characterization Experiment 2 (ACE-2) in Tenerife, Canary Islands in 1997. The Figure also shows the clean August 8 aerosols to be confined to a narrow layer extending to only just over 1 km in altitude. However, during the dusty August 1 period the aerosols are seen to extend to 4 km in altitude. Most of the aerosols are located in the boundary layer on this day, but a clear dust layer above the boundary layer is evident.

The AEC values (at each individual altitude) in each profile may not be highly accurate based on the backscatter-extinction ratio (BER) calculated for each profile. The

BER values for both the clean and dusty profiles are quite high and this is usually caused by incorrect AOD values input to the algorithm or a BER values that are not constant with altitude. The Cimel instrument is highly calibrated at the Goddard facility thus the AOD values are most likely correct. The best assumption is that the BER was not constant with altitude during both of these profiles. This was probably less likely with the clean profile as the BER is much closer to values that would be expected for spherical sea-salt particles. Despite possible error in the calculated AEC values, the altitude of the aerosol layers remains unaffected. Thus the altitude range of the clean and dusty periods is accurate and useful information.

4. *In-situ* Results and SeaWiFS Measurements

SeaWiFS data was acquired on August 1 and August 8 for the area surrounding and including the U.S. Virgin Islands. The SeaWiFS data presented here was provided by the NASA Goddard SeaWiFS web site [*NASA-b*, www site, 1998]. Figures 4 and 5 show composite visible wavelength satellite images taken by SeaWiFS over the VIERS site on August 1 and August 8 respectively. Dust is visible in the images as the brown color, clouds appear as white, and clear portions of sky are blue due to the ocean surface. Also, sunglitter from the ocean surface is present in the middle portion of each image and unfortunately encompasses the VIERS site in Figure 4. However, Figure 4 clearly shows the VIERS site to be under a large dust layer on August 1 that extends far south of the island as much of this portion of the image is most likely dust due to its hazy distinctive brown color. Conversely, Figure 5 shows the VIERS site to be under clear sky save for clouds to the northeast and southwest; dust is visible far to the south of the site on this day.

Figure 4

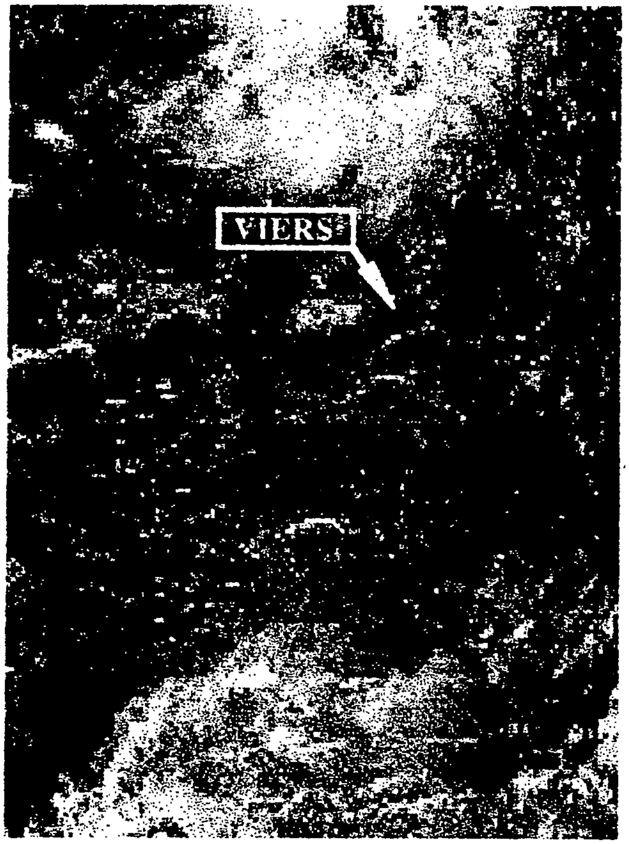

Figure 4. SeaWiFS visible image showing the VIERS site under a large dust layer. Dust appears brown, clouds white, and clear sky portions are blue due to the ocean surface. Sunglitter, present in the middle portion of the image, appears as a gray-like color.

Figure 5

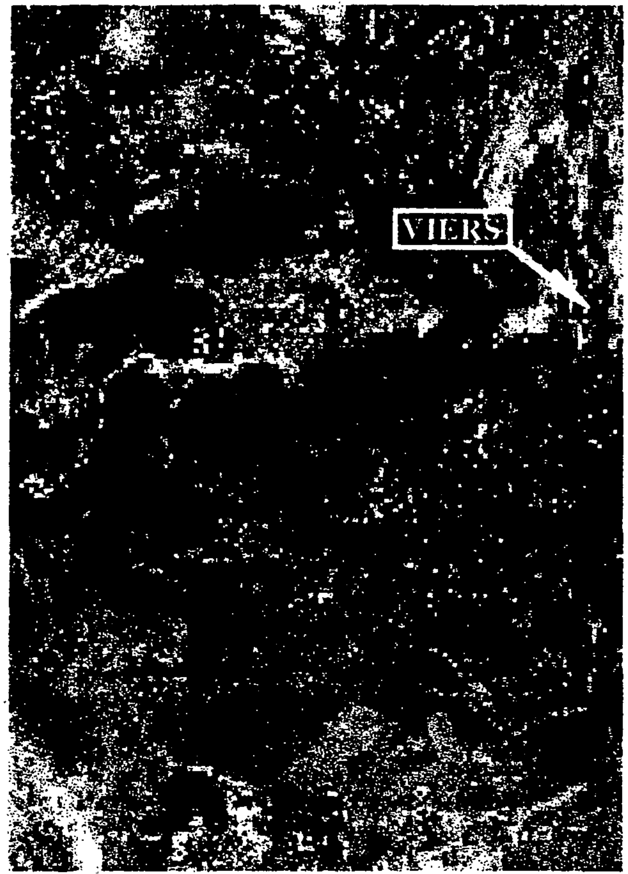

Figure 5. SeaWiFS visible image on August 8 showing the VIERS site under clear sky although surrounded by clouds to the northeast and southwest. Dust appears brown, clouds white, and clear sky portions are blue due to the ocean surface. Sunglitter, present in the middle portion of the image, appears as a gray-like color.

5. Conclusion

The data *in-situ* data obtained at the VIERS site will be used to help develop a better understanding of the impact of dust aerosols on the ocean color analysis performed on the SeaWiFS images shown above. In particular, the data I gathered at the VIERS site will aid in constructing more accurate models of dust properties for use in the analysis of satellite data. Also, the information I gathered on the background sea-salt aerosol properties will add to my previously obtained sea-salt data and aid in the understanding of future measurements of aerosol optical properties over the ocean. Finally, this trip has shown that the VIERS site is well suited to the study of Saharan dust aerosols over the open ocean. The data and experience I acquired during this measurement program will aid any possible future aerosol related work in the Virgin Islands area.

Acknowledgments

I would like to thank Randy Brown and Bobby Agostini at VIERS for much help in setting up my equipment during the program and for making my stay pleasant and enjoyable. I would also like to thank Albert Chapin for the design and construction of the lidar climate containers. I am also grateful to Brent Holben and the NASA-GSFC AERONET network for loaning me the Cimel sunphotometer and performing analysis of the Cimel data. I also gratefully acknowledge the support of the National Park Service and the Virgin Islands National Park for allowing me to conduct my research. Finally, I am thankful to receive support from the NASA contract #NA55-31363.

References

Gordon, H.R., Atmospheric correction of ocean color imagery in the Earth Observing System era, *J. Geophys. Res.*, 102, 17081-17106, 1997.

Holben, B.N., T.F. Eck, I. Slutsker, D. Tanre, J.P. Buis, A. Setzer, E. Vermote, J.A. Reagan, Y.J. Kaufman, T. Nakajima, and F. Lavenu, Multi-band automatic sun and sky scanning radiometer system for measurement of aerosols, *Proc. Sixth International Symposium Physical on Measurements and Signatures in Remote Sensing*, 75-83, 1994.

Mishchenko, M.I., L.D. Travis, R.A. Kahn, and R.A. West, Modeling phase functions for dust-like tropospheric aerosols using a shape mixture of randomly oriented polydisperse spheroids, *J. Geophys. Res.*, 102, 16831-16847, 1997.

NASA-a, *www site*, http://spamer.gsfc.nasa.gov/, 1998.

NASA-b, *www site*, http://seawifs.gsfc.nasa.gov/scripts/SEAWIFS.html, 1998.

Prospero, J.M., Saharan dust transport over the north Atlantic Ocean and Mediterranean, Chapter in*The Impact of Desert Dust From Northern Africa Across the Mediterranean*, Kluwer Academic Publishers, Oristano, Sardinia, 1995.

Russell, P.B., S.A. Kinne, and R.W. Bergstrom, Aerosol climate effects: Local radiative forcing and column closure experiments, *J. Geophys. Res.*, 102, 9397-9407, 1997.

Spinhirne, J.D., J. Rall, and V.S. Scott, Compact eye-safe lidar systems, *Rev. Laser Eng.*, 23, 26-32, 1995.

Van de Hulst, H. C., *Light Scattering by Small Particles*, Dover Publications Inc., New York, NY, 1981.

VIERS, *www site*, http://www.islands.org/virgin/viers/, 1998.

Welton, E. J., Measurements of Aerosol Optical Properties Over the Ocean Using Sunphotometry and Lidar, *Ph.D. Dissertation*, University of Miami, Physics Department, 1320 Campo Sano Dr., Coral Gables, Fl, 33146.

APPENDIX 3

A new instrument to measure the solar aureole from an unstable platform

Joseph M. Ritter and Kenneth J. Voss

Physics Department, University of Miami

Coral Gables, Fl. 33124

305 284 2323 ext 2

fax 305 284 4222

voss@physics.miami.edu

Abstract

A new instrument is described which can measure the sky radiance distribution near the solar disk even when operated on an unstable platform. An imaging detector is used to image the sky around the sun, while an occulter on a long pole blocks out the direct solar radiation. The occulter has a Neutral Density filter in the center which places an image of the solar disk in each image. This allows accurate directional information to be obtained, eliminates possible ambiguities about the angular position of the data, and increases the accuracy of the measurement. A special triggering device aids in making these measurements on a ship. This instrument will be used in field studies of atmospheric aerosols and in satellite validation campaigns.

1. Introduction

Aerosols (solid and liquid particles suspended in the atmosphere) play an important role in determining the Earth's radiation budget (and hence its climate), as well as influencing the chemical composition of the gaseous atmosphere. Aerosols can affect the Earth radiation budget both directly (by scattering and absorbing solar and terrestrial radiation) and indirectly (by modifying cloud properties through their role as cloud condensation nuclei). Unfortunately the global impact of the aerosols optical effects are not well understood. In fact, the uncertainty in the aerosol radiative forcing is larger than the uncertainty in climate forcing by all greenhouse gases released over the past century (Houghton, et al. 1995). To reduce this uncertainty, improved measurements of the aerosol optical properties are needed for aerosol and climate field studies.

In addition, aerosol optical properties must be understood to interpret satellite observations of the earth's surface since much of the signal received by a satellite is caused by the intervening aerosols. Thus to validate remote satellite measurements of ocean and land properties we need to improve our understanding of the aerosols optical properties.

The solar aureole is the region of enhanced brightness surrounding the sun caused by the scattering of light by aerosols. Radiometric measurements of the solar aureole, when combined with spectral extinction data, can yield data products such as the aerosol size distribution and the aerosol scattering phase function for small scattering angles (Nakajima et al. 1983; Nakajima et al. 1996). For vicarious calibration of ocean color satellite sensors it is desirable to make these measurements at sea (Clark et al. 1997). At sea, platform motion coupled with the large dynamic range of the aureole radiance requires an instrument with a high signal-to-noise ratio, accurate pointing, fast triggering, short exposure times, low jitter, as well as sensor stability.

An imaging radiometer meeting these requirements has been developed and will be described. The imaging nature of the instrument allows measurement of sky radiance within one degree of the center of the solar disk even when deployed on an unstable platform such as a ship.

2. Instrument Description

Previous successful approaches to solar aureole radiometry have involved scanning radiometers on stable platforms (Holben et al. 1996). A new approach was required for shipborne operation where platform motion interferes with the scanning motion. Our approach uses an electronic camera to acquire the circumsolar sky radiance in a single image. Use of a camera ensures accurate direction registration, while modern CCD cameras have the dynamic range necessary for measuring the aureole.

The system components are illustrated in Fig. 1. In brief, the system employs a cooled 512x512 CCD array, 35 mm lens and filter wheel, internal and external cooling system, and sun alignment sensor with associated triggering and digitizing electronics. This package is mounted on a 2m pole and pointed manually toward the sun where an occulter mounted on the end of the pole attenuates the direct sunlight and completely shadows the camera aperture. A sun alignment sensor on the system automatically exposes the CCD when the camera orientation is correct. Instrument control and data acquisition is performed by a remote desktop computer. At this time the instrument components will be described in detail.

a. Occulter

The camera aperture is shadowed by the solar occulter so that scattered radiation entering the aperture is a minimum of 1/2 degree from the instrument optical axis. The solar disk itself subtends a half-angle of 1/4 degree at the instrument. The center of the occulter is a neutral density filter. The attenuated image of the solar disk, when combined with ephemeris data, can be used to determine the azimuth and zenith coordinates corresponding to each CCD pixel.

b. Filter Wheel

After the occulter, the first optical element the light entering the system encounters is the filter wheel housing window. This window is coated with an antireflection coating, and has a 1 cm clear inside diameter. Inside the filter wheel housing, 10 nm interference filters centered at 440, 560, 670, and 860 nm are used to limit the spectral bandpass of the instrument. The filter wheel and housing provides an effective light seal with its neighboring components without significantly extending the optical path. Since this system is only looking at a narrow angular range around the sun, the variation in bandpass of the filters with angular position is negligible (<1%).

Each interference filter is paired with a neutral density filter to optimally utilize the available dynamic range of the sensor. Each spectral channel response is adjusted for near saturation at 1.0 degree from the center of the solar disk with the exception of the 440 nm channel. The low system response at 440 nm would have required longer exposure times to achieve this level and lead to potential blurring effects caused by platform motion.

c. Lens

After passing through the interference and neutral density filters the light enters a camera lens. The current lens system is a standard 35 mm lens with a 50 mm focal length stopped at f/15. With this lens, the instrument has an angular resolution of 0.05 degrees and a field of view of +/- 7.5 degrees centered on the sun.

d. Shutter

An electromechanical shutter is employed in this system. A computer controlled integration and shuttering system ensures low integration time jitter (<10μs) while exposing rapidly enough (19 msec) to eliminate image blur due to ship motion. The uncertainty in the retrieval of absolute radiance data is directly proportional to the uncertainty in the time the shutter is open from one exposure to the next. Quantitative assessment of jitter, and other calibration issues are addressed in the next section.

e. Pointing and triggering

An essential feature for shipborne applications is a unique sun-sensing trigger device that trips the shutter only when suitable alignment of the sun with the instrument optical axis is achieved. The trigger developed for this instrument consists of a long, baffled collimating tube with a window and neutral density filter at one end, and a photodiode amplifier package at the other. The axis of the tube is aligned parallel to the optical axis of the aureolemeter. When the tube (and thus the aureolemeter) is aligned with the sun, the photodiode is activated and a pulse is generated. The pulse is amplified and shaped, then used to trigger the shutter. This scheme allows measurement of the aureole to within 1 degree of the edge of the solar disk even when deployed on an unstable platform such as a ship.

f. Detector

A commercially available camera (Spectrasource MCD-1000) is used as the image detector. The CCD array used is a 512-by-512 array (TK512). Double correlated sampling digitizes individual pixels at 16 bit resolution. This system provides a signal to noise ratio of 10^3, with dark noise variation less than 11 counts. The array temperature is actively servo-controlled by Peltier cooling. An external cooling system was constructed to help draw additional heat from the instrument, and to ensure sensor stability in field deployments.

g. Data acquisition and control

A Macintosh desktop computer is employed to control data acquisition as well as primary data reduction. Software was written to provide a menu driven user interface, and control image digitization, storage, shuttering as well as perform field diagnostics. Interrupt routines are written in native assembly language to accommodate strict timing requirements. The software incorporates a control loop allowing complete remote system operation by the experimenter, usually located outdoors with the sensor 50 to 100 feet from the control system. Complementary instruments are employed to provide optical depth, measurement location, ambient pressure, humidity and temperature data.

3. Instrument Calibration and Characterization

There are several calibration steps required to convert the camera output into calibrated sky radiance data. In addition, the electro-optical system must be characterized to understand the performance limitations of the system. These steps are now detailed.

a. Angular Calibration

Angular calibration is required to determine the mapping between the image location on the array focal plane and the corresponding angle in real space. This was done in two ways. In one test an object was imaged at a known distance. The angular subtence of the object was calculated, and this was used to calibrate the angular field of the image. The result was then verified by placing the instrument on a precision rotary table, imaging a point source, and then acquiring an image. The camera was then rotated by a known angle and another image acquired. This was done for angles from 0 to 7 degrees. The pixel displacement of the light source in the image was then determined and agreed with the displacement expected from the first test to within 0.05 degrees. Each pixel covers a 0.05 degree wide (full angle) field of view.

b. Dark Signal

There are several components of the dark signal which are not easily separable. An experiment was performed to determine the time dependent thermally generated dark current and its impact on signal to noise degradation. A series of dark images were taken with exposure times ranging from 19 msec to 100 seconds. For each image the average value from 100 pixels in the center of the image was recorded. The slope of the resulting dark signal versus time indicates that approximately 8 thermal counts per second per pixel are generated with the sensor at the nominal sensor operating temperature of 252 Kelvin. The normal exposure time for a sky image is 19 msec, thus these thermal counts become significant only if the CCD is not cleared immediately prior to acquiring an image. Thus we chose to continuously clock out charge from the chip prior to exposing an image. There is also a position dependent dark signal, a result of pixel-to-pixel bias variations as well as local well fabrication differences. Immediately following each sky image a dark image is acquired. The dark image is then subtracted off of the sky data image as the first step in the data processing. In addition to this dark noise, readout noise from the sampling electronics occurs and is difficult to independently estimate or separate from the dark noise. All of the noise factors together result in a standard deviation per pixel of 11 counts.

c. Linearity Characterization

Charge coupled device arrays are inherently linear devices when properly biased. Nevertheless, an experiment was performed to determine the overall system response linearity. The camera imaged a diffusing plaque from a constant distance. The source illuminating the diffuser was then placed at logarithmically spaced distances for each set of exposures in order to achieve the desired plaque irradiances. An image data set was acquired at each step and an average value from the center 100 pixels was recorded. The results are shown in Fig. 2. The linearity of output signal relative to input light was verified for 3 orders of magnitude of viewed radiance.

d. Absolute Radiometric Flux Calibration

In order to determine the absolute spectral response of each CCD pixel, it was necessary to first determine the absolute transmission curve *T(λ)* for each interference - neutral density filter pair. A monochromator (Optronics 740A) configured for 1 nm resolution was used to measure the filter transmission. The measurement extended to where the transmission was 10^{-4} of the peak transmittance on each side of the filter's peak. This was repeated for all 4 interference filters. The interference filters' bandwidth and center frequencies are summarized in Table 1. .

Following this the system was set to view a nearly lambertian calibrated Spectralon plaque at 45 degrees off normal. The plaque was illuminated by a 1000 W standard lamp (FEL, spectral irradiance calibration traceable to NIST). This provided a known source of radiance for the system. Unfortunately, this laboratory source is much dimmer than the solar aureole, thus we could not include the neutral density filters in this measurement. The transmission of the neutral density filters were determined in the same manner as the interference filters, and these transmission values were folded into the calibration. An absolute calibration factor was then determined for each pixel, and a matrix was constructed such that when applied pixel-by-pixel to image data, after the dark signal removal, it corrects both for optical rolloff as well as generating absolute radiance values.

e. Absolute Radiometric Accuracy and Precision

Tests were performed to quantify absolute radiometric jitter, i.e. repeatability or the lack thereof between measurements. A plaque was illuminated with a steady source and then 20 images were acquired. After applying the above calibration procedure to each image, a 100 pixel sample near the center of each image was selected for analysis. The results show that the absolute jitter, i.e. radiometric precision, for the entire electromechanical system is on the order of 0.1%. The absolute calibration of the system is limited by the accuracy of the standard lamp and is assumed to be on the order of 3%.

f. Optical Beam Spread Function

Since the lens is focussed to infinity, for a perfect lens, all photons incident at one angle are mapped to exactly 1 point on the array. To test our system a helium-neon laser beam was expanded to a diameter larger than the camera aperture in order to both fill the aperture and to decrease the divergence of the laser beam. This beam then directly illuminated the camera aperture from a series of angles (0, 1, 2, 3, 4, 5, 6 and 7 degrees). At each angle an image was acquired. These measurements showed that over 90% of the counts were contained within 0.1 degrees from the center of the spot.

4. Data Acquisition and Reduction

During the data acquisition sequence, upon alignment with the sun, the instrument digitizes and stores a sky radiance image, a dark image, and housekeeping data.

To reduce the data, a series of automated programs were written in Spyglass Transform. These routines act on a collection of raw data (image and dark) files to remove the dark signal. The resulting images are processed to produce image arrays where pixel values are calibrated radiance, and pixel positions correspond to small solid angle elements of the sky at each point in the instrument's field of view. Following this procedure, the user then decides by visual inspection which images merit further analysis. This step is necessary to filter for cloud contamination or measurement artifacts (field of view obstruction, flaring, etc.). The next step in the analysis is completed by a series of automated image analysis programs developed for the Matlab data analysis package.

The Matlab programs opens a data file containing the calibrated image. Embedded in this file are coordinates of the pixel closest to the center of the sun, while a separate data file contains solar air mass, the channel wavelength mapping, solar constants, Rayleigh, aerosol and ozone optical depths for the dataset. The image header is stripped and the data transposed and stored in a format suitable for further analysis. A similarly dimensioned (512x512) matrix is generated where each pixel value corresponds to the air mass at the corresponding camera image pixel. Finally a matrix is constructed where each pixel value is the scattering angle at the corresponding data image pixel. An example radiance image is shown in Figure 3.

Due to diffraction effects it is necessary to filter or "digitally occult" some pixels near the image center. The software determines the points which lie within a small user-definable angle of the sun center and generates a mask to zero data in the original radiance image array. These occulted pixels are shown as the white circle in Fig. 3. This mask is also applied to the scattering angle and air mass matrices.

It is useful to examine the images for sky homogeneity by examining left / right symmetry of radiance vs. scattering angle. A typical scatter plot, for a good data set, showing this symmetry is shown in Fig. 4. After determining symmetry, it is necessary to resample the flagged almucantar data into appropriately sized solid angle bins. This is accomplished by setting a user-definable (half-cone angle) bin size (usually 0.25 degrees) and averaging over all data within that scattering cone, within the appropriate air mass limits and where the data has not been digitally occulted. The almucantar sampled is shown as the white band in Fig. 3 . An example plot showing the resampled almucantor radiance for the solar aureole is shown in Fig. 5. Once this aureole radiance is determined it can be combined with independent measurements of the aerosol optical depth to determine the small angle scattering phase function, and a parameter related to the slope of the large particle size distribution.

As an example derived product, Fig. 6 illustrates several aerosol phase functions derived from the aureole measurements (Ritter 1998). These are derived from several measurements of the solar aureole performed on a single day. They were derived assuming single scattering and that the aerosols were contained in a single layer in the atmosphere. They show a small variation in the small angle portion of the aerosol scattering function over this period.

5. Conclusions

A new instrument has been described which can measure the sky radiance distribution near the solar disk even when operated on an unstable platform. Use of an imaging detector, and the presence of an image of the solar disk in each image, allow accurate directional information to be obtained. This eliminates possible ambiguities about the angular position of the data, and increases the accuracy of the measurement. A special triggering device aids in making these measurements on a ship. This instrument will be used in field studies of atmospheric aerosols and in satellite validation campaigns.

6. Acknowledgements

The authors are grateful for support from the NASA Goddard Space Flight Center under contracts NAS5-31363. We would also like to thank Mr. Albert Chapin for his help in machining the instrument.

References

Clark, D. K., H. R. Gordon, K. J. Voss, Y. Ge, W. Broenkow, and C. Trees, 1997: Validation of atmospheric correction over the oceans. J. Geophys. Res., **102**, 17209 - 17217.

Holben, B., A. Setzer, T. F. Eck, A. Pereira and I. Slutsker, 1996: Effect of Dry-Season Biomass Burning on Amazon Basin Aerosol Concentrations and Optical Properties. J. Geophys. Res., **101**, 1992-1994.

Houghton, J. T., L. G. Meira Filho, B. A. Callendar, N. Harris, A. Kattenberg and K. Maskell (Editors), 1996: *Intergovernmental Panel on Climate Change (IPCC), Climate Change (1995): the Science of Climate Change*, Cambridge University Press, N.Y.

Nakajima, T., M. Tanaka and T. Yamauchi,1983: Retrieval of the Optical Properties of Aerosols from Aureole and Extinction Data. Appl. Opt., **22**, 2951-2959.

Nakajima, T., G. Tonna, R. Rao, P. Boi, Y.J. Kaufman and B. Holben, 1996: Use of Sky Brightness Measurements from Ground for Remote Sensing of Particulate Polydispersions, Appl. Opt., 35, 2672-2686.

Ritter, J. M., 1998: Remote measurement of aerosol scattering properties and the development of a novel imaging solar aureole radiometer, Ph.D. Thesis, University of Miami, Coral Gables, Fl. 33124.

Figure Captions

1) Schematic of aureole camera system.

2) Linearity plot obtained with aureole camera system. Data points are 10 x 10 pixel averages in the center of the image. System shows good linearity at over 3 orders of magnitude. Standard deviation of the pixel values are displayed as error bars in the x direction.

3) Sample aureole image contour. Several important features in the image are identified.

4) Plot of the aureole, separating left and right sides of the aureole almucantor. This illustrates the symmetry of the data set. This type of plot can be used for quality control of the data.

5) Sampled aureole almucantor data.

6) Aerosol phase function derived from aureole data. Phase functions were derived using single scattering and assuming the aerosols were contained in a single layer.

Filter (nm)	Centroid (nm)	Full width at half maximum (nm)
440	440.9	10
560	561.3	10
670	670.2	12
860	856.6	13

Table1. Interference filter bandwidth and center frequencies

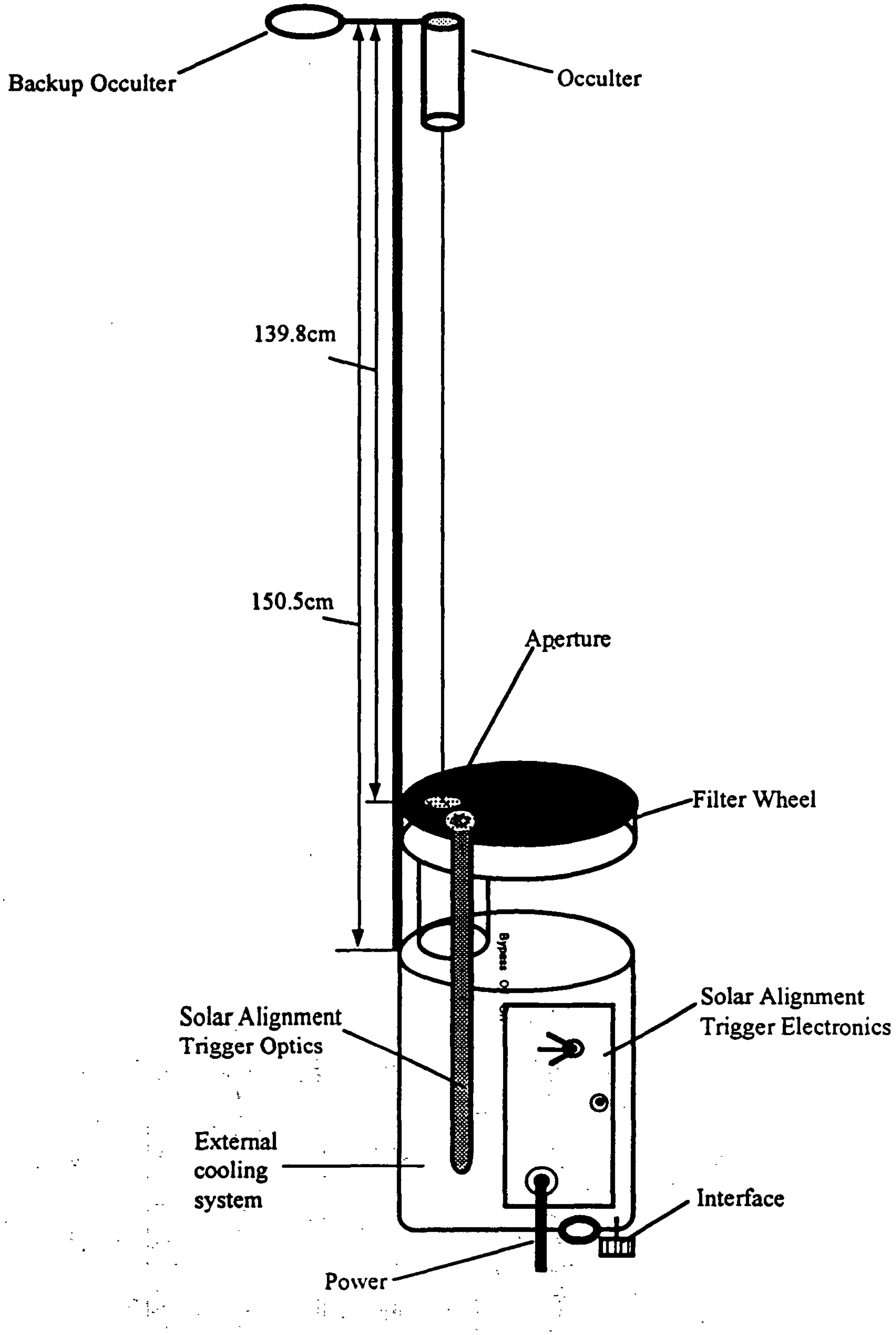
Backup Occulter
Occulter
139.8cm
150.5cm
Aperture
Filter Wheel
Bypass
Solar Alignment Trigger Optics
Solar Alignment Trigger Electronics
External cooling system
Interface
Power

Fig 1

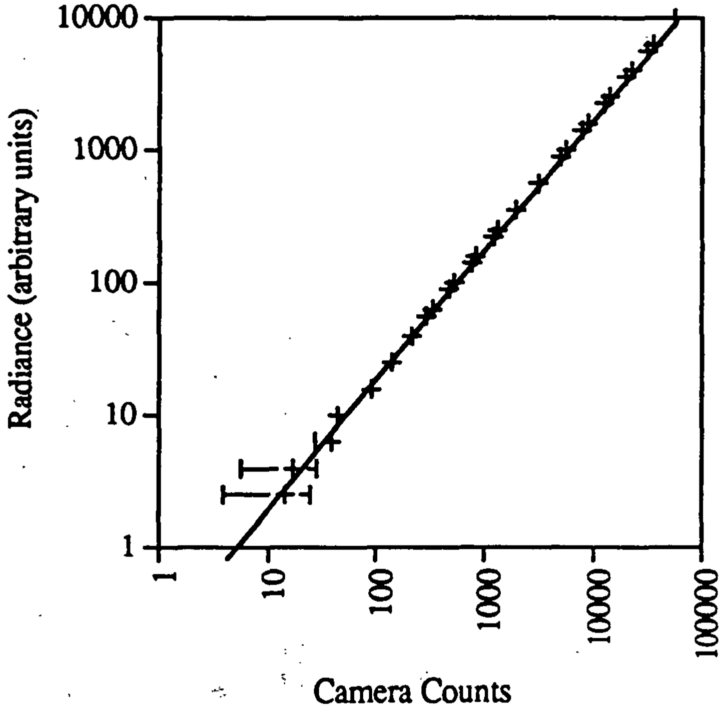
10000
1000
100
10
1
Radiance (arbitrary units)
1
10
100
1000
10000
100000
Camera Counts

Fig 2

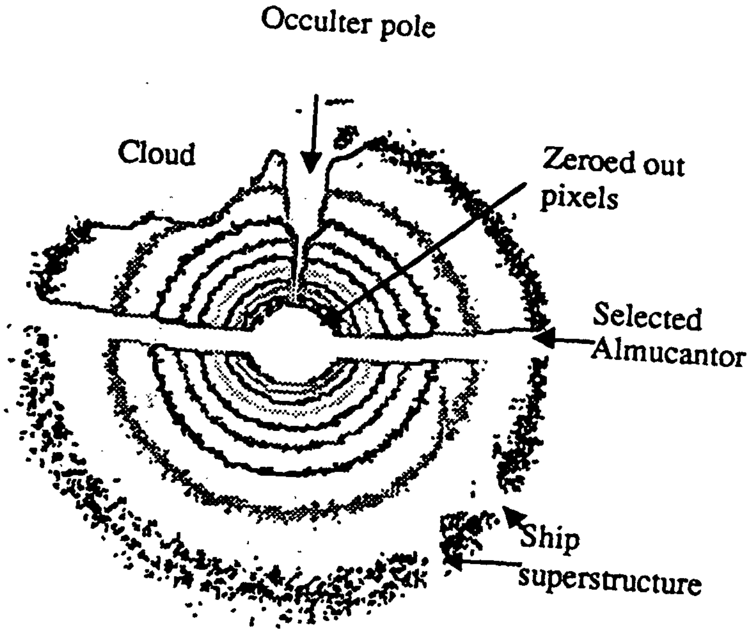
Occulter pole
Cloud
Zeroed out
pixels
Selected
Almucantor
Ship
superstructure

Fig 3

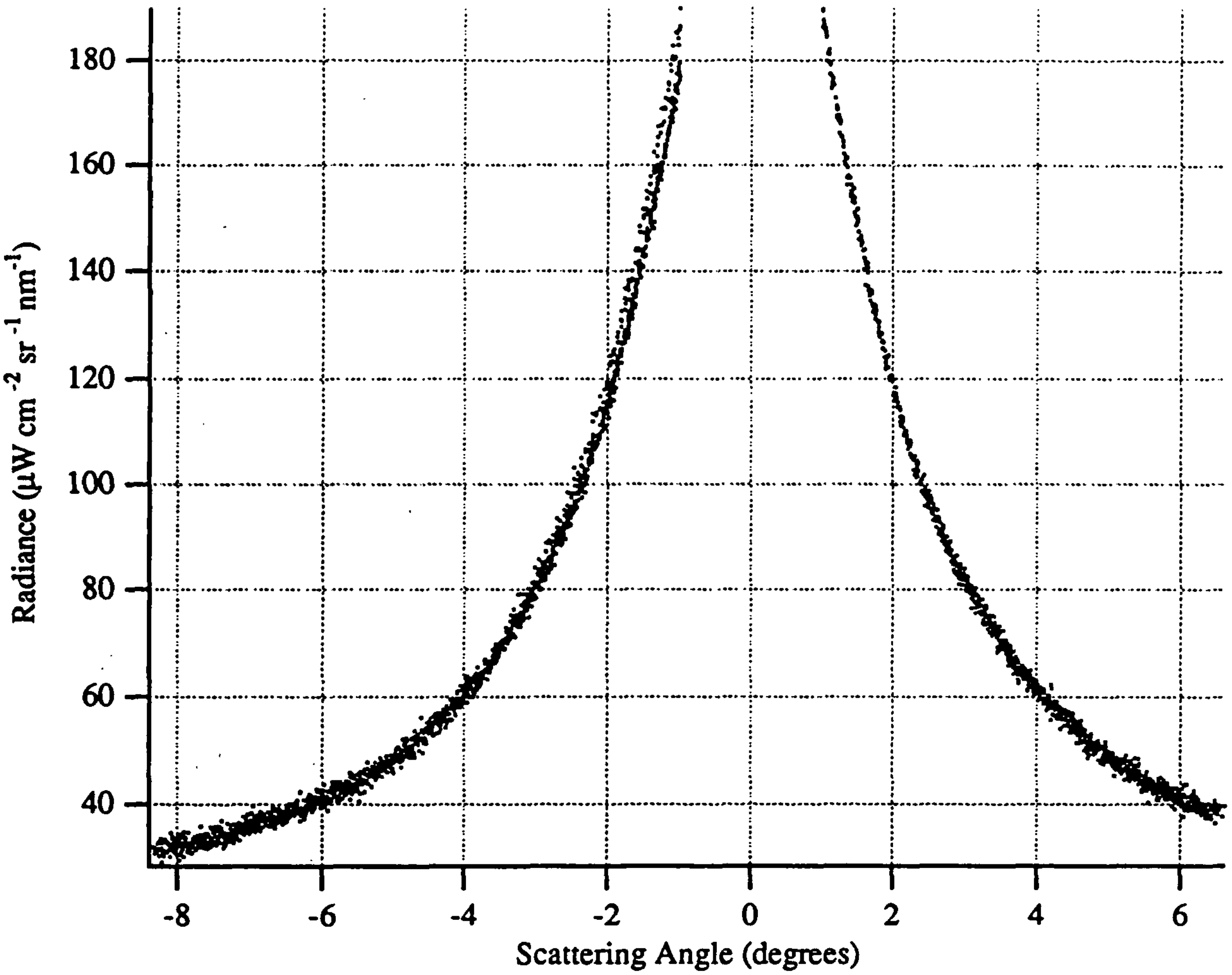
Radiance (µW cm -2 sr -1 nm-1)
180
160
140
120
100
80
60
40
-8
-6
-4
-2
0
2
4
6
Scattering Angle (degrees)

Fig 4

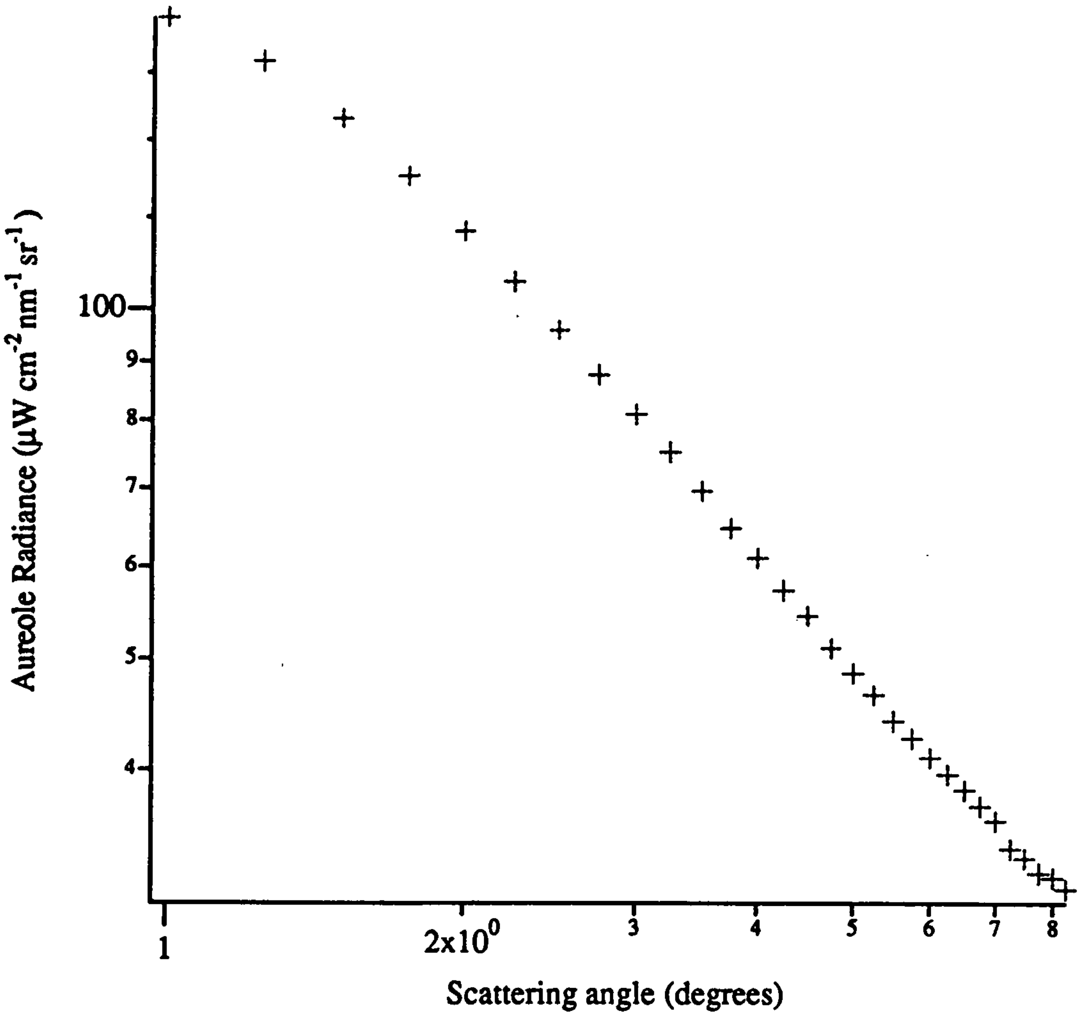
Aureole Radiance (µW cm^{-2} nm^{-1} sr^{-1})
100
9
8
7
6
5
4
1
2x10^0
3
4
5
6
7
8
Scattering angle (degrees)

Fig 5

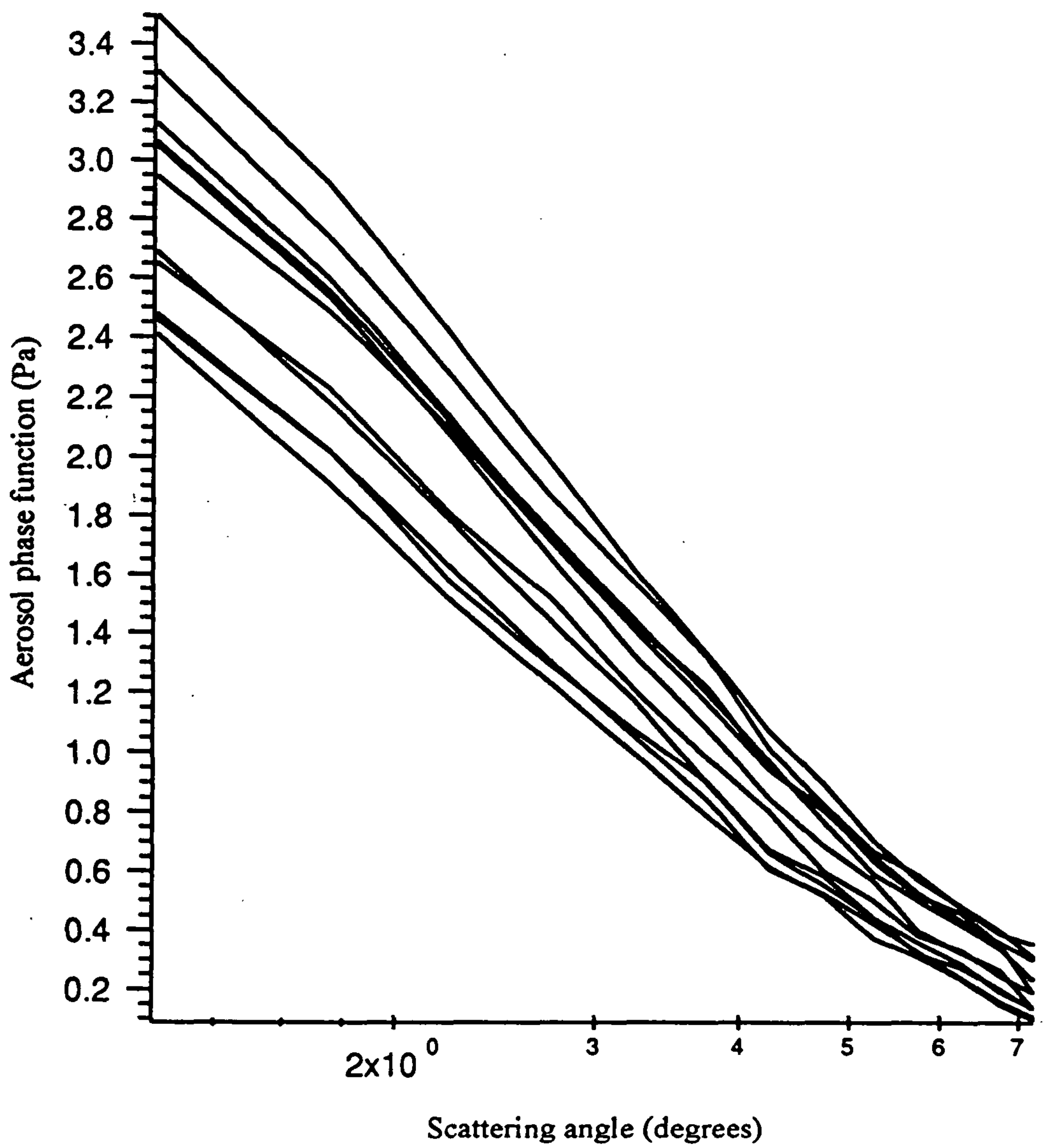
Aerosol phase function (Pa)
3.4
3.2
3.0
2.8
2.6
2.4
2.2
2.0
1.8
1.6
1.4
1.2
1.0
0.8
0.6
0.4
0.2
2x10 0
3
4
5
6
7
Scattering angle (degrees)

Fig 6

Measurements of Aerosol Optical Depth over the North Atlantic Ocean: Correlations with Surface Aerosol Concentrations

Ellsworth J. Welton, Kenneth J. Voss, Dennis L. Savoie,
and Joseph M. Prospero

Abstract:

The optical properties of atmospheric aerosols are an important element of the global radiation balance and in applications such as remote sensing. One of the most important optical properties is the aerosol optical depth (AOD) and it's associated wavelength dependence, characterized by the Angstrom exponent α. Long term measurements of these aerosol features taken at various locations are necessary to track seasonal patterns of aerosol optical behavior and to determine characteristic differences in the optical properties of different sites. An AOD measurement program was begun in August of 1993 to determine the optical properties of aerosols over existing Atmosphere/Ocean Chemistry Experiment (AEROCE) sites in Miami (Florida), Bermuda, and Barbados. A description of the optical program, instrumentation and calibration procedures, and the methodology employed to determine the AOD and α are presented. Analysis of the AOD and Angstrom exponents in terms of seasonal variations and correlations with surface concentration measurements is also presented. Seasonal variations in the optical properties of the aerosols were found to be due to seasonal changes in the types and concentrations of specific aerosol species. The correlational analysis has shown that under certain circumstances aerosol species may be identified over the ocean based on analysis of the AOD and Angstrom exponent.

Keywords: aerosols, optical depth, Angstrom exponent, sunphotometer, shadowband, sulfate, sea-salt, dust

1. Introduction

There is relatively little information on the climatology of atmospheric aerosols, particularly over the ocean. However, the radiative effects of marine aerosols directly alter terrestrial optical properties, such as the planetary albedo, and may play an important role, directly and indirectly, in the global climate [*Charlson*, 1992]. In addition to this climatic impact, marine aerosols also affect our ability to extract surface information from satellites, in particular for ocean color remote sensing [*Gordon*, 1997]. Knowledge of the aerosol optical properties are necessary to correct for these effects in both Global Circulation Models and in satellite correction algorithms.

The most commonly measured aerosol optical property is the aerosol optical depth (AOD), which determines how the aerosol attenuates the direct solar beam. The total optical depth, τ, at a particular wavelength is defined by

$$\tau = \frac{1}{m(\theta)} \ln\left(\frac{E_o}{E}\right) \tag{1}$$

where $m(\theta)$ is the airmass at zenith angle θ, E_o is the extra-terrestrial solar irradiance (solar constant), and E is the direct, unscattered and unabsorbed solar irradiance at the surface. For wavelengths that lie outside the usual atmospheric gas absorption bands, the total optical depth may also be written as the sum

$$\tau = \tau_R + \tau_O + \tau_A \tag{2}$$

where τ_R is the Rayleigh optical depth due to molecular scattering, τ_O is the Chappius band ozone optical depth, and τ_A is the aerosol optical depth. The basic experimental method of acquiring the AOD from the total optical depth has been outlined in several papers, most notably Shaw [1979] and King et al. [1980].

Measurements of aerosol optical depths [*King et. al.*, 1978; *Hoppel et. al.*, 1990; *Kaufman*, 1993; *Dutton et. al.*, 1994; *Smirnov et. al.*, 1994, 1995], made at a variety of locations around the globe and at wavelengths throughout the visible spectrum, have shown that the spectral dependence of the AOD often resembles a power law [*Angstrom*, 1964]:

$$\tau_A = \beta\lambda^{-\alpha} \tag{3}$$

where τ_A is the AOD at wavelength λ, β is a scale factor, and α is the Angstrom exponent. The Angstrom exponent α may be related to the exponent of a Junge type size distribution ($dn/dr = Cr^{-(\gamma+1)}$) by

$$\gamma = \alpha + 2 \tag{4}$$

[*Van de Hulst*, 1981]. The exponent, α, generally varies from zero to two. Lower values of α are associated with relatively more larger-sized particles than aerosol populations with higher α values.

In order to obtain long term data sets of the AOD, hand-held sunphotometers were used at existing AEROCE (Atmosphere/Ocean Chemistry Experiment) sites in Miami (Florida), Bermuda, and Barbados. AEROCE sites also measure various aerosol parameters including concentration, and mass-size distributions. The stations are located at coastal sites and, with the exception of the AOD measurements, samples are collected only during on-shore winds; thus the aerosol data should be representative of the regional oceanic aerosol. The hand-held sunphotometers were replaced with automated multi-filter rotating shadowband radiometers by the end of 1994. The shadowbands create a more complete data record as they automatically sample all day, perform a potential calibration each day (dependent on weather), and also measure diffuse irradiance. The shadowbands operated concurrently with the sunphotometers for several months during the instrument replacement process. Table 1 indicates the geographical information and time period of the sunphotometer and shadowband measurements at each site. The instrument calibration procedure, methods of data selection, aerosol optical depths, and Angstrom exponents recorded for each site are presented in this paper.

Recent measurements of aerosol optical depths have indicated a need to also analyze their other physical characteristics in order to fully understand their climatological impact [*Kaufman et. al.*, 1994; *Smirnov et. al.*, 1995]. Li et. al. [1996] have published results of short term analysis of the optical properties of aerosols in Barbados using concurrent analysis of aerosol composition and concentration levels. Also, Pueschel et. al. [1994] have performed similar analysis of stratospheric Pinatubo aerosols from aircraft observations. Finally, several other researchers [*Hoppel et. al.*, 1990; *Smirnov et. al.*, 1995] have used synoptic air mass analysis to describe aerosol radiative measurements. However, there have been no long term studies of the relationship between aerosol optical depth measurements and the concentration of specific aerosol species.

The radiative properties of aerosols are a function of two main factors: the composition of the aerosols, and the aerosol production mechanisms. The magnitude of the AOD is proportional to the concentrations of the aerosols (the scale factor, β). The Angstrom exponent is dependent on the production mechanisms of each aerosol species. Aerosol concentrations are available for each AEROCE site. Correlations between concurrent measurements of the AOD and aerosol concentrations and resulting seasonal dependencies are also presented in this paper. The goal of the correlational analysis was to determine if it is possible to distinguish between different aerosol species based only on analysis of the AOD and Angstrom exponent (two parameters readily available from satellite remote sensing programs).

2. Instrumentation Description

Two different instruments were deployed at each AEROCE site: sunphotometers, and Multi-filter Rotating Shadowband Radiometers (shadowbands). The instruments were used to determine the total optical depth from measurements of the direct sunlight using Eq. (1). The AOD was calculated from the total optical depth using Eq. (2). Sunphotometers were first installed at each AEROCE site in the Fall of 1993. The sunphotometers were replaced with shadowbands by the end of 1994.

2.1 Sunphotometers

The sunphotometers [*d'Almeida et al.*, 1983] were manufactured by NOLL GMBH in Germany, and were provided by John DeLuisi at CMDL-NOAA. The sunphotometers used in this study had nine interference filters, with passbands approximately 5 nm wide, centered at the wavelengths shown in Table 2. Identical filters, selected from the same lot, were used in each sunphotometer and were selected to avoid water vapor absorption bands. The sunphotometers are operated manually by pointing the instrument at the sun. The operator then moves the instrument in small circles around the central direction of the sun. The instrument retains the highest signal measured and displays this reading, which is the direct sun signal that is used to determine the optical depth. The operator performs direct sun measurements for each filter in the sunphotometer. The signal, filter number, instrument temperature, and the time in GMT (either from an accurate watch or the instrument display) are recorded and then the process is repeated for the remaining filters.

2.2 Shadowbands

The shadowbands were designed by Lee Harrison and Joe Michalsky at SUNY/Albany and were manufactured by Battelle Labs in Richland, WA. A complete description of the shadowbands may be found in Harrison et al. [1994]. Shadowbands measure total downwelling irradiance and the diffuse irradiance by shadowing the irradiance collector. The direct irradiance, determined by subtracting the diffuse irradiance from the total irradiance, is then used to determine the spectral optical depth. The shadowbands are autonomous instruments designed to operate remotely in the field and are controlled via a phone line modem link. The shadowband consists of two main components: a control unit, and detector platform. The detector platform holds the band motor and detector housing. The detector housing holds the irradiance collector and seven photodiode detectors. Six of the seven photodiode detectors have spectral interference filters encapsulated with the detector. The filter wavelengths, with passbands 10 nm wide, are given in Table 2. Filter 1, a broadband filter, and filter 7, a water vapor band filter, were not used in this study. Filters 2 to 6 were chosen to avoid water vapor absorption bands. The filters are positioned so that they view the back of the irradiance collector. Measurements are performed with the 7 filters simultaneously.

2.3 Aerosol Concentration Measurements

Ground-based aerosol concentration samples are collected by drawing air through 20x25 cm Whatman 41 (W41) filters at a flow rate of about 1.1 $m^3\,min^{-1}$, yielding average sampled volumes of about 1500 m^3. W41 filters have collection efficiencies greater than 90% for nss sulfate and ammonium, 95% for nitrate and sea-salt [*Savoie*, 1984], and 95% for mineral aerosol [*Arimoto et al.*, 1996]. At all sites, the aerosol sampler is linked to a wind sensor which controls the operation of the sampler so that it is activated only when the wind blows from the open ocean sector at a speed greater than 1 m/s. Filters are returned to Miami were they are extracted with deionized water and the extracts analyzed for major soluble inorganic ions: Na^+ by flame atomic absorption and Cl^-, NO_3^-, $SO_4^=$ by suppressed ion chromatography [*Savoie et al.*, 1989] and NH_4^+ by automated colorimetry. Non sea-salt sulfate (nss $SO_4^=$) is calculated: [total $SO_4^=$] - [Na^+ * 0.2517], where 0.2517 is the $SO_4^=/Na^+$ mass ratio in bulk sea water. The extracted filters were then placed in a muffle furnace for about 14 hours at 500°C; the residue weight (less filter blank) is assumed to be mineral dust ash.

3. Sunphotometer and Shadowband Calibrations

The instruments described in Section 2 must be calibrated before beginning analysis of the data taken with them. For the purposes of this study, the term calibration refers to all procedures that must be performed upon the instrument in order to determine the aerosol optical depth using data acquired with the instrument. The procedures used to calibrate the sunphotometers and shadowbands are described in this section.

3.1 Sunphotometer Calibrations

The calibration of the sunphotometers involves determination of E_0 (in instrument counts), also referred to as the solar constant, by using procedures based on the Langley calibration method [*Shaw*, 1979; *King et al.*, 1980]. The sunphotometers were operated by on-site AEROCE personnel who recorded measurements at approximately 10:00 am and 3:00 PM local time respectively. Therefore, normal instrument operations do not acquire enough data to perform Langley calibrations. Specific Langley measurements had to be performed with each instrument from the Miami, Bermuda, and Barbados AEROCE sites. An additional sunphotometer was used for calibration processes during and after the measurement period.

Initially the Langley method was used to perform the calibrations, for each sunphotometer, in Miami prior to deployment into the field. The instruments were then sent into the field, and operations began as indicated in Table 1. With the exception of poor weather days, the measurements continued uninterrupted for the remainder of the sunphotometer program. It was difficult to perform sea-level Langley calibrations in these locations because of atmospheric variability and cloudiness. Thus it was not possible to have the on-site operator perform routine Langley calibrations at the Bermuda and Barbados locations. The Miami instrument (M114) was calibrated several times during the sunphotometer program, both in Miami and in Brainard Lake, Colorado. An additional sunphotometer (M119), not tied to any location, was extensively calibrated during an oceanographic cruise, off of Hawaii, in October and November of 1994. Post-calibrations for the Bermuda and Barbados instruments were performed in Miami at the end of the sunphotometer program (through a method described below).

A calibration history for each instrument was compiled in order to account for time shifts in the solar constants, often caused by degradation of the filters. The calibration record for an instrument consists of a plot of the date versus E_0 for the length of the entire data set. For the period when the instruments were deployed, calibration values were obtained by an interpolation between the initial calibrations and the post-calibrations. Prior experience with the degradation of sunphotometer interference filters led to the use of an exponential function for the interpolation of the calibration constants. An error correction procedure was then employed for both instruments to modify the conventional Langley calibrations.

It was difficult to perform full Langley calibrations on the instruments at the end of the sunphotometer program due to poor weather. The Miami instrument was calibrated several times during the initial startup, and throughout the program, and was considered to be the best calibrated of the sunphotometers. The M119 sunphotometer was well calibrated, using the Langley procedure, during October and November 1994 and was used to calibrate the Miami instrument at the end of the sunphotometer program through a cross-calibration procedure. A cross-calibration assumes that two identical sunphotometers are present; one is fully calibrated and is referred to as the reference instrument, while the other is uncalibrated and referred to as the target instrument. Simultaneous direct beam measurements are made with each sunphotometer at the same location. The resulting equations for each instrument are

$$E_r = E_{ro}\exp[-m_r(\theta)\tau] \quad , \qquad (5)$$

$$E_t = E_{to}\exp[-m_t(\theta)\tau] \quad , \qquad (6)$$

where the r subscript denotes the reference instrument and the t subscript denotes the target instrument. As E_{ro} is known, the τ is calculated using the calibrated reference instrument. Once the TOD is determined, E_{to}, can be written as

$$E_{to} = E_{ro} \frac{E_t}{E_r} \exp\left[-\tau\left(m_t(\theta) - m_r(\theta)\right)\right] \qquad (7)$$

for each wavelength of the uncalibrated target sunphotometer. This cross-calibration procedure was useful because the weather need only be stable and cloud-free for a small window of time. Ideally, the target and reference measurements should be made at exactly the same time so the two airmass values are equal, the exponential term is zero, and τ need not be determined. However, exactly simultaneous measurements are often not possible, therefore, the reference and target airmass values should be as close as possible to avoid errors in calculating E_{to}.

The Miami instrument, (M114), was cross-calibrated against M119 at the end of the program and the cross-calibrations were added to the calibration history for M114. Sunphotometer M114 was then used as a reference instrument during cross-calibrations for the Bermuda and Barbados sunphotometers. These cross-calibrations were then added to the calibration history for Bermuda and Barbados. The calibration histories for each sunphotometer at the three locations are given in Figures 1a, 1b, and 1c. The solid line is the exponential fit to the calibrations given above.

An error correction procedure was developed to fine tune these solar constants. This procedure assumes that there is some error, χ, present in the solar constant for each wavelength, and that the aerosols above the sites, on average, obey the Angstrom spectral dependence. Redefining the solar constant in terms of this error and the true solar constant yields

$$E_o = \chi E_o' \quad , \qquad (7)$$

where E_o is the previously derived solar constant, χ is the error factor, and E_o' is the true solar constant. The measured τ is given by

$$\tau = \frac{1}{m(\theta)} \ln\left(\frac{E_o}{E}\right) = \frac{1}{m(\theta)} \ln\left(\frac{E_o'}{E}\right) + \frac{\ln(\chi)}{m(\theta)} \quad , \qquad (8)$$

using Eq. (7). The first term on the RHS of Eq. (8) is the true TOD (τ') as follows from using Eq. (1) and Eq. (7), therefore, the following equation is calculated

$$\ln(\chi) = [\tau - \tau']\,\mathrm{m}(\theta) \quad , \tag{9}$$

relating the error factor, χ, to the difference in measured and true total optical depths. τ_R and τ_O are subtracted from both the measured and true total optical depths since they are known. The resulting equation

$$\ln(\chi) = [\tau_A - \tau'_A]\,\mathrm{m}(\theta) \quad , \tag{10}$$

relates the error factor, χ, to the difference in measured and true aerosol optical depths.

In the calibration process, a sunphotometer reading consisted of recording, E, for each of the nine wavelengths. The AOD was then fit to Eq. (3), determining β and α, and this equation was then used to generate τ'_A, producing the final relation

$$\ln(\chi) = [\tau_A - \beta\lambda^{-\alpha}]\,\mathrm{m}(\theta) \quad . \tag{11}$$

Therefore, $\ln(\chi)$, is the difference between the measured AOD and the Angstrom fitted AOD for a given wavelength, times the airmass. This factor determines the variation from the Angstrom power law for that particular measurement.

The AOD, for each location's entire data set, was first calculated using the original solar constants from the calibration histories, and Rayleigh optical depths determined using Hansen and Travis [1974] and ozone models provided by Klenk et al. [1983]. For each day, the deviation of the AOD from the Angstrom power law was determined using Eq. (11) and the error factor, χ, was calculated. The time history of χ was fit by another exponential function, yielding an equation for χ for each instrument. This equation was used to correct the solar constants according to Eq. (7). The error-corrected solar constant histories are plotted in Figures 1a, 1b, and 1c as the dotted lines.

Channels one (380.2 nm) and nine (1025.9 nm) were not processed, and were not used in this study. The 380.2 nm filter degraded rapidly in all instruments and was considered unusable. Channel nine deviated significantly from the Angstrom power law, perhaps due to the weak water vapor absorption band around 1000 nm [*Shaw*, 1979] which was not considered in our analysis, or the effects of sea spray [*Villevalde et al.*, 1994]. These error-corrected calibration values are not significantly different from the original values but provide a fine-tuning adjustment.

3.2 Shadowband Calibrations

The shadowbands began operation in the fall of 1994. The shadowbands ran automatically, eliminating the need for an on-site operator. The Miami shadowband sampled data every minute throughout the day. The Bermuda and Barbados shadowbands sampled every four minutes to reduce the number of data downloads per week. As the shadowbands perform measurements continually, each day offers the potential of a Langley calibration. Therefore the calibrations for the shadowbands are more complete than those for the sunphotometers since the actual daily data can be used to perform the Langley calibrations. Gaps are present in all data sets due to instrument malfunctions and the subsequent time needed to repair the problems. A gap exists in the Miami data from September 1995 to November 1995. This was caused by data communication problems and poor weather. Normal operation began again in December 1995. The Bermuda data gap, also caused by data communication problems, resulted in the loss of data from July 1995 to November 1995. The communication problems were fixed in December 1995 and shadowband operation was continued. The Barbados shadowband data set only includes data from May 1995 to August 1995 due to poor phone line connections for data transfer and unstable electrical power at the site.

All of the shadowbands collect enough data each day to perform two Langley calibrations, one in the morning and one in the afternoon, weather permitting. Therefore all that remains is to determine which of the days has weather suitable for Langley calibrations. Each shadowband's data set was analyzed using the Objective Langley Regression Algorithm (OLRA) [*Harrison and Michalsky*, 1994] in order to recover the solar constants for each instrument. The OLRA rejected a large number of the Langley calibrations for all three sites due to the variable tropical weather at each location. However, the strict criteria in the OLRA assures that the remaining Langley calibrations are accurate. Once the solar constants for each shadowband were determined using this technique, a calibration history was compiled in the same manner as for the sunphotometers. The calibration histories for each shadowband and interpolations are depicted in Figures 2a, 2b, and 2c.

There were few solar constant values recovered for the Barbados shadowband due to the small time period of the data set. Therefore, the solar constants for the Barbados shadowband were obtained by using the mean value of the solar constant for each channel instead of the interpolations described above. A linear fit to the calibration histories was performed for all of the channels except channel four (610 nm) of the Miami shadowband, and channels four and five (610 and 665 nm respectively) of the Bermuda shadowband. The filters in these channels were found to stabilize after a period of time making a single linear fit unsuitable. Instead a linear fit was performed on the first part of the calibrations, ignoring the stabilized portion, and a second linear fit was performed on the more stable portion.

These Langley calibrations were fine tuned with another procedure. This procedure assumes that there is some error, μ, present in the solar constant. Angstrom spectral dependence in the AOD was not assumed. The shadowband records more samples and with more variation in solar zenith angle than the sunphotometer, therefore, it is possible to analyze a month's worth of shadowband data to test for dependence of the AOD on solar zenith angle. We assume that the set of minimum aerosol optical depths should not depend on solar zenith angle (airmass) over the span of one month. Then the lowest optical depths on a plot of the AOD versus 1/m(θ) for a given month will represent a background AOD. A linear fit to the lowest aerosol optical depths in the plot described above should have zero slope and a y intercept equal to the average background AOD for that month. A slope not equal to zero would indicate that the background AOD has some dependence on the airmass, and thus an error in the solar constant [*Ignatov*, personal communication, 1996].

Assuming that there is some error, μ, in the solar constants yields the following equation

$$E_o = \mu E_o' \quad , \tag{12}$$

where E_o is the previously derived solar constant, μ is the error factor, and E'_o is the true solar constant. Inserting Eq. (12) into Eq. (1) produces the following relation

$$\tau = \frac{\ln(\mu)}{m(\theta)} + \frac{1}{m(\theta)}\ln\left(\frac{E'_o}{E}\right) = \ln(\mu)\frac{1}{m(\theta)} + \tau' \quad , \qquad (13)$$

τ' is the true optical depth as it contains the true solar constant, E_o'. The Rayleigh [*Hansen and Travis*, 1974] and ozone [*Klenk et al.*, 1983] optical depths are not dependent on the calibrations so they may be subtracted from both sides of Eq. (13) to produce the equation

$$\tau_A = \ln(\mu)\frac{1}{m(\theta)} + \tau'_A \ . \qquad (14)$$

Equation (14) may only be used when both τ_A and τ'_A represent the background (minimum) AOD. Therefore, the slope of the background AOD versus $1/m(\theta)$ plot described above is the natural logarithm of μ and the y intercept is the true background AOD (τ'_A). This procedure was used to obtain monthly values of μ for each shadowband channel. The error corrected solar constants are plotted in Figs. 2a, 2b, and 2c.

4. Aerosol Optical Depths and Concentrations

The aerosol optical depths and corresponding Angstrom exponents were calculated for the AEROCE sites in Miami, Bermuda, and Barbados using both the sunphotometer and shadowband data. The uncorrected and the error corrected calibrations described in sections 3.1 and 3.2, were applied to the data sets separately in order to gauge the usefulness of each error correction method. Data screening procedures were then used to remove optical data affected by atmospheric phenomena other than aerosols, such as clouds. Both data screening procedures were similar, but due to the nature of the instruments, a different screening procedure was employed for each instrument. The screening procedures and comparisons between the uncorrected and error corrected results are described below. The tolerance criteria in each of the data screening processes were a compromise between eliminating questionable data and retaining enough of the data set to analyze. Finally, the resulting AOD and Angstrom exponents were correlated with surface measurements of the specific aerosol species concentrations for each site.

4.1 Sunphotometer Data Screening Procedure

The aerosol optical depths and Angstrom exponents were calculated for channels two through eight, for the respective data sets, due to the calibration problems with channels one and nine. The sunphotometer data screen contained three levels. Level One determined the deviation of the measured τ_A from the power-law-fitted τ'_A for a given measurement, similar to the error factor procedure above. If the magnitude of the deviation between τ_A and τ'_A was greater than 0.1, then the measured AOD at that wavelength was rejected. This was done to screen out AOD measurements that varied strongly from an Angstrom power law. The aerosol optical depths that survived this level were then subjected to Level Two of the screen. It should be noted that a given measurement set consists of two series of readings, E, for each of the nine channels. This was done to ensure that atmospheric properties were fairly constant during the measurement set, as the optical depth should not change appreciably during a span of five minutes (the approximate time for one measurement set). The Level Two screen examined the difference between the first and second measured aerosol optical depths. If the magnitude of the difference was greater than 0.03, then that channel was rejected. If only one of the two dual readings survived the Level One screen, then the Level Two screen was not performed. Finally, the Level Three screen determines if at least six of the seven channels (one and nine are excluded) remain, and channels two and eight are among them. If this was true then this measurement was considered usable, otherwise the entire measurement was discarded. This screening process ensures that the atmospheric aerosol properties are fairly constant during the measurement, that the AOD roughly resembles an Angstrom power law formula, and that there are enough remaining aerosol optical depths to accurately perform a fit to the Angstrom power law (for the wavelength range, 412.2 nm to 861.8

nm only). The AOD was then calculated from the surviving measurements and used to generate the Angstrom parameters. The remaining AOD values and the Angstrom exponent were then stored for that sample.

4.2 Shadowband Data Screening Procedure

The shadowbands record data continuously throughout the day, as opposed to the sunphotometer's singular morning and afternoon measurements. Therefore, a different screening method to eliminate bad data was developed. This method was based on the Sliding Window Optical Depth Procedure (SWODP) [*Schlemmer*, personal communication, 1996] developed at the Atmospheric Sciences Research Center at the State University of New York, Albany.

The University of Miami SWODP (MSWODP) used the aerosol optical depths for each sampled measurement by the shadowband. The MSWODP then analyzed one day at a time, starting with the first measurement sample. The term, "sliding window," originated because the MSWODP analyzed a twenty minute "window" of data to determine if the window contained usable data (free from cloud contamination). Two screening levels were then applied to the resulting AOD window by the MSWODP. Level One performed a linear least squares fit to the AOD (versus time), and then calculated the individual AOD deviations from the fit. If all of the aerosol optical depths were within 0.01 of the linear fit, then the MSWODP proceeded to the Level Two screen for that window. If Level One failed, then the MSWODP slid the window ahead one sample measurement and began the screening process anew. If Level One was successful then the MSWODP applied Level Two, which determined the mean AOD for that window. If the mean AOD was less then 1.0 then the MSWODP recorded the mean AOD and corresponding Angstrom exponent for that window. If the mean AOD was greater than or equal to 1.0 then the entire window was rejected, and no data were recorded for that window of time (possible cloud presence). Regardless of the outcome of Level Two, the MSWODP then slid the window ahead by twenty minutes to the corresponding sample measurement, and the process was started over again. The MSWODP yields twenty minute averages of the AOD, and the corresponding Angstrom parameters for each day in the data set. This analysis procedure results in aerosol optical depths that do not vary erratically, that were reasonable magnitudes for atmospheric aerosols, and excluded clouds. The remaining AOD values and the Angstrom exponent were then stored for the time of day falling at the center of the twenty minute window.

4.3 Comparison of Uncorrected and Error Corrected Results

The spectral variation of the aerosol optical depths for each sunphotometer and shadowband were analyzed to compare differences between the uncorrected and error corrected (solar constant) results. The AOD values were plotted versus the wavelengths and the Angstrom fit was applied to the data. The comparison focused on examining any changes to the Angstrom fit caused by the application of the error correction procedure.

The uncorrected sunphotometer results are not much different from the error corrected results, indicating that the data were not changed significantly by the error correction procedure. However, a small improvement to the Angstrom power law fit was obtained using the error corrected sunphotometer results. The average chi-squared data fitting parameter for each data set indicated a better power law fit. The Miami chi-squared data fitting parameter was 0.086 for the uncorrected results and 0.034 for the error-corrected results. The Bermuda uncorrected and error-corrected chi-squared parameters were 0.065 and 0.012 respectively. Finally, the Barbados uncorrected and error-corrected chi-squared parameters were 0.744 and 0.058. The sunphotometer error correction procedure assumes that the true AOD follows the Angstrom power law. Furthermore, the sunphotometer data screen explicitly screened out days (for both uncorrected and error corrected results) that did not accurately fit the Angstrom power law. For these two reasons, an improvement in the fits to the Angstrom power law between uncorrected and error corrected results was expected.

There were significant differences between the uncorrected and error-corrected results for certain channels of each shadowband. However, all of the error-corrected changes also resulted in a better average Angstrom power law fit. In particular, a clear bias in channel five of the

Miami shadowband was removed after using the shadowband error correction procedure. The Miami chi-squared data fitting parameter was 0.521 for the uncorrected results and 0.122 for the error corrected results. The Bermuda uncorrected and error corrected chi-squared parameters were 0.300 and 0.131 respectively. Finally, the Barbados uncorrected and error corrected chi-squared parameters were 0.071 and 0.059. The shadowband error correction procedure and the shadowband data screen did not assume any particular spectral form of the AOD. However, results obtained using the error corrected results more accurately portrayed a power law fit compared to the uncorrected results.

Level One of the sunphotometer data screen determined the deviation of the measured AOD from the Angstrom power law. Turning off Levels Two and Three of the sunphotometer data screen allowed the percentage of measurements rejected by only Level One to be determined. The Level One sunphotometer data screen rejected 3% of the Barbados measurements and 7% of the Miami and Bermuda measurements. Therefore, at all three locations, over 90% of the sunphotometer AOD measurements resembled an Angstrom power law. Also, there were significant improvements in the Angstrom power law fits using the error-corrected shadowband results compared to using the uncorrected shadowband data. This improvement indicates that the majority of shadowband AOD measurements also resembled an Angstrom power law, particularly since no spectral dependence of the AOD was assumed but the error corrected data more accurately fit the Angstrom power law. As a result of this analysis, the majority of the aerosol optical depths measured over Miami, Bermuda, and Barbados were able to be fit to an Angstrom power law in the wavelength range 400 nm to 860 nm.

4.4 AOD and Concentration Correlation Procedure

The optical data were analyzed to determine seasonal patterns and to identify correlations with specific aerosol types and concentrations. The basic procedure was to search both the optical data and the aerosol concentration data for periods that overlapped. The aerosol sampling period was usually one day long, however in some cases the concentration measurement period was several days long. As a result, the optical data were averaged over the length of the aerosol measurement period during the correlation process. For each correlation period, the first step was to determine which aerosol types were present during the comparison period and if one appeared to be dominant. The aerosols of interest during this study were non-sea-salt sulfate (nss $SO_4^{=}$), nitrate (NO_3^-), sea-salt, and mineral dust.

The determination of a dominant aerosol species was based on analysis of the mass concentrations. It must be noted that sea-salt aerosols have a low mass-scattering efficiency MSE [*Li et al.*, 1996] and they are confined to the marine boundary layer. Therefore, the overall contribution of sea salt to the AOD, is generally expected to be much less than the contributions from the other aerosol species. However, the sea-salt concentrations at each location were usually greater than the other aerosol concentrations; therefore, a direct comparison of the concentration levels alone would exaggerate the importance of sea-salt on the optical behavior. To de-emphasize the role of sea-salt aerosols, the other aerosol's concentrations were first compared to that of sea salt. First, the mean mass concentration of each aerosol at the measurement sites was calculated, the results are displayed in Table 3. If the concentration of sea salt was within 30% of it's mean value for the site in question, and the concentration of the other aerosol's was 50% less than that of the sea-salt, then sea-salt was considered to be dominant. If this initial criteria was not met, then sea-salt was excluded from the correlation and the dominant aerosol was chosen from the remaining aerosol species by assigning dominance to the aerosol with a concentration at least 50% greater than that of the other aerosols. If both the sea-salt comparison and the remaining aerosols comparison failed to determine a dominant aerosol, then that period was discarded. If a particular aerosol was found to be dominant then the optical effects recorded during that period were attributed to this aerosol species.

Analysis of the correlated data sets was undertaken to study how the AOD and Angstrom exponents vary during periods of dominance by different aerosol species. Relative increases or decreases in dominant aerosol concentrations from one period to the next should correlate with corresponding increases or decreases in the AOD. Also, long term measurements of the near-surface concentrations of aerosols have shown that individual aerosol types often have characteristic size distributions [*Savoie et al.*, 1982; *Kaufman et al.*, 1994]. Non-sea-salt sulfate particles are primarily found in the submicron range with mass-median diameters generally below 0.5 microns. Dust particles over the ocean (that is, 1000 km or more from the sources) typically have a mass median diameter of several microns or larger, although there is a substantial submicron component [*Li et al.*, 1996]. Sea-salt aerosols also are predominantly supramicron, with a mass median diameter in 4-6 microns. Therefore, periods of non-sea-salt sulfate dominance should contain particles that are primarily submicron and thus should yield a higher Angstrom exponent relative to a period when sea-salt or dust is the dominant aerosol; as in the latter case the particles would primarily be at least several microns in size. It should be noted that another primary anthropogenic aerosol is nitrate. While nitrate aerosols are derived from gaseous precursors, as are non-sea-salt sulfates, in the marine environment the nitrate size distribution follows the surface area of sea-salt aerosols [*Savoie et al.*, 1982] due to a tendency of the nitrate precursors to adsorb into existing sea-salt particles. Also, nitrate concentrations were relatively low at all sites except Miami (Table 3). The majority of Miami periods of high nitrate concentrations correlated with moderate to high sea-salt concentrations. Therefore, nitrate aerosols were not analyzed in the correlation process.

4.5 AOD and Concentration Correlation Results

The monthly averaged AOD at 500 nm, the Angstrom scale factor β, and the Angstrom Exponent α, along with their respective standard deviations (σ_i) are presented for Miami, Bermuda, and Barbados in Tables 4a, 4b, and 4c. The AOD data from Table 4 are displayed for Miami, Bermuda, and Barbados in Figures 3a, 4a, and 5a, respectively. This data is the result of combining the data sets from the sunphotometers and the shadowbands for each site.

Figures 3a, 4a, and 5a show characteristic increases in the AOD during the summer months with minimum AOD values during the winter months. The relative changes in the AOD values for each site are the result of changes in the concentrations of particular aerosol species. Figures 3b, 4b, and 5b display the monthly mean aerosol concentrations at Miami, Bermuda, and Barbados. The high sea-salt concentrations measured at each site are evident. However, as mentioned above, the relative importance of the sea-salt to the AOD is less due to it's low MSE.

The Miami and Barbados concentration data shows the well known influence of Saharan dust transport during the summer months [*Prospero*, 1995]. The summer dust concentrations at each site are much higher than aerosol concentrations from other seasons and thus create high summertime AOD values. The decrease in dust concentrations during the winter, early spring, and late fall, results in sea-salt being the dominant aerosol most of the time. During these periods the AOD is lower due to the low MSE of sea-salt. Miami occasionally experiences non-sea-salt sulfate dominant periods, particularly during the spring and summer, and relatively high AOD values may occur. These sulfate dominant periods often occur during the dust season and therefore analysis of the Angstrom exponent correlations (see below) is necessary to determine which aerosol is primarily responsible for the increase in AOD. Barbados was not significantly impacted by sulfate and it's AOD patterns may be understood solely on the analysis of the sea-salt and dust concentrations.

Bermuda does not show as much seasonal dependence in both AOD and aerosol concentration (except for sea-salt) as the other two sites. Dust concentrations at Bermuda were much lower than at Miami and Barbados, even during the summer months. The relative absence of much dust at Bermuda is the primary reason for the lack of strong seasonal dependence in the AOD. However, Bermuda does have a strong seasonal dependence in the sea-salt concentrations. Sea-salt dominance during the winter and fall months creates low AOD values relative to the spring months. During the spring months, non-sea-salt sulfates from North America are present. The Bermuda sulfate concentrations are lower than those seen at Miami, however, the high MSE of sulfate [*Li et al.*, 1996] creates AOD values that are high relative to the sea-salt induced AOD values at Bermuda. This results in the small seasonal AOD dependence observed for Bermuda.

The Angstrom exponents were correlated with the aerosol concentrations for each site based on the procedure described above. Table 5 displays the mean Angstrom exponent and corresponding standard deviation (σ_α) for each dominant aerosol. There were negative Angstrom exponents calculated at each site. The negative Angstrom exponents were attributed to less accurate Angstrom fitting at low AOD values since 74% of the negative Angstrom exponents correspond to AOD (at 500 nm) below 0.1 in value. The majority of the negative Angstrom exponent, higher AOD (> 0.1) data had exponents only slightly negative (- 0.1 or higher).

The non-sea-salt sulfate dominant periods at both Miami and Bermuda have mean Angstrom exponents of 1.216 and 1.012 respectively. The sea-salt and dust dominant periods at each site have mean Angstrom exponents ranging from 0.205 to 0.585 in magnitude. The high sulfate exponents relative to the sea-salt and dust exponents show the predominance of smaller particles during the sulfate periods. Furthermore, using the standard deviations in Table 5 and combining sea-salt and dust into a "natural" aerosol type it is possible to show the difference between sulfate and natural (sea-salt and dust) aerosol exponents. Based on the analysis above, the Angstrom exponents for sulfate measurements over the ocean range from 0.863 to 1.365 while the Angstrom exponents for natural aerosols over the ocean range from 0.184 to 0.614 in value.

A goal of this research was to determine if it was possible to distinguish between different aerosol species over the ocean based only on analysis of the AOD and Angstrom exponent. As can be seen from analysis of the seasonal dependence of the AOD and aerosol concentrations and correlations with the Angstrom exponent, at the moment it is not generally possible to distinguish between specific aerosol types based solely on analysis of the AOD and Angstrom exponent. However, it is generally possible to distinguish between natural (sea-salt and dust) and sulfate aerosols over the ocean, and in specific cases of high dust concentrations it is also possible to distinguish between sea-salt and dust species over the ocean.

Figures 6a, 6b, and 6c display plots of the AOD versus the Angstrom exponent for Miami, Bermuda, and Barbados. The AOD and exponent values are daily averages of the entire data set for each site. Two characteristic patterns are evident in the figures. In both the Miami and Bermuda plots, the exponents are low at low AOD values. The exponents gradually increase in magnitude with corresponding increases in the AOD until an asymptote in exponent value is reached. The Barbados plot shows what appears to be an opposite pattern; decreasing exponents with increasing AOD values. In addition, there is a small portion of the Miami plot that shows relatively high AOD values with correspondingly low exponents, similar to the Barbados plot. The plots in Figures 6 are redisplayed in Figures 7a, 7b, and 7c after applying the correlational procedure. The data in each plot is segmented according to dominant aerosol type.

The Miami plot shows that the majority of sulfate dominant periods have high AOD values (above 0.2) and high Angstrom exponents (generally greater than 1.0). There is one low exponent sulfate period (below 0.5), but the AOD is much lower. The Miami plot also shows that the sea-salt and dust dominant periods have Angstrom exponents that are mostly below 0.5, as mentioned above. However, it is also evident that several of the dust dominant periods also have high AOD values (approximately 0.2), while there is only one sea-salt dominant period with a high AOD.

The Bermuda plot shows a similar trend, as for Miami, for the sulfate dominant periods. The high AOD sulfate periods coincide with high Angstrom exponents (approximately 1.0). There is also one sulfate period with a low exponent (below 0.5), but this period also corresponds with a lower AOD value, as found in the Miami plot. For the purposes of this discussion, we are concerned only with strong dominant aerosol occurrences and the low sulfate AOD periods are discarded. The Bermuda sea-salt dominant periods are also similar to the Miami sea-salt periods, with lower AOD values (below 0.2) and low exponents (below 1.0). The dust dominant periods in Bermuda correspond with higher Angstrom exponents (mostly between 0.5 and 1.0) than those seen for Miami. However, the dust dominant AOD values for Bermuda are much lower on the average (mostly below 0.1) than for Miami dust dominant periods.

The Barbados plot shows very similar sea-salt dominant period behavior as that seen for Miami. Sea-salt periods have low AOD values (mean around 0.1) and low exponents (below 0.5). The dust dominant periods for Barbados show a clear pattern of decreasing Angstrom exponents with increasing AOD. As in Miami, high dust period AOD values (above 0.2) correspond to low exponents (below 0.5). The lower dust period AOD values (near 0.1) have higher Angstrom exponents (above 0.5), similar to the dust dominant trend shown for Bermuda.

General statements may be made by combining the results from each site. Figure 8 shows the AOD plotted versus the Angstrom exponent for each dominant aerosol period from all the sites. In general, strong non-sea-salt sulfate dominant periods are characterized by AOD values from 0.2 to 0.3, and Angstrom exponents from 1.0 to 1.5 in magnitude. In contrast to the sulfate periods, nearly all sea-salt dominant periods have AOD values from 0.1 to 0.2, and Angstrom exponents from 0.0 to 1.0 in magnitude. The dust dominant periods range in AOD from below 0.1 to just under 0.4 in value, and the majority of Angstrom exponents range from 0.0 to 1.0 in magnitude. The sea-salt and dust dominant periods overlap in both AOD and Angstrom exponent values for most ranges in question, and therefore are not easily distinguished. Both sea-salt and dust dominant periods do not show the same characterization in AOD and Angstrom exponent as do sulfate dominant periods, therefore it is possible to distinguish strong non-sea-salt sulfate dominant periods from sea-salt and dust periods based only on the analysis of the AOD and Angstrom exponents.

The dust dominant periods show a characteristic trend in the AOD and Angstrom exponent. Dust dominant periods show that the Angstrom exponents are higher (from 0.5 to 1.0) for lower AOD values from 0.1 to 0.2, and that the exponents decrease in magnitude (to below 0.5) as the AOD increases to above 0.2 in value. This is equivalent to saying that on the average, the dust Angstrom exponents decrease rapidly as the dust concentration increases. This same trend does not occur for sea-salt dominant periods. Therefore, it is possible to distinguish strong dust periods from sea-salt periods because the sea-salt AOD values do not normally reach above 0.2 in magnitude. AOD values above 0.2 and corresponding Angstrom exponents below 0.5 in magnitude are a strong indication of dust dominance.

The ability to identify strong non-sea-salt sulfate dominant periods over the ocean by analysis of only the AOD and Angstrom exponent has been demonstrated. Also, the ability to distinguish strong dust dominant periods from normal sea-salt dominant periods has also been shown. The characteristic AOD and Angstrom exponent values that may be used to identify particular aerosol species over the ocean are summarized in Table 6.

5. Conclusions

The results of AOD analysis for Miami, Bermuda, and Barbados over approximately a two and a half year period of time have been presented. Together, the three sites provide good spatial coverage for the western half of the tropical North Atlantic Ocean. Also, the time period of over two years allows for good temporal coverage which is essential for proper seasonal studies. The results obtained from this work agree well with other AOD data sets taken in the North Atlantic region. For instance, the seasonality of average AOD values exhibited in the AVHRR AOD values [*Husar et al.*, 1997] over the Caribbean and along the coast of the Southeast United States agrees with our data set.

The results obtained from correlations of the AOD with the aerosol concentrations also agree well with work done by other researchers that involved correlating AOD measurements over the ocean with air mass trajectories. Reddy et al. [1990] and Smirnov et al. [1995] have shown that air mass types from continental northern regions (such as the United States) produce high AOD (approximately 0.2) and high Angstrom exponents (> 1.0) when they move over the ocean. This result agrees well with the AOD and Angstrom exponents obtained in this work during non-sea-salt sulfate dominant periods. Also, AOD and Angstrom exponents presented by Smirnov et al. [1995] for a tropical maritime air mass (AOD ~ 0.15, α ~ 0.42) are similar to those found in this work during sea-salt dominant periods. Finally, AOD and Angstrom exponents from Reddy et al. [1990] for air masses from, or influenced by, the Saharan region (AOD ~ 0.39, α ~ 0.37; AOD ~ 0.13, α ~ 0.77), produce AOD and Angstrom exponents similar to those found in this work for dust dominant periods.

There are three primary conclusions drawn from this analysis. The first is that the spectral variation of the AOD over each site may be represented by the Angstrom power law. The second is that characteristic seasonal patterns in the AOD at each site are present and are caused primarily by seasonal changes in the types and concentrations of the aerosol species. Finally, it is possible to distinguish between different aerosol species over the ocean by analyzing the spectral variation of the AOD, particularly during strong periods of dominance by a single aerosol species.

The recent launch of ocean viewing satellite sensors such as SeaWiFS and the upcoming launch of the MODIS sensor on the EOS-AM satellite are used to determine the ocean color by measuring upwelling sunlight from the ocean. However, the sun's radiance must pass through the atmosphere before reaching the sensor. The measured radiances must be corrected for atmospheric effects in order to calculate the ocean color. An overview of atmospheric correction algorithms may be found in Gordon [1997]. The basic procedure for both single and multiple scattering algorithms involves the determination of the correction factor ε [*Gordon*, 1997] at blue wavelengths after calculating ε in the near infared (NIR). The high degree to which the AOD measurements at each site resembled an Angstrom power law in the visible and NIR means it is possible that, for ocean color correction, the spectral variation of ε can be modeled using power-law size distributions [*Chomko and Gordon*, 1998].

The seasonal variability of the AOD must be understood to properly analyze the optical data and when using AOD for other secondary purposes, such as input to climate models and atmospheric correction algorithms. For instance, use of a typical AOD measured during a mid-summer Saharan dust passage, would not be representative of normal year-round conditions over the tropical North Atlantic Ocean. These types of problems may be avoided by proper understanding of the seasonal AOD changes. For instance, it would be best to use a typical AOD measured during mid-winter for climate studies and correction algorithms used to model normal open ocean conditions, and to use a typical AOD from mid-summer to study the pertubative effects of Saharan dust over the North Atlantic Ocean. Also, the use of correct AOD values, and hence the correct aerosol model, based on the understanding of seasonal changes in the aerosol species will improve the determination of the ocean color correction factor ε.

The measurement of spectral AOD from the ground is a relatively well known procedure, and surface based measurements of the AOD over the ocean are increasing in number as more attention is focused on understanding the climatic effects of aerosols on a global scale. Many of the sensors on upcoming satellites are capable of producing AOD values at, or near, the spectral variety of ground-based sensors. Also, satellite AOD measurements are performed only for cloud-free areas, and therefore, like surface AOD measurements, the resulting data should not be effected by cloud processing of the aerosol. Combination of both ground-based and satellite spectral AOD measurements will produce much needed global data of the AOD and Angstrom exponent, particularly over the oceans. The identification of specific aerosol species based on the analysis of the AOD and Angstrom exponent has been shown in this study. The ability to identify aerosol species from analysis of other ground-based and satellite derived spectral AOD and the criteria in Table 6 will complement other current satellite aerosol identification programs, such as the TOMS aerosol index product [*Herman et al.*, 1997].

Future work will involve examining the transport patterns and source locations for the aerosol species investigated in this study. Also, the criteria developed in this work for identifying aerosol species based on measurements of the spectral AOD (Table 6) will be used to aid in analyzing data taken at the AERONET Cimel sunphotometer [*Holben et al.*, 1994] site in the Dry Tortugas, Florida.

Acknowledgements

The authors would like to thank the following people: Albert Chapin and Derrick Snowden for help in performing sunphotometer measurements and calibrations; Miguel Izaguirre and Tom Snowden for help in arranging site communications and logistics; Hal Maring, and Xu Li for providing useful information on aerosol measurement techniques and various aerosol properties; Joe Michalsky and Lee Harrison for providing much needed information and suggestions on performing shadowband measurements; Alexander Ignatov for providing information on the procedure used to correct the shadowband calibrations; Jim Schlemmer for providing the algorithm to the SUNY Sliding Window Optical Depth Procedure; and AEROCE site operators Anne Glasspool, Cornealius Shea, Matthew Krasowski, Megan McKay, H. B. Gooding, and Dr. F. Henriques for help in maintaining the on-site instruments. The optical measurements were funded by NASA contract #NA55-31363, and NOAA grant #NA16RCO471-01. The aerosol chemistry measurements were made under National Science Foundation grants ATM9013125 and ATM9414846.

References

d'Almeida, G.A., P. Koepke, and E.P. Shettle, *Atmospheric Aerosols: Global Climatology and Radiative Characteristics*, A. Deepak Pub., Hampton, Virginia, 1991.

Angstrom, A., The parameters of atmospheric turbidity, *Tellus*, 16, 64-75, 1964.

Arimoto, R, R.A. Duce, D.C. Savoie, J.M. Prospero, R. Talbot, J.D. Cullen, U. Tomza, N.F. Lewis, and B.J. Ray, Relationship among aerosol constituents from Asia and the North Pacific during PEM-West A, *J. Geophys. Res.*, 101, 2011-2023, 1996.

Charlson, R.J., S.E. Schwartz, J.M. Hales, R.D. Cess, J.A. Coakley Jr., J.E. Hansen, and D.J. Hofmann, Climate forcing by anthropogenic aerosols, *Science*, 255, 423-430, 1992.

Chomko, R., and H. Gordon, Atmospheric correction of ocean color imagery: Use of the Junge power-law aerosol size distribution with variable refractive index to handle aerosol absorption, (In Press) *Appl. Optics*, 1998.

Dutton, E.G., P. Reddy, S. Ryan, and J. DeLuisi, Features and effects of aerosol optical depth observed at Mauna Loa, Hawaii: 1982-1992, *J. Geophys. Res.*, 99, 8295-8306, 1994.

Gordon, H.R., Atmospheric correction of ocean color imagery in the Earth Observing System era, *J. Geophys. Res.*, 102, 17081-17106, 1997.

Hansen, J.E., and L.D. Travis, Light scattering in planetary atmospheres, *Space Sci. Reviews*, 16, 527-610, 1974.

Harrison, L., J. Michalsky, and J. Berndt, The Automated multi-filter rotating shadow-band radiometer: An instrument for optical depth and radiation measurements, *Appl. Optics,* 33, 5118-5125, 1994.

Harrison, L., and J. Michalsky, Objective algorithms for the retrieval of optical depths from ground-based measurements, *Appl. Optics*, 33, 5126-5132, 1994.

Herman, J.R., P. Bhartia, O. Torres, C. Hsu, C. Seftor, and E. Celarier, Global distribution of UV-absorbing aerosols from Nimbus-7/TOMS data, *J. Geophys. Res.*, 102, 16911-16922, 1997.

Holben, B.N., T.F. Eck, I. Slutsker, D. Tanre, J.P. Buis, A. Setzer, E. Vermote, J.A. Reagan, Y.J. Kaufman, T. Nakajima, and F. Lavenu, Multi-band automatic sun and sky scanning radiometer system for measurement of aerosols, *Proc. Sixth International Symposium Physical on Measurements and Signatures in Remote Sensing*, 75-83, 1994.

Hoppel, W.A., J. Fitzgerald, G. Frick, R. Larson, and E. Mack, Aerosol Size Distributions and Optical Properties Found in the Marine Boundary Layer Over the Atlantic Ocean,*J. Geophys. Res.*, 95, 3659-3686, 1990.

Husar, R.B., J.M. Prospero, L.L. Stowe, Characterization of tropospheric aerosols over the oceans with the NOAA advanced very high resolution radiometer optical thickness operational product, *J. Geophys. Res.*, 102, 16889-16909, 1997.

Ignatov, A, *Personal Communication*, NOAA NESDIS ORA, Washington D.C., 20233, 1996.

Kasten, F., and A.T. Young, Revised optical air mass tables and approximation formula, *Appl. Optics*, 28, 4735-4738, 1989.

Kaufman, Y.J., Aerosol optical thickness and atmospheric path radiance, *J. Geophys. Res.*, 98, 2677-2692, 1993.

Kaufman, Y.J., A. Gitelson, A. Karnieli, E. Ganor, R.S. Fraser, T. Nakajima, S. Mattoo, and B.N. Holben, Size distribution and scattering phase function of aerosol particles retrieved from sky brightness measurements, *J. Geophys. Res.*, 99, 10341-10356, 1994.

King, M.D., D. Byrne, B. Herman, and J. Reagan, Aerosol size distributions obtained by inversion of spectral optical depth measurements, *J. Atmos. Sci.*, 35, 2153-2167, 1978.

King, M., D. Byrne, J. Reagan, and B. Herman, Spectral variation of optical depth at Tucson Arizona between August 1975 and December 1977, *J. Appl. Meteorol.*, 19, 16,639-16,650, 1980.

Klenk, K., P. Bhartia, E. Hilsenrath, and A. Fleig, Standard ozone profiles from balloon and satellite data sets, *J. Clim. Appl. Meteorol.*, 22, 2012-2022, 1983.

Li, X., H. Maring, D. Savoie, K. Voss, and J. Prospero, Dominance of Mineral Dust in Aerosol Light-Scattering in the North Atlantic Trade Winds, *Nature*, 380, 416-419, 1996.

Prospero, J.M., Saharan dust transport over the north Atlantic Ocean and Mediterranean, Chapter in*The Impact of Desert Dust From Northern Africa Across the Mediterranean*, Kluwer Academic Publishers, Oristano, Sardinia, 1995.

Reddy, P.J., F.W., Kreiner, J.J. DeLuisi, and Y. Kim, Aerosol Optical Depths Over the Atlantic Derived From Shipboard Sunphotometer Observations During the 1988 Global Change Expedition, *Global Biogeochem. Cycles*, 4, 225-240, 1990.

Savoie, D., and J. Prospero, Particle Size Distributions of Nitrate and Sulfate in the Marine Atmosphere, *Geophys. Res. Lett.*, 9, 1207-1210, 1982.

Savoie, D., Nitrate and non-sea-salt sulfate aerosols over major regions of the world oceans: concentrations, sources, and fluxes, *Ph.D. Dissertation*, Rosenstiel School of Marine and Atmospheric Science, University of Miami, 4600 Rickenbacker Causeway, Miami, Fl, 33149, 1984.

Savoie, D., J.M. Prospero, and E.S. Saltzman, Non-sea-salt sulfate and nitrate in trade wind aerosols at Barbados: evidence for long-range transport, *J. Geophys. Res.*, 94, 5069-5080, 1989.

Schlemmer, J., *Personal Communication*, Atmospheric Sciences Research Center, SUNY Albany, NY, 12205, 1996.

Shaw, G.E., Aerosols at Mauna Loa: Optical properties, *J. Atmos. Sci.*, 36, 862-869, 1979.

Smirnov, A., A. Royer, N. O'Neill, and A. Tarussov, A study of the link between synoptic air mass type and atmospheric optical parameters, *J. Geophys. Res.*, 99, 20967-20982, 1994.

Smirnov, A., Y. Villevalde, N. O'Neill, A. Royer, and A. Tarussov, Aerosol optical depth over the oceans: Analysis in terms of synoptic air mass types, *J. Geophys. Res.*, 100, 16639-16650, 1995.

Van de Hulst, H. C., *Light Scattering by Small Particles*, Dover Publications Inc., New York, NY, 1981.

Villevalde, Y.V., A.V. Smirnov, N.T. O'Neill, S.P. Smyshlyaev, and V.V. Yakovlev, Measurement of aerosol optical depth in the Pacific Ocean and the North Atlantic, *J. Geophys. Res.*, 99, 20983-20988, 1994.

Table 1

Location	Time Period
Miami, Florida Lat: 25.75 N Lon: 80.2 W Altitude: Sea Level	August 1993 to December 1995
Bermuda Lat: 32.38 N Lon: 64.7 W Altitude: Sea Level	August 1993 to December 1995
Barbados Lat: 13.18 N Lon: 59.43 W Altitude: Sea Level	August 1993 to December 1995

Table 2

Channel Number	Sunphotometer Filter Wavelength (nm)	Shadowband Filter Wavelength (nm)
1	380.2	Unfiltered (Broadband)
2	412.2	410
3	440.5	500
4	501.8	610
5	551.2	665
6	675.2	860
7	777.9	940
8	861.8	-
9	1025.9	-

Table 3

Location	nss Sulfate ($\mu g/m^3$)	Nitrate ($\mu g/m^3$)	Sea Salt ($\mu g/m^3$)	Dust ($\mu g/m^3$)
Miami	2.202	2.090	8.892	5.633
Bermuda	1.783	0.979	11.412	2.056
Barbados	0.765	0.599	19.997	14.864

Table 4a Monthly Miami AOD Results

Month-Year	$\bar{\tau}_{A_{500}}$	σ_τ	$\bar{\beta}$	σ_β	$\bar{\alpha}$	σ_α
Aug-93	-	-	-	-	-	-
Sep-93	0.114	0.024	0.070	0.022	0.734	0.228
Oct-93	0.142	0.068	0.069	0.020	0.976	0.374
Nov-93	0.142	0.020	0.080	0.011	0.833	0.001
Dec-93	0.121	0.034	0.050	0.013	1.269	0.056
Jan-94	0.121	0.030	0.071	0.005	0.740	0.398
Feb-94	0.120	0.035	0.083	0.035	0.566	0.375
Mar-94	0.151	0.073	0.069	0.030	1.063	0.240
Apr-94	0.166	0.038	0.104	0.035	0.706	0.553
May-94	0.243	0.091	0.111	0.033	1.098	0.319
Jun-94	0.163	0.058	0.128	0.057	0.217	0.457
Jul-94	0.234	0.055	0.209	0.034	0.148	0.100
Aug-94	0.075	0.013	0.059	0.011	0.347	0.319
Sep-94	0.127	0.058	0.079	0.026	0.524	0.773
Oct-94	0.119	0.054	0.056	0.027	0.987	0.509
Nov-94	0.093	0.039	0.049	0.014	0.762	0.713
Dec-94	0.097	0.041	0.093	0.019	-0.246	0.820
Jan-95	0.091	0.032	0.059	0.017	0.443	0.579
Feb-95	0.115	0.049	0.062	0.024	0.846	0.501
Mar-95	0.118	0.020	0.065	0.010	0.768	0.284
Apr-95	0.143	0.037	0.094	0.019	0.480	0.311
May-95	0.288	0.078	0.108	0.023	1.294	0.199
Jun-95	-	-	-	-	-	-
Jul-95	0.165	0.053	0.103	0.030	0.494	0.565
Aug-95	0.148	0.077	0.100	0.043	0.347	0.557
Sep-95	-	-	-	-	-	-
Oct-95	-	-	-	-	-	-
Nov-95	-	-	-	-	-	-
Dec-95	0.099	0.032	0.045	0.016	1.110	0.565
Total	0.141	0.050	0.084	0.034	0.684	0.367

Table 4b Monthly Bermuda AOD Results

Month-Year	$\bar{\tau}_{A_{500}}$	σ_τ	$\bar{\beta}$	σ_β	$\bar{\alpha}$	σ_α
Aug-93	-	-	-	-	-	-
Sep-93	0.161	0.043	0.104	0.015	0.603	0.290
Oct-93	0.161	0.041	0.103	0.020	0.622	0.232
Nov-93	0.117	0.025	0.081	0.018	0.540	0.214
Dec-93	0.160	0.037	0.102	0.009	0.614	0.304
Jan-94	0.099	0.012	0.069	0.011	0.531	0.298
Feb-94	0.102	0.023	0.079	0.005	0.322	0.372
Mar-94	0.157	0.041	0.099	0.026	0.666	0.268
Apr-94	0.169	0.050	0.105	0.022	0.667	0.415
May-94	0.134	0.047	0.085	0.030	0.655	0.259
Jun-94	0.270	0.125	0.170	0.072	0.599	0.233
Jul-94	0.116	0.072	0.081	0.045	0.474	0.179
Aug-94	0.126	0.131	0.097	0.125	0.424	0.334
Sep-94	0.100	0.061	0.049	0.035	1.058	0.746
Oct-94	0.075	0.041	0.060	0.015	0.288	0.663
Nov-94	0.068	0.021	0.077	0.016	-0.209	0.351
Dec-94	0.064	0.028	0.085	0.033	-0.920	0.973
Jan-95	0.081	0.035	0.075	0.023	-0.236	0.817
Feb-95	0.104	0.027	0.059	0.025	0.697	0.616
Mar-95	0.091	0.050	0.068	0.023	0.108	0.416
Apr-95	0.172	0.077	0.095	0.034	0.818	0.187
May-95	0.168	0.057	0.088	0.030	0.851	0.318
Jun-95	0.134	0.069	0.072	0.024	0.558	0.659
Jul-95	-	-	-	-	-	-
Aug-95	-	-	-	-	-	-
Sep-95	-	-	-	-	-	-
Oct-95	-	-	-	-	-	-
Nov-95	-	-	-	-	-	-
Dec-95	-	-	-	-	-	-
Total	0.129	0.047	0.086	0.025	0.442	0.433

Table 4c Monthly Barbados AOD Results

Month-Year	$\bar{\tau}_{A_{500}}$	σ_τ	$\bar{\beta}$	σ_β	$\bar{\alpha}$	σ_α
Aug-93	-	-	-	-	-	-
Sep-93	-	-	-	-	-	-
Oct-93	0.078	0.033	0.059	0.029	0.442	0.166
Nov-93	0.072	0.019	0.055	0.021	0.483	0.256
Dec-93	0.064	0.006	0.051	0.015	0.360	0.322
Jan-94	0.084	0.029	0.071	0.022	0.262	0.180
Feb-94	0.129	0.057	0.097	0.055	0.508	0.446
Mar-94	0.078	0.058	0.064	0.056	0.605	0.674
Apr-94	0.184	0.157	0.167	0.156	0.275	0.245
May-94	0.201	0.151	0.167	0.102	0.256	0.245
Jun-94	0.247	0.095	0.224	0.084	0.148	0.139
Jul-94	0.362	0.128	0.267	0.111	0.504	0.225
Aug-94	0.210	0.067	0.132	0.055	0.731	0.211
Sep-94	0.169	0.090	0.118	0.076	0.640	0.287
Oct-94	-	-	-	-	-	-
Nov-94	-	-	-	-	-	-
Dec-94	-	-	-	-	-	-
Jan-95	-	-	-	-	-	-
Feb-95	-	-	-	-	-	-
Mar-95	-	-	-	-	-	-
Apr-95	-	-	-	-	-	-
May-95	-	-	-	-	-	-
Jun-95	0.257	0.107	0.260	0.108	0.014	0.059
Jul-95	0.144	0.060	0.147	0.063	0.047	0.187
Aug-95	0.200	-	0.176	-	0.138	-
Sep-95	-	-	-	-	-	-
Oct-95	-	-	-	-	-	-
Nov-95	-	-	-	-	-	-
Dec-95	-	-	-	-	-	-
Total	0.165	0.085	0.137	0.073	0.361	0.220

Table 5

Location - Dominate Aerosol	α	σ_α
Miami - nss Sulfate	1.216	0.209
Bermuda - nss Sulfate	1.012	0.292
Miami - Sea Salt	0.205	0.202
Bermuda - Sea Salt	0.580	0.376
Barbados - Sea Salt	0.406	0.080
Miami - Dust	0.280	0.235
Bermuda - Dust	0.585	0.127
Barbados - Dust	0.339	0.268

Table 6

AOD (500 nm)	Angstrom Exponent	Primary Aerosol Species
0.0 - 0.2	0.0 - 0.5	sea-salt or dust
	> 0.5	indeterminate
> 0.2	0.0 - 0.5	dust
	0.5 - 1.0	indeterminate
	> 1.0	non-sea-salt sulfate

Figure 1a

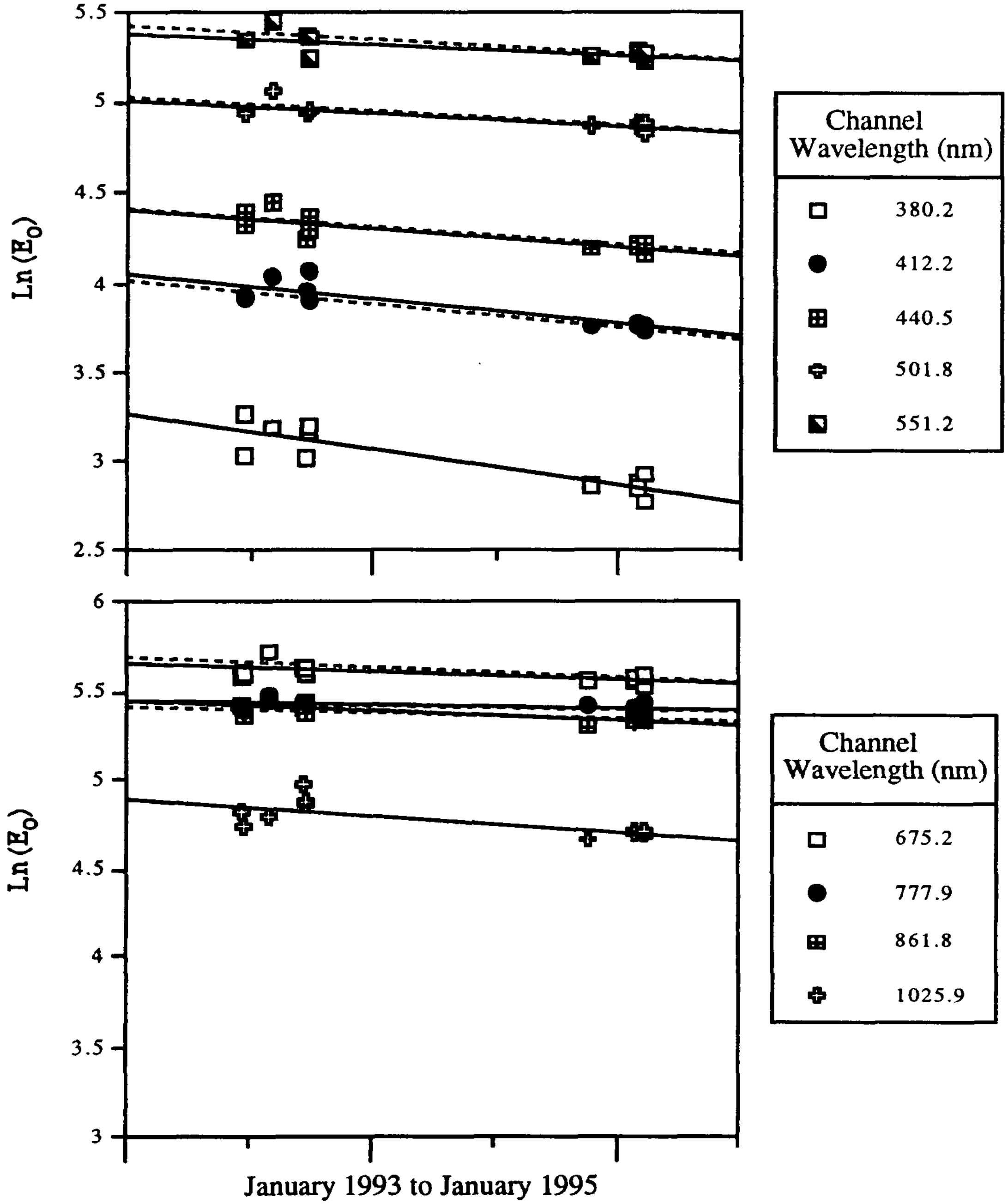

Figure 1a. Calibration history for the Miami sunphotometer. The solid line is the fit to the Langley and cross-calibrations. The dotted line is the fit to the error corrected calibrations.

Figure 1b

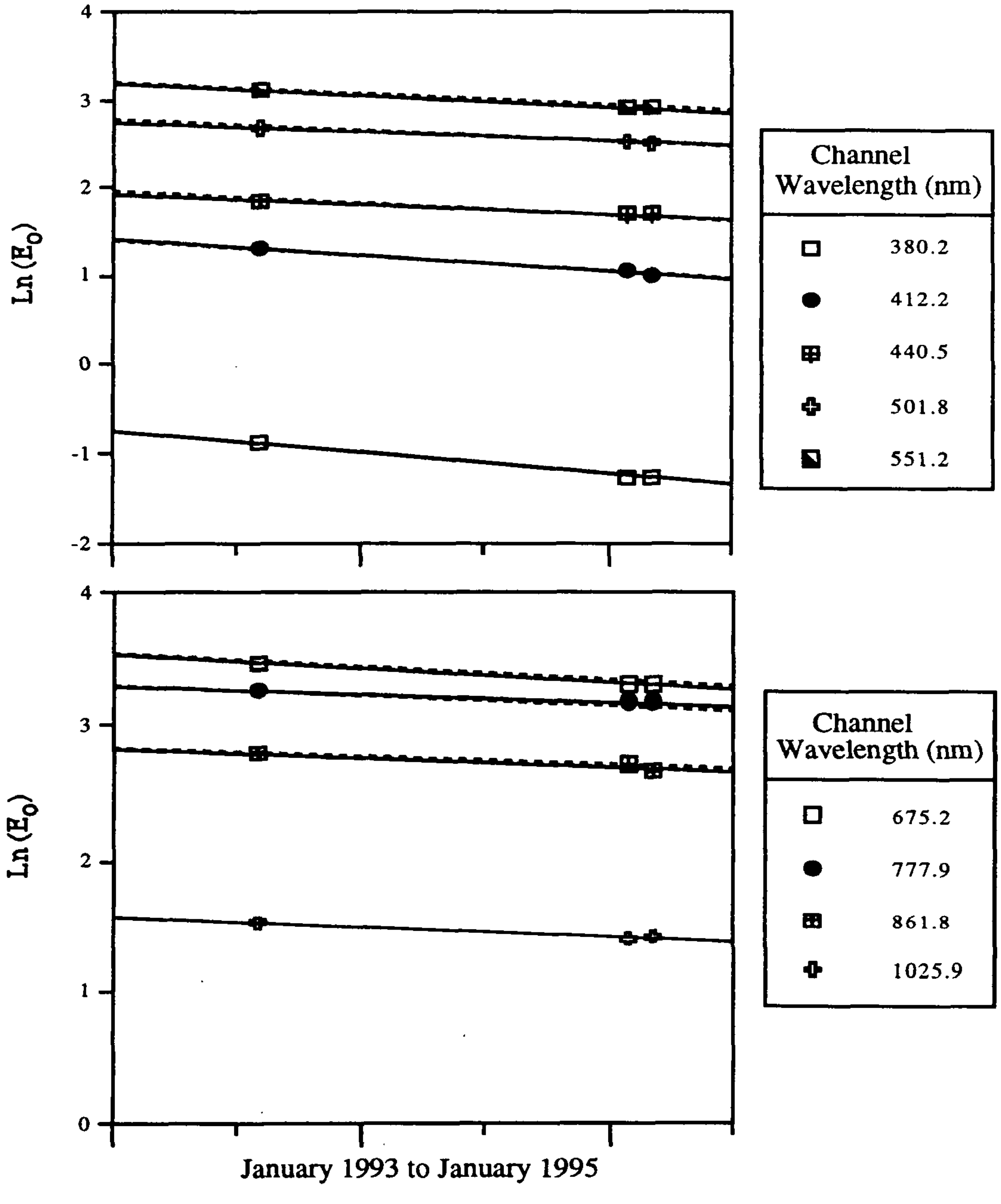

Figure 1b. Calibration history for the Bermuda sunphotometer. The solid line is the fit to the Langley and cross-calibrations. The dotted line is the fit to the error corrected calibrations.

Figure 1c

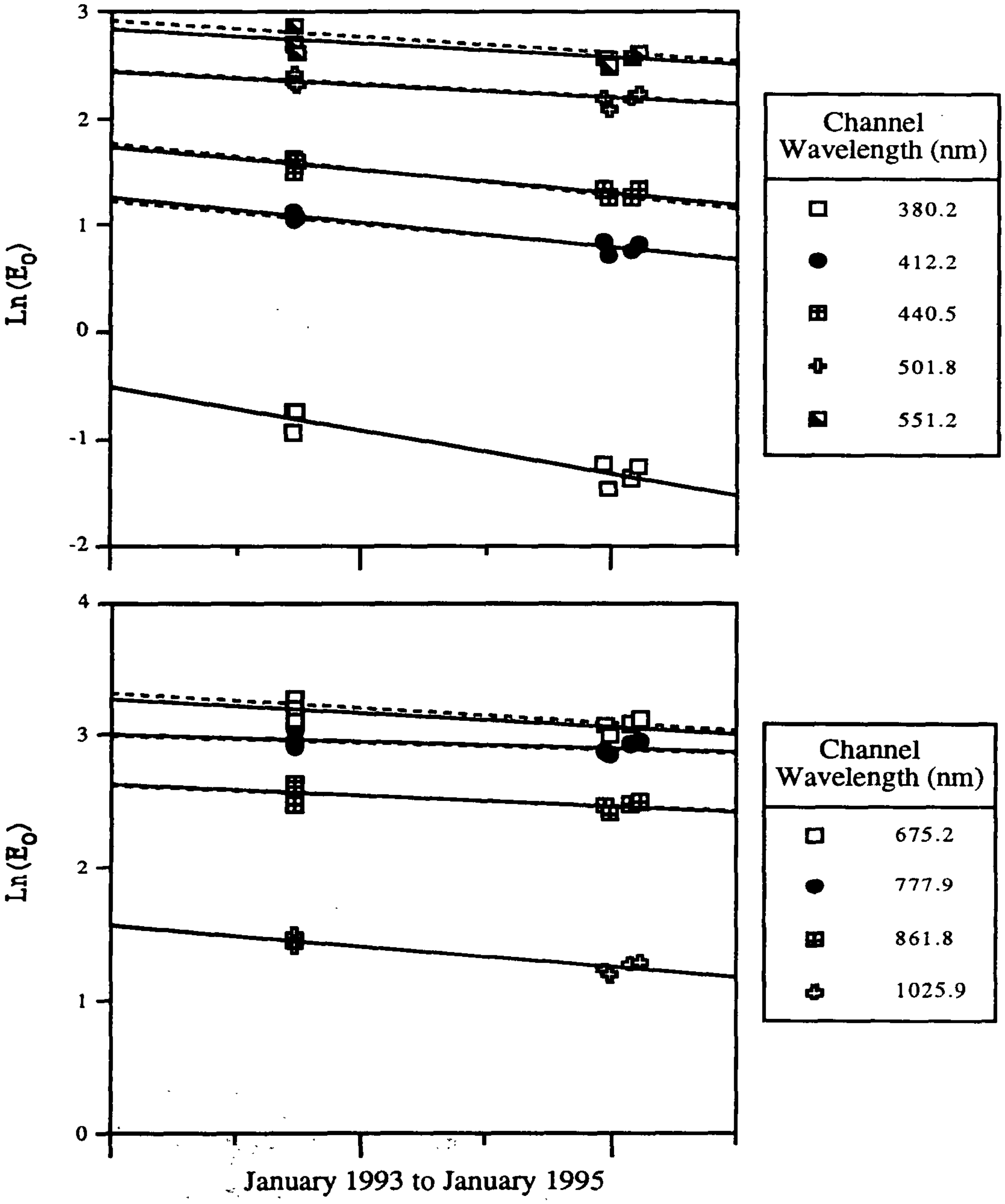

Figure 1c. Calibration history for the Barbados sunphotometer. The solid line is the fit to the Langley and cross-calibrations. The dotted line is the fit to the error corrected calibrations.

Figure 2a

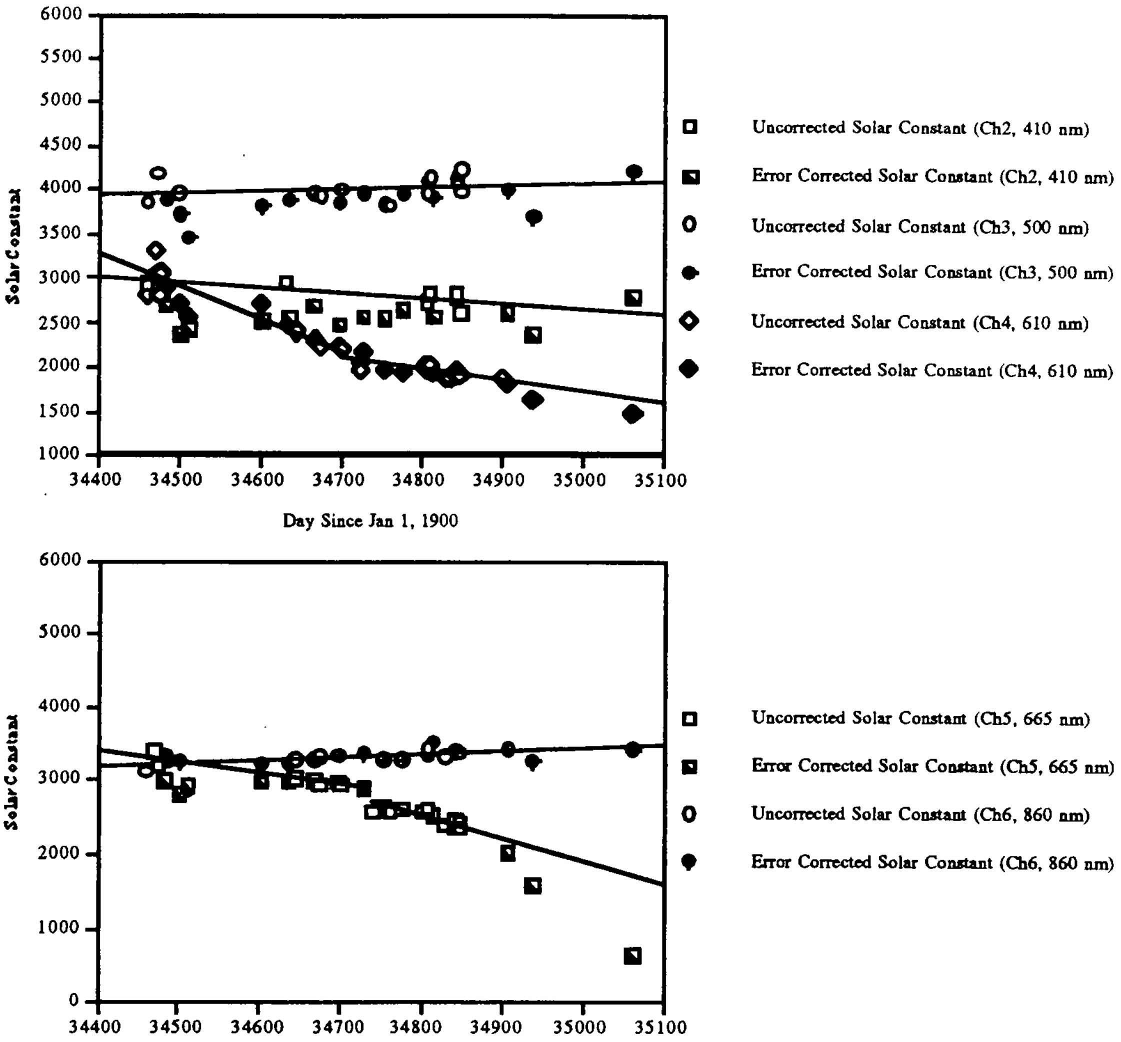

Figure 2a. Calibration history for the Miami shadowband (May 1994 to December 1995). The solid line is the fit to the OLRA Langley calibrations.

Figure 2b

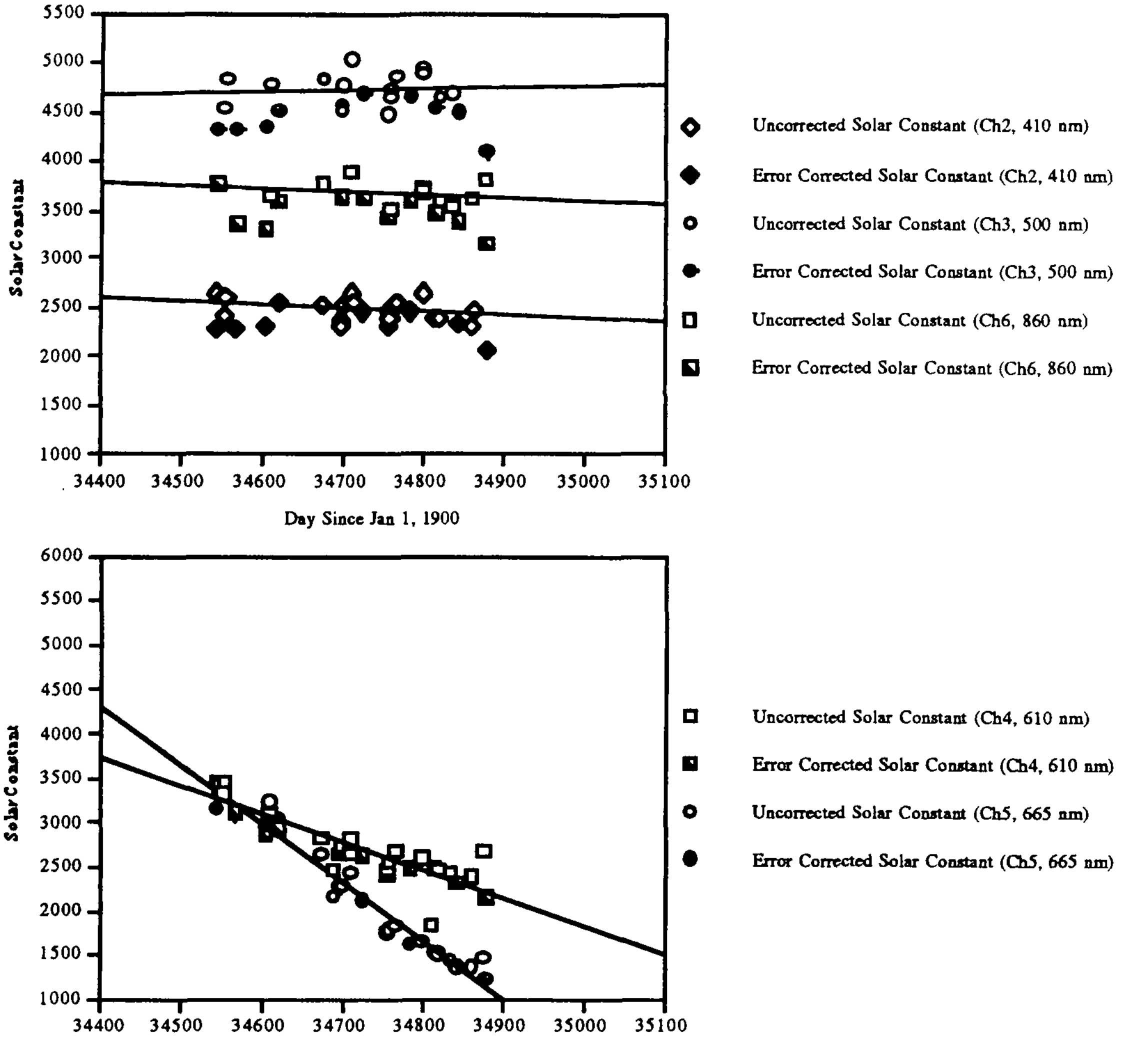

Figure 2b. Calibration history for the Bermuda shadowband (May 1994 to December 1995). The solid line is the fit to the OLRA Langley calibrations.

Figure 2c

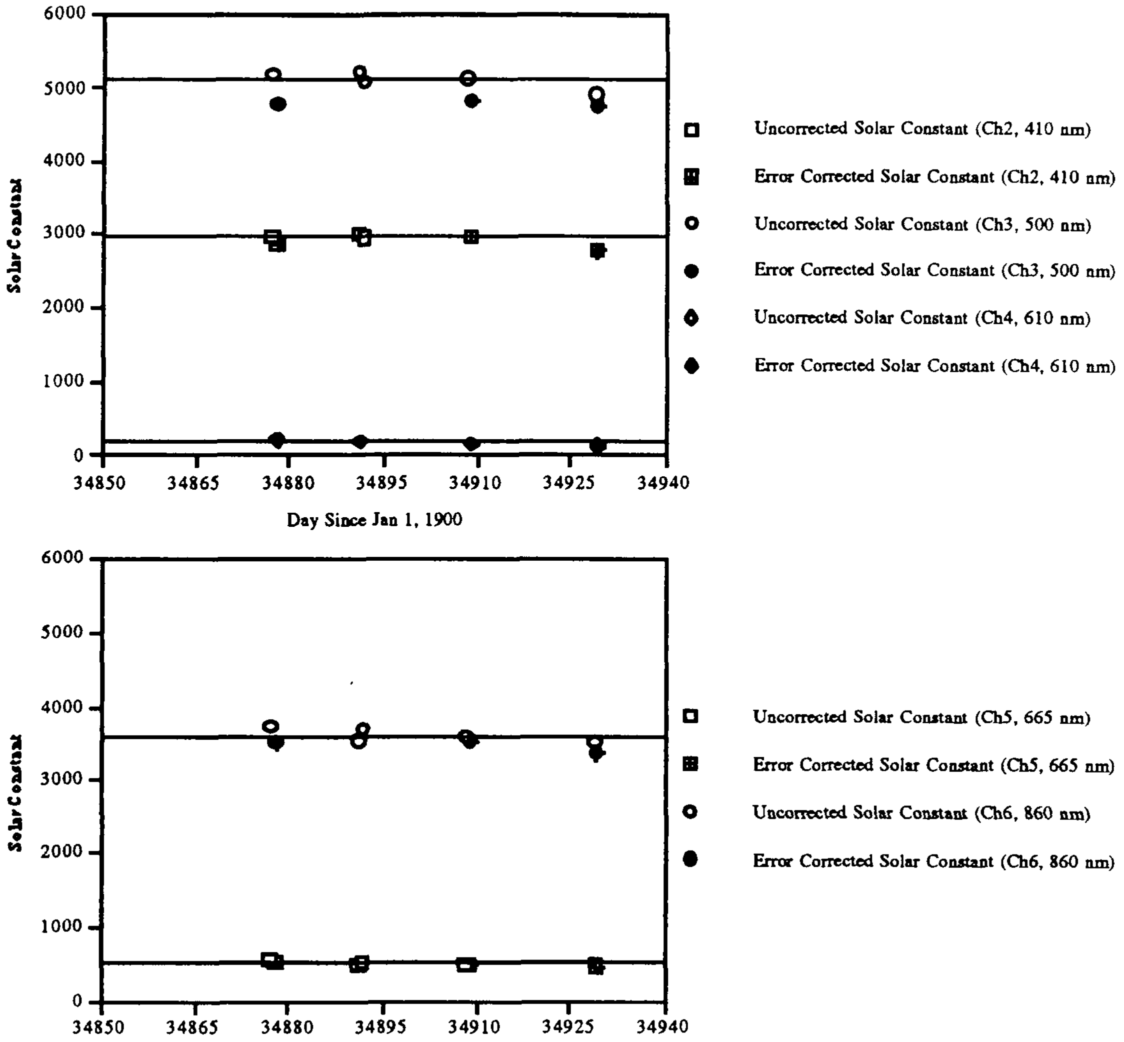

Figure 2c. Calibration history for the Barbados shadowband (June 1995 to August 1995). The solid line is the fit to the OLRA Langley calibrations.

Figure 3a

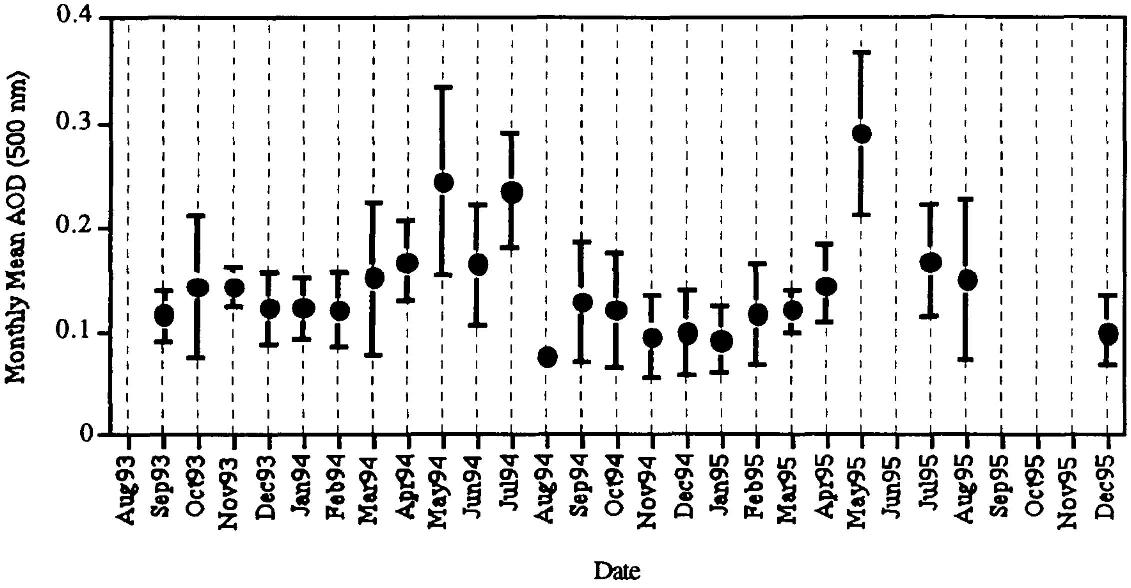

Figure 3a. Miami monthly mean AOD (500 nm) and corresponding standard deviations from August 1993 to December 1995.

Figure 3b

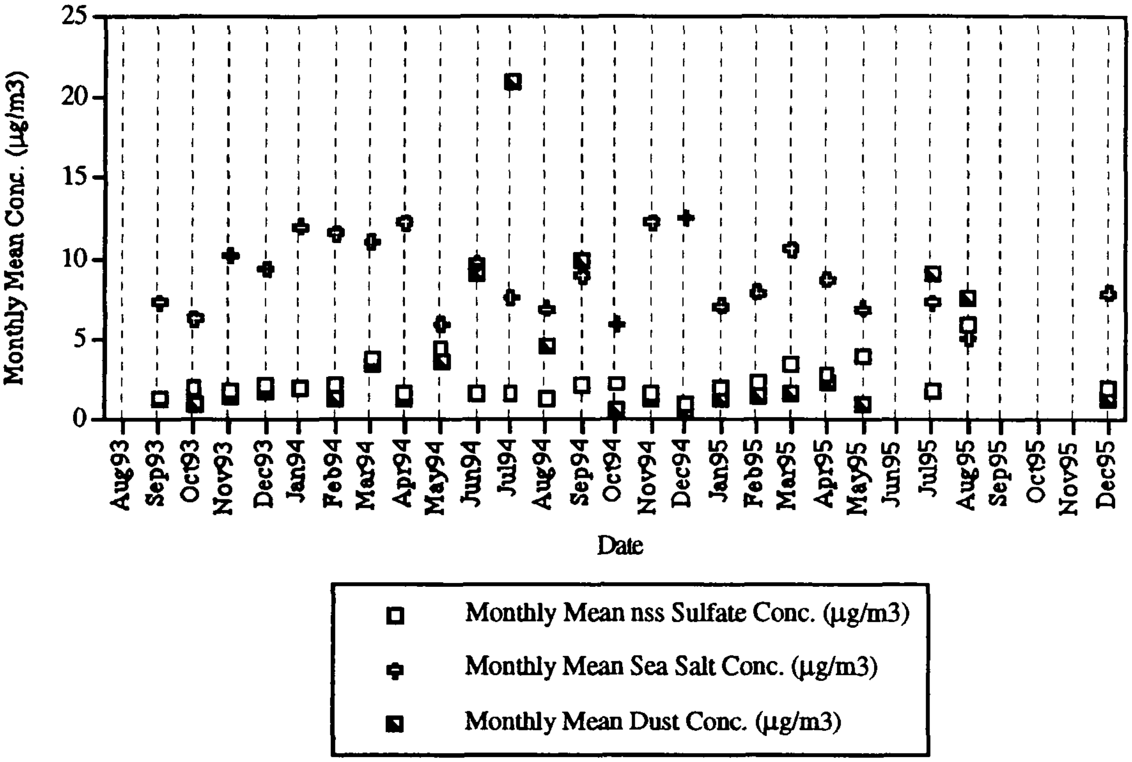

Figure 3b. Miami monthly mean aerosol concentrations from August 1993 to December 1995.

Figure 4a

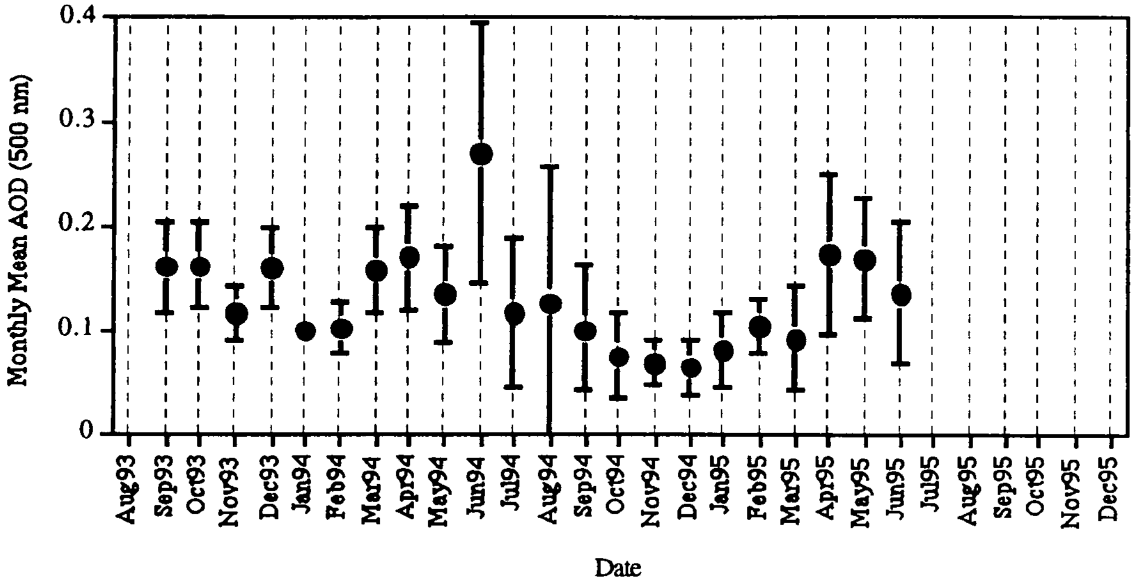

Figure 4a. Bermuda monthly mean AOD (500 nm) and corresponding standard deviations from August 1993 to December 1995.

Figure 4b

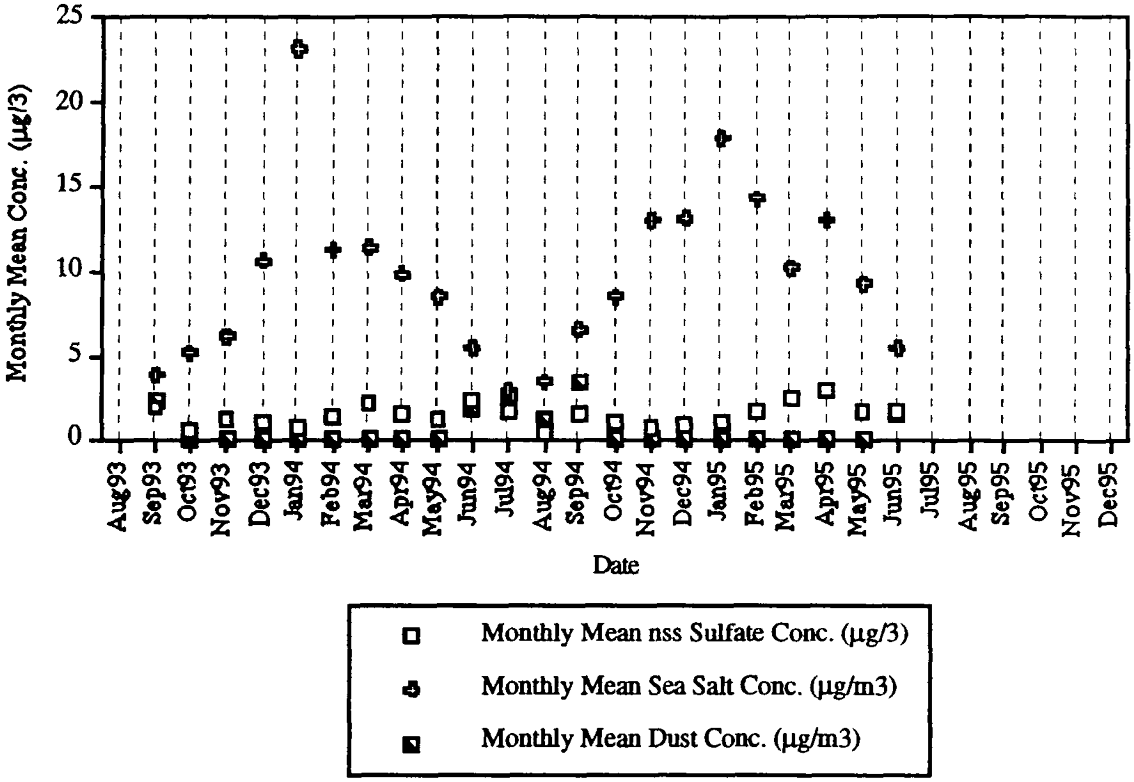

Figure 4b. Bermuda monthly mean aerosol concentrations from August 1993 to December 1995.

Figure 5a

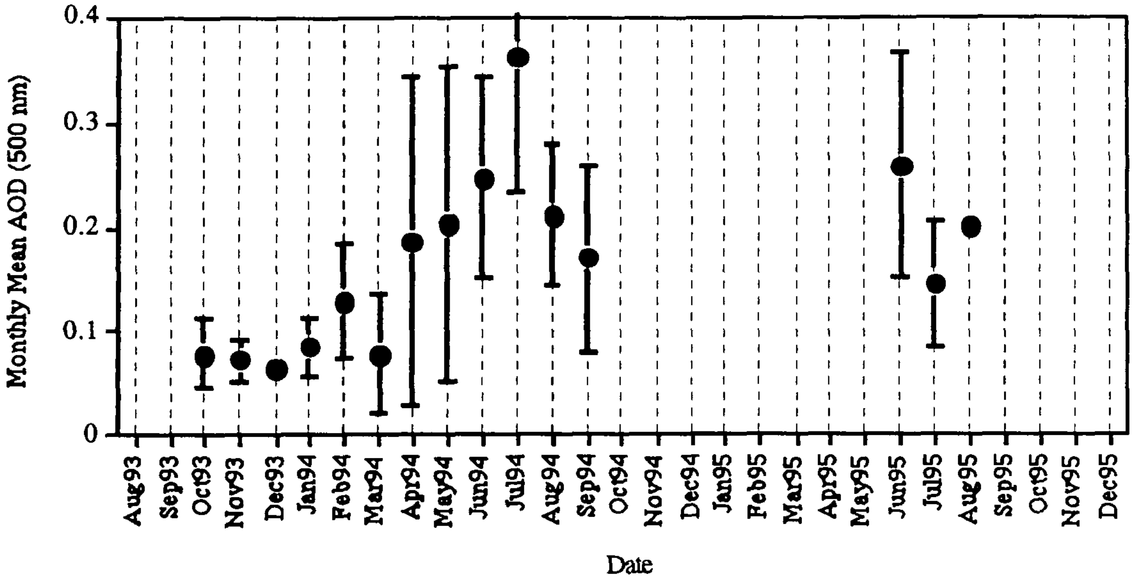

Figure 5a. Barbados monthly mean AOD (500 nm) and corresponding standard deviations from August 1993 to December 1995.

Figure 5b

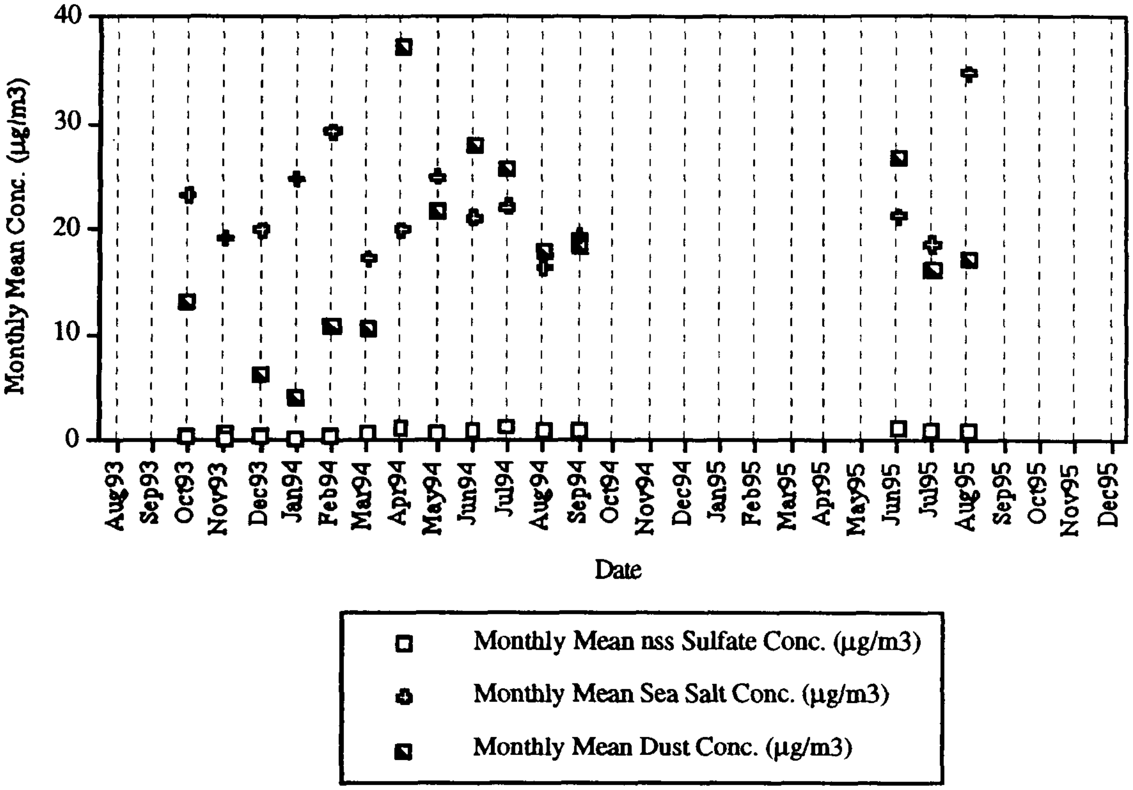

Figure 5b. Barbados monthly mean aerosol concentrations from August 1993 to December 1995.

Figure 6a

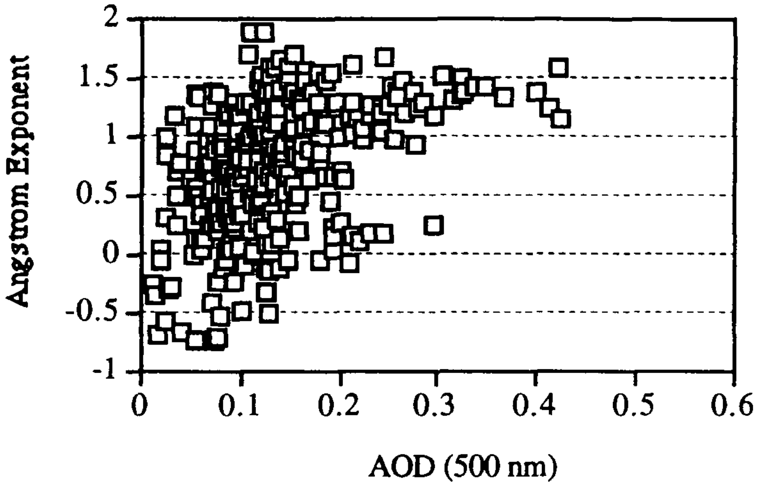

Figure 6a. Miami daily averaged AOD (500 nm) versus the Angstrom exponent.

Figure 6b

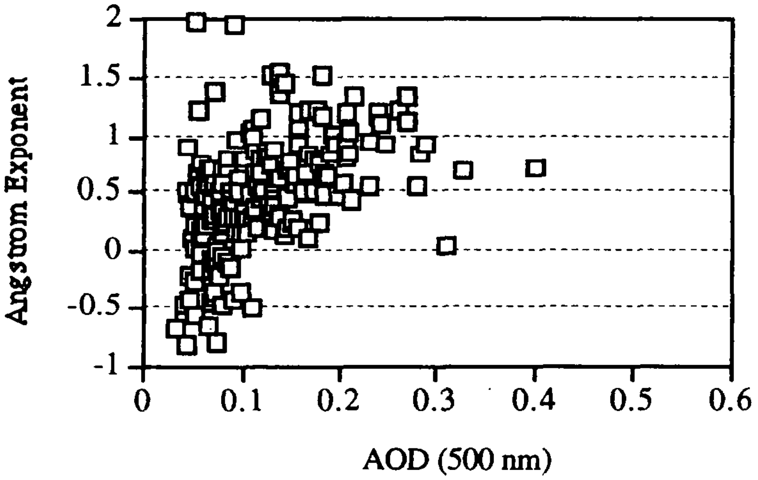

Figure 6b. Bermuda daily averaged AOD (500 nm) versus the Angstrom exponent.

Figure 6c

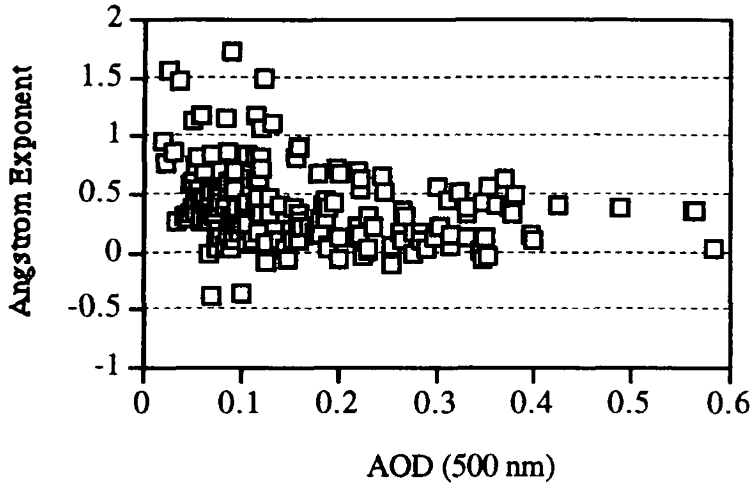

Figure 6c. Barbados daily averaged AOD (500 nm) versus the Angstrom exponent.

Figure 7a

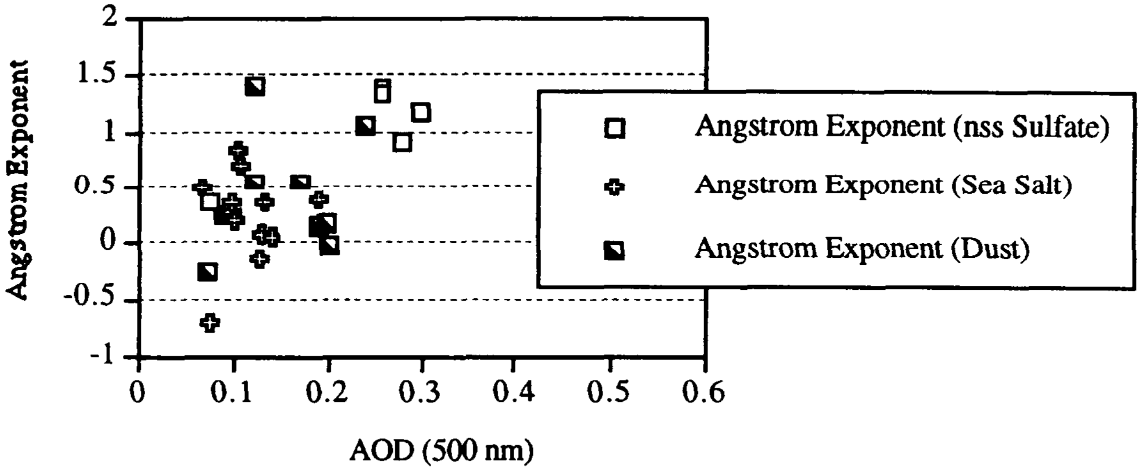

Figure 7a. Dominant aerosol correlation results: Miami daily averaged AOD (500 nm) versus the Angstrom exponent.

Figure 7b

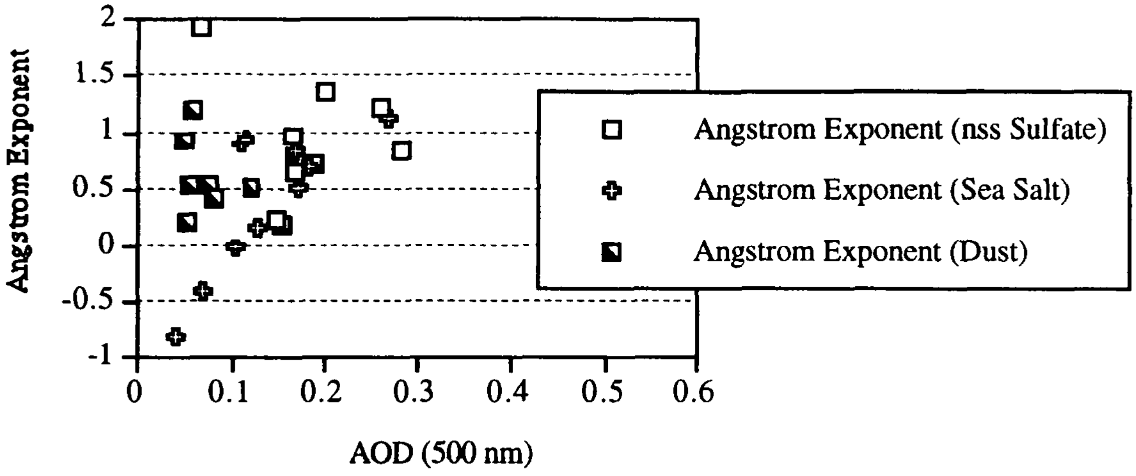

Figure 7b. Dominant aerosol correlation results: Bermuda daily averaged AOD (500 nm) versus the Angstrom exponent.

Figure 7c

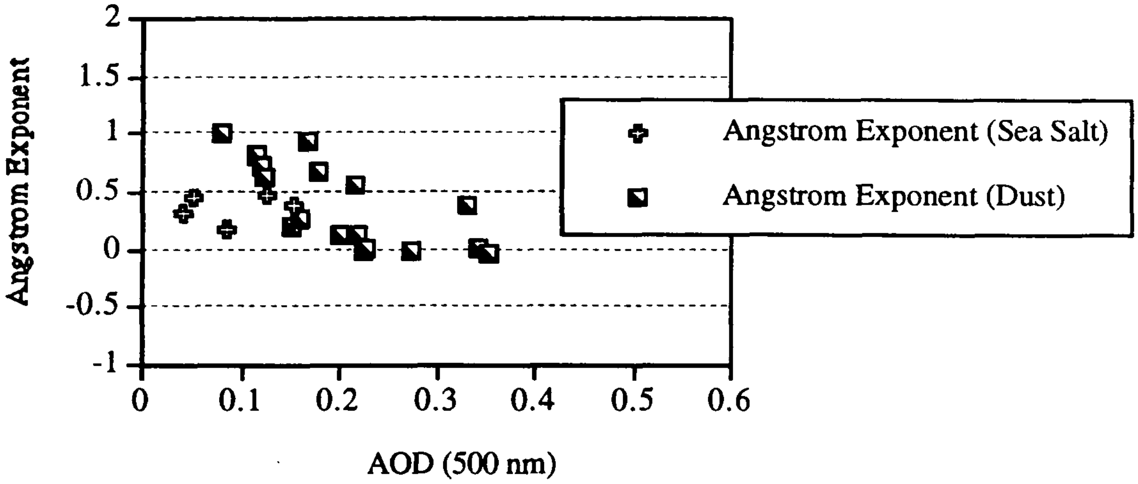

Figure 7c. Dominant aerosol correlation results: Barbados daily averaged AOD (500 nm) versus the Angstrom exponent.

Figure 8

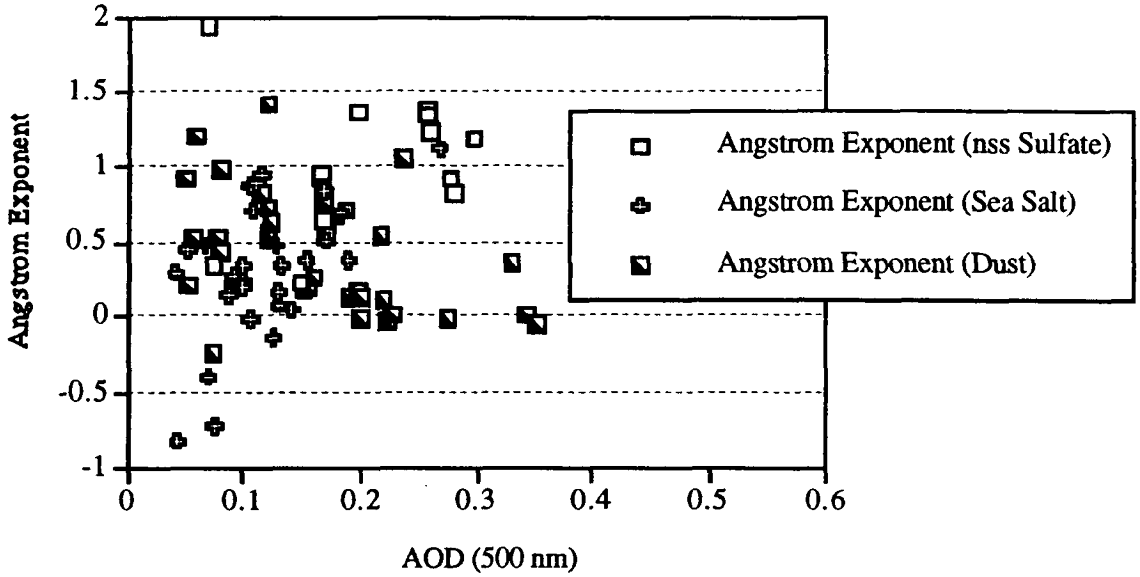

Figure 8. Dominant aerosol correlation results: Combined Miami, Bermuda, and Barbados daily averaged AOD (500 nm) versus the Angstrom exponent.

APPENDIX 5

Ground-based Lidar Measurements of Aerosols During ACE-2: Instrument Description, Results, and Comparisons with other Ground-based and Airborne Measurements

Ellsworth J. Welton [1], Kenneth J. Voss [1], Howard R. Gordon [1], Hal Maring [2],
Alexander Smirnov [3], Brent Holben [4], Beat Schmid [5], John M. Livingston [6],
Philip B. Russell [7], Philip A. Durkee [8], Paola Formenti [9], Meinrat O. Andreae [9]

1. University of Miami, Physics Department, Miami, Fl
2. University of Miami, Rosenstiel School of Marine and Atmospheric Science, Miami, Fl
3. Science Systems and Applications, Inc. - NASA / GSFC, Greenbelt, MD
4. NASA / GSFC, Greenbelt, MD
5. Bay Area Environmental Research Institute, San Francisco, CA
6. SRI International, Menlo Park, CA
7. NASA Ames Research Center, Moffett Field, CA
8. Naval Postgraduate School, Monterey, CA
9. Max Planck Institute for Chemistry, Biogeochemistry Dept., PO 3060, 55020 Mainz, Germany

Abstract:

A micro-pulse lidar system (MPL) was used to measure the vertical and horizontal distribution of aerosols during the Aerosol Characterization Experiment 2 (ACE-2) in June and July of 1997. The MPL measurements were made at the Izaña observatory (IZO), a weather station located on a mountain ridge (28°18' N, 16°30' W, 2367 m asl) near the center of the island of Tenerife, Canary Islands. The MPL was used to acquire aerosol backscatter, extinction, and optical depth profiles at IZO. System tests and calibration procedures are discussed, and analysis of aerosol optical profiles acquired during ACE-2 are presented. The optical characterization of upslope aerosol layers normally present at IZO (the background aerosol), and of a Saharan dust episode during the middle of ACE-2, are presented. Comparisons of the MPL data with data from other co-located instruments are also presented. The comparisons showed good during both the clean, upslope period and the dust episode. Finally, results show the possible perturbation of the bottom of the dust layer by upslope winds from the mountain.

1. Introduction

The Aerosol Characterization Experiment 2 (ACE-2) ran from June 16, 1997 to July 25, 1997. The purpose of ACE-2 was to study the radiative properties and physical characteristics of anthropogenic aerosols from Europe, and dust aerosols from Africa, as they are transported across the North Atlantic Ocean. An overview of ACE-2 operations and specific activities can be found in Raes et al. (this issue). One of the ACE-2 activities was the "clear sky column closure experiment" (CLEARCOLUMN) and was aimed at simultaneous measurements of aerosol properties using a variety of different platforms in order to assess the aerosol direct radiative forcing (Heintzenberg and Russell, this issue). The work presented in this paper was part of the CLEARCOLUMN effort during ACE-2.

This paper will focus on lidar measurements of the vertical and horizontal structure of aerosols surrounding the Izaña observatory (IZO) on Tenerife, Canary Islands during ACE-2. IZO is located on a mountain ridge (28°18' N, 16°30' W, 2367 m asl) near the center of the island and has often been used as a site for the study of various aerosol properties (Prospero et al., 1995; Raes et al., 1997; Smirnov et al., 1998). However, lidar measurements at IZO have not been made prior to this study. Thus, accurate knowledge of the spatial distribution of aerosols in the atmosphere surrounding IZO is needed in order to correctly apply the *in-situ* IZO data to studies of aerosols in the Eastern North Atlantic region. The lidar data are used to assess the vertical distribution and horizontal homogeneity of the aerosols in the atmosphere around IZO (10-30 km radius).

In addition to the lidar observations, *in-situ* aerosol mass concentration and extinction coefficient measurements were made at IZO. These *in-situ* measurements were used to aid in the calibration of the lidar system (as described in Section 3), and in comparisons with the near-IZO-range lidar data. Sunphotometer measurements were also made at IZO in order to supply spectral aerosol optical depth (AOD) measurements for

CLEARCOLUMN efforts and for use in a lidar inversion algorithm (Appendix). The algorithm uses the sunphotometer AOD along with the lidar data to produce profiles of the aerosol extinction coefficient and AOD, and the columnar backscatter-extinction ratio. The lidar derived aerosol optical data are used to show normal IZO site conditions, as well as conditions seen during Saharan dust passages. Finally, comparisons between the lidar data and data from other ACE-2 CLEARCOLUMN instruments are presented. In addition to daily comparisons with the other IZO instruments, joint measurements of the AOD on the afternoon of the July 17, 1997 dust episode were performed with the lidar, a sunphotometer on board an ACE-2 aircraft, and a radiometer installed on the nearby volcano of Tenerife (Teide). The comparisons demonstrate the success of the lidar calibration techniques and the lidar inversion algorithm, and show that lidar analysis can produce accurate profiles of ambient aerosol optical properties.

2. Instrumentation

2.1 Micro-pulse Lidar System (MPL)

The lidar used in this study is a micro-pulse lidar system (MPL) and is manufactured by Science & Engineering Services Inc., USA. Basic MPL design and background is described in Spinhirne (1993) and Spinhirne et al. (1995). The MPL system is revolutionary in that it uses rapidly pulsed low intensity laser light instead of slowly pulsed very high intensity laser light that has been used in previous lidar systems. The MPL system has μJ output energies and the beam is expanded to 20.32 cm in diameter which achieves ANSI eye-safe standards. A pulse repetition frequency (PRF) of 2500 Hz allows the system to average many low energy pulses in a short time to achieve a good signal-to-noise ratio. In practice, an averaging time of 1 minute is used for data collection but the stored signals can be averaged over longer periods if necessary during post-analysis. The MPL system also has a high vertical spatial resolution (75 m is used with the MPL system in this study). Finally, the MPL system is small compared to previous lidar systems and is therefore much more portable than its predecessors. The small size of the MPL system allows the operator to perform lidar measurements at any zenith angle by carefully tilting the instrument to the desired angle. It is therefore possible to perform horizontal and slant path measurements with the MPL as well as the normal vertical measurements. Care must be taken when operating the MPL during sunny days as direct sunlight entering the MPL can cause serious damage to the detector. The MPL must be tilted away from the sun or turned off and covered in such conditions.

The MPL is pictured schematically in Figure 1. The MPL transmitter-receiver (T-R) is located inside the climate housing and consists of a black 20.32 cm diameter cassegrain telescope with optics and electronics mounted directly below the telescope. The laser supply and scalar (data binning unit) are connected to the T-R, and along with the control computer, they must be located inside a separate climate controlled environment. The laser supply contains a diode pumped Nd:YLF laser with a fundamental pulse output wavelength of 1046 nm that is converted to 523 nm for lidar use after passage through a frequency doubling crystal. The MPL system used in this study was operated at the full laser power supply setting of 1 W. The pulse duration is 10 ns with a PRF of 2500 Hz and output energies ranging from 1 to 6 μJ depending upon system performance. Signals are received using the same telescope and are recorded with a Geiger mode avalanche photodiode.

The signals are stored as photons/sec (ph/sec). Since the receiver is a telescope focused at infinity, the T-R has difficulty accurately imaging near-range signals onto the detector. This problem is referred to as overlap error and causes the near-range signals (0 to approximately 2 km) to rapidly fall off in intensity the closer they are to the T-R. Since the majority of aerosols are contained in the first several kilometers of the atmosphere (or as at IZO, the first several kilometers in range from IZO), the overlap problem must be overcome. The procedures used in this study to correct for the MPL overlap are discussed in Section 3. The signals are binned in the scalar according to their time-of-flight from transmission to signal reception and correspond to steps of 75 m in range. Our MPL system has a pause of approximately 1 μs from activation of the detector to emission of the laser pulse. Thus, we disregard the first two signal bins and re-zero the range such that the third signal bin represents the signal return from 75 m.

A control computer is connected to the scalar and is used to control lidar operation, to visualize real-time lidar output, and to store the resulting lidar data. The data are stored in 1 hour binary files with each record containing a header followed by the signal in ph/sec at the successive 75 m increments up to a preset range (30 km). The maximum MPL range having usable data typically varies from approximately 30 km at night to about 10 km during reasonably clear daytime conditions. The lidar signals stored on the control computer contain background noise that is present from laser-detector crosstalk (afterpulse) and sunlight at 523 nm. Afterpulse noise must be corrected in post-analysis and the procedure is discussed in Section 3. Background sunlight noise is measured by the MPL in real time by measuring the detector signal after the maximum altitude signal (30 km) has arrived and before the next pulse is fired. This background signal is stored and used to correct the final signal by subtracting its value from each binned signal in post-analysis. The header information contains the time, output pulse energy, instrument temperatures, background sunlight energies, and information necessary for the operator to determine the altitude resolution used for each record in the data file.

2.2 Other IZO Instruments

In-situ aerosol measurements were made at IZO. Aerosol mass concentration measurements were made with a Rupprecht & Patashnick Model 1400a tapered element oscillating microbalance and extinction coefficients were obtained with a Radiance Research particle/soot absorption photometer, a TSI Model 3563 integrating nephelometer, and a

Radiance Research Model M903 integrating nephelometer. The IZO *in-situ* measurements were used for MPL calibrations and in comparisons with the MPL. A NASA AERONET cimel sunphotometer (Holben et al., 1998) was also operated at IZO for the duration of ACE-2. The cimel was used to acquire independent measurements of the AOD (Smirnov et al., 1998) for input to the lidar inversion algorithm (Appendix) and to perform aerosol measurements specific to AERONET and CLEARCOLUMN operations.

2.3 Airborne and Teide Instruments

The MPL was used to supply morning lidar signal profiles via fax to ACE-2 headquarters to assist in the pre-flight briefing for the Center for Interdisciplinary Remotely Piloted Aircraft Studies Pelican aircraft, which was one of the aircraft participating in ACE-2. AOD measurements were made on-board the Pelican with the NASA Ames Airborne Tracking 14-channel Sunphotometer, AATS-14, (Schmid et al., this issue). AOD measurements were also made on the island's volcano, Teide (28°16' N, 16°36' W, 3570 m asl), during ACE-2 using a multi-filter rotating shadowband radiometer (Formenti et al., 1998; Formenti et al., this issue). AOD data acquired with the AATS-14 and the shadowband are used in the comparison on July 17, 1997.

3. The Lidar Equation and MPL Calibrations

The basic lidar equation for returned signals is given by

$$\mathrm{S_L}(z) = \frac{CE}{(z - z_L)^2}[\beta_R(z) + \beta_A(z)]\exp\left[-2\int_{z_L}^{z}(\sigma_R(z') + \sigma_A(z'))dz'\right] \qquad (1)$$

where $\mathrm{S_L}(z)$ is the lidar signal at altitude z (m), C is the system constant (principally a function of the optics), E is the output energy in μJ, z_L is the lidar altitude (m), $\beta(z)$ and $\sigma(z)$ are the backscatter ($\mathrm{m^{-1}\ sr^{-1}}$) and extinction ($\mathrm{m^{-1}}$) coefficients respectively, the R subscript denotes a Rayleigh quantity (due to molecular scattering), and the A subscript denotes an aerosol quantity.

The backscatter coefficient is related to extinction by

$$\beta(z) = \mathrm{R}(z)\sigma(z) \ , \tag{2}$$

where R(z) is the backscatter-extinction ratio (BER) with units of sr^{-1}. The aerosol BER is considered to be constant for each profile in this study and thus is referred to as the columnar backscatter-extinction ratio, R_A. The BER is related to the aerosol phase function, $\mathrm{P_A}(\Theta)$ (normalized to 4π), and the single scattering albedo, ω_o, by $4\pi \bullet R_A = \omega_o \mathrm{P_A}(\pi)$.

It is useful to rewrite Eq. (1) by multiplying by the range squared, $(z-z_L)^2$, to remove the range dependent fall off in the signal returns and to use the BER to rewrite the equation in terms of only the backscatter coefficient,

$$\mathrm{S}_r(z) = CE[\beta_R(z) + \beta_A(z)]\exp\left[-\frac{2}{R_R}\int_{z_L}^{z}\beta_R(z')dz'\right]\exp\left[-\frac{2}{R_A}\int_{z_L}^{z}\beta_A(z')dz'\right] \tag{3}$$

where $\mathrm{S}_r(z)$ is referred to as the range-corrected lidar signal, R_R is the BER for Rayleigh scattering, and R_A is the BER for the aerosols. The lidar equation must be solved for the unknown aerosol quantities, $\beta_A(z)$, $\sigma_A(z)$, and R_A. The Rayleigh optical functions are constructed using data from Hansen and Travis (1974). The BER values used above are assumed to be constant with altitude. While R_R is constant, R_A may actually vary. Algorithms exist for lidar analysis using altitude dependent R_A values (Klett, 1985; Kovalev, 1993) but require additional assumptions or measurements of the vertical structure of the aerosol optical properties that were not possible for this work. The lidar inversion algorithm in this study uses an independent AOD measurement to iterate a basic lidar inversion (Fernald et al., 1984) to produce the $\beta_A(z)$ and $\sigma_A(z)$ profiles, and to calculate the value of R_A. The lidar inversion algorithm used in this study is discussed in the Appendix. Errors related to assuming constant BER values are also addressed in the Appendix.

The above discussion relates to vertical lidar measurements. Horizontal lidar measurements are used to assess the horizontal homogeneity of the atmosphere at a particular altitude. The backscatter and extinction coefficients for a horizontal lidar measurement during conditions of horizontal homogeneity are constant by definition. Therefore, a horizontal lidar signal simplifies Eq. (3) to

$$\mathrm{S}_H(x) = CE[\beta_R(z_L) + \beta_A(z_L)]\exp\left[-2(\sigma_R(z_L) + \sigma_A(z_L))x\right], \tag{4}$$

where $\mathrm{S}_H(x)$ is the horizontal lidar signal, x is the horizontal range in m, and the values of $\beta_i(z_L)$ and $\sigma_i(z_L)$ are constants with respect to x. Furthermore, taking the natural logarithm of both sides of Eq. (4) gives

$$\ln\left[\mathrm{S}_H(x)\right] = -2\left[\sigma_R(z_L) + \sigma_A(z_L)\right]x + \ln\left[CE(\beta_R(z_L) + \beta_A(z_L))\right]. \tag{5}$$

Thus, the slope of $\ln[\mathrm{S}_H(x)]$ versus the range x yields $-2\sigma_{\mathrm{total}}$ and the y-intercept is $\ln[\mathrm{CE}\beta_{\mathrm{total}}]$ for the horizontal homogeneous case. If the atmosphere is not horizontally homogeneous at the lidar altitude, then a horizontal lidar plot of $\ln[\mathrm{S}_r(z)]$ versus the range x will not produce a straight line.

MPL Calibration Procedure

Equation (3) is an ideal lidar signal. Actual lidar signals are effected by both afterpulse and overlap problems as mentioned in Section 2. Thus, an actual MPL range-corrected signal is given by

$$\begin{aligned}\mathrm{S}_r(z) = &\left\{C\,\mathrm{O}(z)E[\beta_R(z) + \beta_A(z)]\exp\left[-\frac{2}{R_R}\int_{z_L}^{z}\beta_R(z')dz'\right]\exp\left[-\frac{2}{R_A}\int_{z_L}^{z}\beta_A(z')dz'\right]\right\} \\ &+ \mathrm{A}(z)\end{aligned} \tag{6}$$

where O(z) and A(z) represent the overlap and afterpulse functions.

Calibration of the MPL system involves correcting for the afterpulse and overlap functions. Additionally, lidar calibration can also involve determination of the lidar system constant, *C*. However, the determination of the system constant was not a focus of this study since it is not needed to produce the optical coefficient profiles when the AOD is measured by an independent instrument (Appendix).

The calibration procedures applied to the MPL during ACE-2 differ from the normal MPL calibration techniques (Welton, 1998). The laser frequency doubling crystal in the MPL system burned midway through ACE-2. The cause of the burned crystal was attributed to a poor ground connection between the laser temperature controller on the laser supply and the laser itself, located inside the T-R. Data continued to be taken with the MPL system because the problem was not noticed until the end of the experiment.

The data acquired after the crystal burn had noticeable effects caused by signal loss and diffraction from the burn pattern. Signal loss resulted from light scattered off axis, by the hole, that was lost before reaching the T-R. Diffraction effects were believed to be the cause of distortions in the outgoing laser pulses. These diffraction effects caused distortion of the MPL overlap characteristics and altered the afterpulse signal. These problems became worse as the experiment continued. Thus it was not possible to use the pre-experiment calibrations or post-calibrations to correct the entire data set taken during the experiment. Therefore, a new lidar calibration procedure was developed to handle the MPL data during ACE-2. The procedure is based on normalization of the MPL signals to those signals from a molecular (Rayleigh) only atmosphere and is described below.

Due to its unique location, IZO is in the free troposphere at night (Raes et al., 1997). The MPL performed vertical profile measurements during normal ACE-2 nighttime lidar operations. Several nights were very clean and the lidar returns were assumed to represent pure Rayleigh scattering with the exception of the afterpulse and overlap effects. This assumption was based on normal nighttime conditions and inspection of both aerosol mass concentration and aerosol extinction coefficient measurements made at the observatory during the night. The early mornings (00:00 GMT to 03:00 GMT) of June 29 and July 15, 1997 were chosen as having clean (negligible aerosol concentrations) based on the low aerosol concentrations and extinction coefficients shown in Figures 2a and 2b.

At 00:00, 01:00, 02:00, and 03:00 GMT, a 15 minute average Rayleigh lidar signal, $S_R(z)$, was calculated using Eq. (3) with $\beta_A(z) = 0$, E obtained from the actual time corresponding measured lidar signal, and with C set equal to 100,

$$S_R(z) = 100E\beta_R(z)\exp\left[-\frac{2}{R_R}\int_{z_L}^{z}\beta_R(z')dz'\right] . \qquad (7)$$

The actual measured lidar signals are expressed using the following equation,

$$S_L(z) = CE\,O(z)\beta_R(z)\exp\left[-\frac{2}{R_R}\int_{z_L}^{z}\beta_R(z')dz'\right] + A(z) , \qquad (8)$$

where $\beta_A(z)$ is still assumed to be zero. Eq. (8) can be rewritten in terms of the Rayleigh-only signal as

$$S_L(z) = O(z)\,S_R(z) + A(z) . \qquad (9)$$

The term $S_R(z)$ is calculated and the term $S_L(z)$ is measured with the MPL system, thus the only unknowns in Eq. (9) are O(z) and A(z). A linear regression was performed using Eq. (9), the calculated Rayleigh signal, and the measured lidar signal for each altitude bin in each period (4 each night) from the chosen nights. The y intercepts where used to construct the afterpulse function and the slope was used to determine the overlap function. The resulting overlap and afterpulse functions are shown in Figures 3a and 3b.

The overlap function for June 29 approaches an asymptote of almost 10, instead of the usual value of 1, as the range increases beyond 2 km. This is due to setting C equal to 100 for the calibration procedure. The actual value of C for the June 29 period was most likely much higher than 100. This is also the reason for the negative afterpulse values calculated for June 29. The overlap and afterpulse functions for June 29 do not represent the physical overlap and afterpulse values for this period due to the arbitrary choice of C. However, the overlap and afterpulse functions still produce the correct lidar calibration. Also, the MPL crystal problems increased in magnitude as the experiment progressed, and the value of C decreased significantly. The value of C was very close to 100 by July 15, as evidenced by the overlap asymptotic limit of approximately 1 for this day. Also, the afterpulse values for July 15 are similar to those obtained using the MPL with no crystal problem (Welton, 1998).

The overlap and afterpulse functions were used to correct MPL signals only during the days immediately after the calibration night. As an example of applying the calibration functions to the MPL data, Figure 4 shows the original lidar signal measured at 00:00 GMT on June 30, the calculated Rayleigh signal, and the corresponding overlap and afterpulse corrected signal. The signal now resembles a free troposphere Rayleigh-only lidar signal and demonstrates the success of the calibration procedure.

4. Analysis of ACE-2 MPL Data

The MPL was operated on a daily schedule that involved vertical, horizontal, and slant path (T-R tilted to 60° zenith angle) measurements at specific times of the day. Vertical measurements were typically performed from 00:00 GMT to 10:30 GMT and again from 16:30 GMT to 23:59 GMT each day. Horizontal measurements were usually performed from 10:30 GMT to 11:00 GMT and from 16:00 GMT to 16:30 GMT, and slant path measurements were made each day from 11:00 GMT to 16:00 GMT. Slant path rather than vertical orientation was necessary during mid-day to prevent direct sunlight from entering the T-R and damaging the MPL detector and optics. The schedule was occasionally altered to accommodate Pelican overflights and special ACE-2 directed activities. For this study, only vertical and selected horizontal measurements are discussed.

MPL installation and testing was performed during the first weeks and normal operation began on June 28. The instrument problems with the MPL system became substantial after July 20, 1997 and the resulting data from the correction procedure were not considered reliable. Thus, only MPL data from June 28 to July 20 were analyzed for this study. The MPL signals were calibrated using the procedure discussed in Section 3. The signals were then divided by the lidar constant C (set equal to 100) and the corresponding output energy E. The resulting profile is referred to as an attenuated backscatter signal (ABS, units of m^{-1} sr^{-1}) because it is a profile of the total backscatter coefficient and is attenuated by the exponential transmission function. The ABS profiles for all the vertical measurements made from June 28 to July 20 showed that no aerosols were present above an altitude of approximately 6 km during ACE-2. Also, most days during ACE-2 produced similar ABS profiles and were identified as the normal site condition influenced by upslope aerosols. The periods, July 7 to July 9, and July 16 to July 18, showed much higher ABS values relative to the normal site profiles. These two periods correspond to the first and second Saharan dust passages observed during ACE-2. This study will focus on the normal upslope aerosol conditions at IZO during June 29 to July 1, and the Saharan dust episode from July 16 to July 18.

4.1 Analysis of Upslope Aerosols

During the day, local heating near IZO (along the mountain ridge) creates an upslope wind. This local wind carries aerosols from within the marine boundary layer (MBL) below IZO, to the level of IZO and beyond. The upslope aerosols appear in the early morning as the sun rises and subside by the late afternoon as the sun sets and the air temperature stabilizes. The presence of upslope aerosols during the daytime is characteristic of normal conditions at the IZO site (Raes et al., 1997), therefore, it is necessary to understand the upslope aerosol's spatial distribution and optical profile before analysis of the Saharan dust layers can be attempted.

Time series ABS profiles are shown for June 29 to July 1 in Figure 5. Also, ABS profiles from early morning to late afternoon on June 29 are shown in Figures 6a and 6b. The ABS profile at 06:15 GMT, approximately 45 minutes before sunrise (~ 07:00 GMT) is representative of a Rayleigh-only profile, no aerosol layers are present. However, the profile at 07:15 GMT shows a weak aerosol layer extending to under 6 km in altitude. The profiles at 10:15 GMT and 17:15 GMT also show aerosol layers extending to under 6 km in altitude but with much higher ABS values just over IZO. These mid-day ABS profiles are significantly less than the earlier ABS profiles at higher altitudes due to the attenuation of the upslope layer. The ABS profile at 19:15 GMT shows the aerosol layer subsiding, with ABS values similar to the 07:15 GMT profile, and lower than during mid-day. Finally, the ABS profile at 22:15 GMT shows no indication of aerosol layers, and instead resembles the Rayleigh-only ABS profile at 06:15 GMT. The ABS profiles in Figures 6a and 6b clearly show the presence of the upslope aerosols and this pattern is typical for normal upslope conditions at IZO during ACE-2.

Upslope Aerosol Extinction Coefficient and Optical Depth Profiles

The AOD measured with the IZO cimel was used to calculate the aerosol extinction coefficient (AEC), the columnar backscatter-extinction ratio (BER), and AOD profiles for the upslope aerosol layers on June 29, 1997 using the inversion algorithm discussed in the Appendix. The profiles shown for June 29 are representative of normal upslope aerosol conditions during ACE-2. The lidar AEC profiles are shown in Figure 7a and the AOD profiles are shown in Figure 7b. The daytime average AEC measured at IZO using the nephelometer is also shown in Figure 7a, and the AOD measured by the Teide shadowband is displayed in Figure 7b. The Rayleigh extinction coefficient profile is shown in Figure 7a for comparison.

Significant AEC values (greater than the Rayleigh extinction coefficient) extend from just under 3 km to approximately 3.5 km in altitude for the 08:15, 17:15, and 18:15

GMT profiles. The bottom of the upslope layer is lower during the late morning profile at 10:15 GMT and at this time the layer extends from approximately 2.5 km to 3.5 km in altitude. The upslope layers at IZO typically begin forming at approximately 07:00 to 08:00 GMT and begin dissipating just prior to 18:00 GMT. The formation of the upslope aerosols corresponds with a gradual lowering of the bottom of the layer through to the late morning, and the dissipation of the upslope aerosols corresponds with a gradual increase in the altitude of the bottom of the layer.

The peak upslope aerosol AEC values are approximately 1.5e-5 m^{-1}. These are not large compared with boundary layer values (Schmid et al., this issue) but are higher than free-troposphere values (Rayleigh values). The AEC values peak at approximately 3 km in altitude, but are much lower near IZO throughout the day. In order to check that this was not due to a poor calibration of the MPL, the nearest range lidar AEC value (2.442 km) was compared to the daytime (07:00 to 19:00 GMT) AEC measured at IZO using a nephelometer. The average lidar AEC value at 2.442 km for the 10:15 and 17:15 GMT profiles is 4.4e-6 m^{-1}, which agrees well with the IZO nephelometer AEC value of ~5e-6 m^{-1}. However, the 08:15 and 18:15 GMT lidar AEC values (at 2.442 km) are much lower than the IZO value. This is most likely due to the rapidly changing aerosol conditions during the formation and dissipation of the upslope layer. The changing aerosol conditions (thus, varying AOD values from the cimel) and overall low AEC values, results in poorer inversion results.

The AOD measured with the Teide shadowband is compared to the lidar AOD value at 3.57 km in Figure 7b. The low AOD values measured by all instruments demonstrate the absence of Saharan dust during this period. The lidar AOD value at 3.57 km is approximately half of the Teide AOD value. The AOD values from both instruments are small and the difference between the two are within the bounds of measurement error. The difference in AOD may also be due to the presence of upslope aerosols specific to Teide which are not present one kilometer over IZO.

Upslope Aerosol Backscatter-Extinction Ratios

The AEC and AOD profiles shown in Figures 7a and 7b each correspond to a calculated columnar BER value from the lidar inversion. The BER values for the 08:15, 10:15, 17:15, and 18:15 GMT profiles on June 29 are 0.018, 0.038, 0.031, and 0.017 sr^{-1} respectively. Low BER values (~0.020) during the early morning and late afternoon, and higher BER values (~0.035) during mid-day were characteristic of upslope aerosol conditions at IZO during ACE-2. The low BER value of ~0.020 occurs during the formation and dissipation of the upslope aerosol layer, while the higher BER value of ~0.035 occurs during the stable mid-day period of the upslope layer.

The lidar $\omega_o P_A(\pi)$ value for the early morning and late afternoon periods averages ~0.25 sr^{-1}, and averages ~0.44 sr^{-1} for the mid-day period. Phase functions derived from the cimel during ACE-2 were generated using Mie theory (O. Dubovik, personal communication) and were used in conjunction with the lidar $\omega_o P_A(\pi)$ values in order to assess the impact of particle non-sphericity. The lidar BER values, and hence the lidar $\omega_o P_A(\pi)$ values, calculated using the lidar inversion alogrithm in the Appendix are not dependent upon Mie theory and are direct calculations. Mishchenko et al. (1997) have shown that there are unique differences in the aerosol phase function for the ratio of non-spherical to spherical measurements. They have shown that, in general, there is little difference at forward scattering angles (0° to 10°), but that when particle non-sphericity is taken into account increased side-scattering (near 120°) and decreased backscatter (at 180°) occurs relative to spherical particle calculations. The data shown in Plate 5 of Mishchenko et al. (1997) depicts the behavior of both Mie and non-spherical phase functions for different size parameters, x_{eff}, using a refractive index of $1.53 + 0.008i$.

The cimel (henceforth referred to as Mie) phase functions at 0° and 180° and the lidar $\omega_0 P_A(\pi)$ values (no Mie dependence) were used to determine the degree of particle non-sphericity and a value of x_{eff} by comparison with the Plate 5 Mishchenko et al. (1997) data. The Mie phase functions at 0° are just over 30 sr^{-1} in the early morning (07:50 GMT) and from 70 to 90 sr^{-1} at mid-day (measurements at 11:00 and 17:30 GMT). The Mie phase functions at 180° are approximately 0.3 sr^{-1} in the early morning, and average approximately 0.4 sr^{-1} during mid-day. The forward and backward Mie phase function values given above do not exactly match the behavior of Mie functions in Plate 5 of Mishchenko et al. (1997) most likely due to differences in the refractive indices used to generate them. However, the ratio of the lidar to Mie phase function values still yields useful information. Comparing the forward Mie phase function values from the cimel with those given in Plate 5 of Mishchenko et al. (1997) give x_{eff} ranges from 6 to 10, which correspond to r_{eff} values from 0.5 to 0.8 microns using the lidar wavelength. The Mie phase functions at 180° are not much different from the lidar $\omega_0 P_A(\pi)$ values for morning and mid-day. The lidar $P_A(\pi)$ and Mie $P_A(\pi)$ values would then agree very well assuming ω_0 is not significantly less than 1, indicating that the particles are fairly spherical in shape.

Upslope Horizontal Lidar Signal Results

Analysis of horizontally aimed lidar measurements (approximately due East) during upslope conditions was performed. The natural logarithm of the horizontal ABS at 10:45 GMT on June 29 is shown in Figure 8 along with a calculated Rayleigh horizontal plot. The presence of the upslope aerosols along the side of the mountain is shown by the elevated and non-linear ABS values out to approximately 1.5 km from the side of the mountain. The plot becomes linear after 1.5 km, thus, the atmosphere does appear to be horizontally homogeneous from 1.5 km out to 6 km (the maximum daytime range of the

MPL during most of ACE-2). However, near the side of the mountain, and near IZO, horizontal homogeneity does not exist due to the presence of the upslope aerosols.

4.2 Analysis of Saharan Dust Episode

Three Saharan dust episodes occurred during ACE-2. Each episode was characterized by the presence of dust layers at and above the IZO site. The first dust episode started at mid-day on July 7 and continued until the afternoon of July 9. The second dust episode started late in the evening on July 16 and continued until the morning of July 18. The last dust episode started on the morning of July 25 and continued into July 26, past the end of ACE-2.

During much of the first dust episode, the MPL was orientated in the slant path position. During this episode, inspection of the dust layer lidar returns and IZO aerosol concentration and nephelometer data showed that very little of the dust was at the IZO altitude. The decision was made to orient the MPL on a slant path in order to attempt to measure dust data lower than the MPL's lowest vertical measurement range (75 m). As a result, there is little vertical MPL data during the first dust episode. Also, the last dust episode occurred after the period when the MPL data could be accurately corrected. Therefore, no usable MPL data exists for the last dust episode. The results presented below for Saharan dust layers are derived from analysis performed on data acquired during the second dust episode, from July 16 to July 18.

It is important to note that sulfates and other aerosol species have often been correlated with dust episodes at IZO and elsewhere over the North Atlantic Ocean (Welton et al., unpublished data; Maring, personal communication). Therefore, the results presented in this section for dust conditions at IZO are likely to include some effects from aerosols other than dust, and may in fact underestimate the effects of the dust aerosols alone.

A time series of ABS profiles from July 16 through July 18 is shown in Figure 9. The calibration of the MPL was more difficult for this period, relative to June 29, because the MPL crystal problems were much worse than in late June. The final July 16 to July 18 calibrated lidar data contains more noise than the June 29 to July 1 data. The straight lines running across the figure are due to noise in the calibrations and not aerosol effects. The problem is only significant during mid-day at altitudes over 6 km (which exceeds the maximum aerosol altitude observed during ACE-2 using the MPL). This was due to a low signal-noise ratio caused by background sunlight and very high dust concentrations, corresponding to high signal attenuation, during mid-day.

The temporal extent of the dust layer is clearly evident. The dust layer appeared at approximately 22:00 GMT on July 16 at an altitude of approximately 3.5 km. The layer dropped in altitude by the morning of July 17 with the majority of the dust at altitudes from about 2.5 km to about 4 km until the late afternoon. The layer thickness narrowed in altitude considerably after 18:00 GMT on July 17. Most of the dust remained at altitudes from about 2.75 km to 3.5 km for the duration of the episode, which ended the morning of July 18.

Dust Aerosol Extinction Coefficient and Optical Depth Profiles

The AOD measured with the IZO cimel was used to calculate the AEC, the columnar BER, and the AOD profiles for the dust layers on July 17, 1997 using the inversion algorithm discussed in the Appendix. The lidar AEC profiles calculated throughout the day (08:15, 10:15, 17:15, and 18:45 GMT) on July 17 are shown in Figure 10 along with the Rayleigh extinction coefficient profile for comparison. The AEC values for July 17 are orders of magnitude higher than the upslope values on June 29 and thus the presence of the dust is obvious. The peak AEC values were between 1.5e-4 and 2e-4 m^{-1} and were located just above 3 km in altitude. Significant AEC values (greater than the Rayleigh extinction coefficient) were present from the IZO altitude to just under 5 km.

The inversion results for 10:15 GMT and 17:15 GMT are slightly effected by the calibration noise problem discussed above. The signals are too noisy to start the inversion at 5 km or higher for these two times. Thus, the inversions were started at 4.8 and 4.5 km for the two profiles respectively. The end result is a profile which has fairly accurate AEC and AOD values due to the high concentrations of aerosol, but may have less accurate BER values. The results from the 08:15 and 18:45 GMT profiles were not effected by this problem.

Figure 11a shows the July 17 lidar AEC profiles at 10:15 and 18:45 GMT. Figure 11a also shows the average AEC measured by the IZO nephelometer at both mid-day (Daytime) and after 18:00 GMT. The lidar AEC values at 2.442 km agree well with the IZO nephelometer AEC values. Figure 11b shows the lidar AOD profile at 18:45 GMT, the AATS-14 (onboard the Pelican aircraft) AOD profile from 18:30 to 18:45 GMT, and the AOD measured by the Teide shadowband and the IZO cimel for this time period. The AATS-14 AOD values immediately above the IZO altitude, average 0.218 ± 0.05 AOD units. This portion of the Pelican flight corresponds to horizontal flight tracks across the mountain ridge, approximately 50 meters over IZO. The spread in AOD (± 0.05) for these tracks is evidence of slight changes in the horizontal homogeneity of the dust layer overhead. The AOD values from all the instruments agree within approximately 0.02 AOD units for most of the profile and they agree better than the ± 0.05 AOD spread from horizontal inhomogeneity for the entire profile. The excellent agreement between the lidar 18:45 GMT data and the data from the other instruments for this time shows that the MPL calibrations and inversion algorithm worked successfully and that the BER calculated for this profile was accurate for this dust episode.

Dust Aerosol Backscatter-Extinction Ratios

The calculated lidar BER values for the 08:15, 10:15, 17:15, and 18:45 GMT profiles were 0.026, 0.048, 0.073, and 0.027 sr^{-1} respectively. The same diurnal increase in the BER, as was present for the upslope aerosols, may exist during the dust episode because slightly higher BER values (average ~0.06 sr^{-1}) during mid-day relative to BER values for morning and late afternoon (average ~0.025 sr^{-1}) were calculated on July 17. However, the mid-day BER values may be inaccurate due to the calibration noise problem. Elevated BER values during mid-day could also be caused by the presence of a small amount of small spherical upslope aerosols. However, analysis of this possible effect is beyond the scope of this paper.

Thus, attention was focused on the morning and late afternoon lidar profiles (08:15 and 18:45 GMT respectively) because they were not influenced by significant noise problems. The lidar $\omega_0 P_A(\pi)$ value for these periods is approximately 0.3 sr^{-1}. Mie phase functions were calculated (O. Dubovik, personal communication) using the cimel data on July 17. The Mie phase function values at 0° were near 200 sr^{-1} at 08:00 GMT and near 300 sr^{-1} at 18:30 GMT. The Mie phase function values at 180° for 08:00 and 18:45 GMT were nearly identical and averaged approximately 0.6 sr^{-1}. The ratio of the lidar $P_A(\pi)$ value with the Mie $P_A(\pi)$ value from the cimel is ~0.5 assuming $\omega_0 = 1$, and the ratio is ~0.625 assuming $\omega_0 = 0.8$. The ratio of lidar to Mie $P_A(\pi)$ values, calculated using ranges of ω_0 similar to those determined during this dust episode (Formenti et al., this issue; Schmid et al., this issue), agree well with the results presented in Mishchenko et al. (1997) for non-spherical particles. Therefore, the aerosols present during this dust episode were non-spherical. Also, comparison of the measured cimel and lidar phase function values with the phase functions in Plate 5 of Mishchenko et al. (1997) gives x_{eff} ranges from 16 to 20, corresponding to r_{eff} ranges from 1.3 to 1.7 microns (assuming the index of refraction $1.53+0.008i$).

Dust Horizontal Lidar Signal Results

Horizontal profiles (lidar aimed approximately due East) of the natural logarithm of the ABS on July 17 at 11:15 and 18:50 GMT are shown in Figure 12, along with a calculated Rayleigh profile for comparison. Both measured lidar profiles are non-linear within 2 km of IZO, indicating that horizontal homogeneity did not exist near the mountain ridge. The 11:15 GMT profile shows an increasing and non-linear plot out to about 1.5 km in range, followed by a fairly linear (but noisy) plot from 1.5 to 4 km. The 18:50 GMT profile also shows a non-linear plot out to about 2.5 km, followed by a linear plot from 2.5 to 4 km. Therefore, the atmosphere does appear to be horizontally homogeneous from approximately 2 km to 4 km (the maximum horizontal range with dust present) away from the mountain ridge during this dust episode.

Both horizontal profiles show that the aerosols are not horizontally homogeneous close to the side of the ridge (out to about 2 km). However, the sharply increasing plot within the first kilometer of range for the 11:15 GMT profile shows that a large amount of aerosol was present within 1 km from the ridge relative to the situation at 18:50 GMT. The increase in aerosol within 1 km of the ridge during daytime (11:15 GMT) corresponds to the upslope period. The 18:50 GMT profile shows that less aerosol was located close to the mountain side (within 1 km), and corresponds to the period after the upslope has subsided (~18:00 GMT). The upslope wind motion may have changed the dust layer near the mountain and indicates the importance of considering upslope effects on the horizontal homogeneity of the region around IZO.

5. Conclusions

The operation of the MPL system during ACE-2 has shown that this new lidar technology can be used successfully in the field. ACE-2 closure comparisons between the MPL system and other independently operated instruments have shown that the MPL calibration procedures and inversion algorithm succeed in producing accurate optical profiles throughout the entire range of the profile. This is significant because it shows that the overlap and afterpulse problems can be overcome, even when the MPL has suffered an instrument problem.

The results of lidar analysis during ACE-2 have shown several interesting characteristics of the upslope aerosols and the Saharan dust episode during the middle of the experiment. The upslope aerosols were seen to form a layer several hundred meters above and to the sides of IZO during the day, and to subside by nightfall. The peak AEC values obtained in these upslope aerosol layers were low compared to MBL values, but were approximately 25% greater than Rayleigh values. The dust layer on July 17 was seen to reside mostly above and to the sides of IZO, possibly held off by the motion of upslope winds despite findings that show upslope winds have been known to be weaker during dust episodes (Raes et al., 1997). The possible perturbation of the dust layer by the upslope effect is significant due to the fact that the IZO site is used during summer months to study Saharan dust layers. Peak AEC values obtained during the dust episode were an order of magnitude higher than Rayleigh values. Finally, the dust layer altitude ranges observed during ACE-2 (from just over 2 km to under 5 km) correspond well with other investigations of the vertical structure of the Saharan air layer (SAL) over the North Atlantic Ocean (Carlson and Prospero, 1972; Karyampudi and Carlson, 1988).

Results of this study also show that upslope aerosols (r_{eff} from 0.5 to 0.8 microns) are smaller relative to aerosols during the dust episode (r_{eff} from 1.3 to 1.7 microns). The differences in r_{eff} values between upslope and dust conditions agree well Angstrom exponents measured with the IZO cimel during ACE-2 (Smirnov et al., 1998). The Angstrom exponent during upslope conditions on June 29 was approximately 1.0, indicating may small particles, and the Angstrom exponent during the afternoon of the July 17 dust episode averaged 0.16, indicating a greater portion of larger particles. Another important result was the determination of an accurate BER value (0.025 sr^{-1}) for the dust episode on July 17. Knowledge of an accurate BER during dust episodes will aid in the analysis of future lidar measurements in regions influenced by dust aerosols. Finally, the degree of non-sphericity of the upslope aerosols was found to be small, but the degree of non-sphericity of the aerosols during the dust episode was large and found to be in agreement with previous theoretical studies of dust-like aerosols.

Several areas requiring further study have also been identified. Using the initial results from work presented in this study and others in this issue, more in-depth comparisons and analysis of data from the different measurement platforms will be addressed in future work. In addition to more accurate results of the type discussed in this study, attention will be given to correct determination of the altitude dependence of the index of refraction and the single scattering albedo. This will in turn produce better lidar inversions and help to determine the correct BER for both the upslope and dust aerosols. Lastly, further studies of the horizontal homogeneity of the region surrounding IZO will be attempted.

Appendix: The Lidar Inversion Algorithm

The lidar inversion algorithm used for this study is presented in this section. Also, errors inherent to the algorithm are discussed. The primary error is due to the assumption of a constant BER value, R_A.

The Solution to the Lidar Equation

The basic $\beta_A(z)$ solution to lidar data taken according to Eq. (3) is referred to as the backward Fernald two-component solution (Fernald et al., 1972) as it uses the value of the backscattering coefficient at some maximum altitude, z_m, as a boundary value and then successive values of $\beta_A(z)$ are calculated as the altitude is decreased toward the lidar altitude, z_L. The solution is given below in a format for algorithm development (Fernald, 1984),

$$\beta_A(x-1) = \frac{S_r(x-1)\Psi(x-1,x)}{\dfrac{S_r(x)}{\beta_A(x)+\beta_R(x)} + \dfrac{1}{R_A}\left[S_r(x) + S_r(x-1)\Psi(x-1,x)\right]\Delta z} - \beta_R(x-1), \quad \text{(A.1)}$$

where

$$\Psi(x-1,x) = \exp\left[\left(\frac{1}{R_A} - \frac{1}{R_R}\right)\left(\beta_R(x-1) + \beta_R(x)\right)\Delta z\right] \;,$$

and x is the altitude bin one step above x-1, and Δz is the lidar range interval (75 m). In order to obtain the extinction coefficient profile, each value of the backscattering coefficient need only be divided by R_A.

The basic lidar algorithm that uses Eq. (A.1) to solve for the aerosol profiles must assume that R_A and the backscattering coefficient at some maximum altitude, $\beta_A(z_m)$, are known. R_A is not usually known, but the latter constraint is usually valid as aerosols are normally confined to the marine boundary layer (MBL), or at least at low altitudes above the lidar (such as over IZO), therefore, z_m can be chosen at an altitude where $\beta_A(z_m) = 0$. An algorithm was developed for this study that uses an independently measured AOD, τ_A, as input and produces a σ_A profile that integrates to the measured AOD and will also calculate the value of R_A.

The Lidar Inversion Algorithm

This algorithm is based on procedures described in Fernald et al. (1972) and Marenco et al. (1997). The alogrithm produces extinction coefficient and AOD profiles, and also calculates the BER. The algorithm is described below and presented schematically in Figure 13.

The first step in the algorithm requires determination of β_A at some maximum altitude, z_m, and is done by inspection of the calibrated signals. Inspection of the signals during ACE-2 showed that there was a maximum altitude, above which, no aerosol appeared to be present ($\beta_A \sim 0$). The inversion algorithm value of z_m was chosen to lie just above this altitude, with β_A set equal to 0.

The second step in the algorithm is the calculation of β_A one altitude step, 75 m, below z_m. This is done by solving Eq. (A.1) with $\beta_A(x=z_m) = 0$, and the Rayleigh profile quantities; $\beta_R(z)$, $\sigma_R(z)$, and R_R, from Hansen and Travis (1974). In order to solve Eq. (A.1), R_A is required. For this step in the algorithm, R_A is set equal to 1 and $\beta_A(x-1)$ is calculated. This process is repeated downward through the atmosphere, with $R_A = 1$ and $\beta_A(x+1)$ obtained from the previous step, until the value of β_A is calculated at the lowest altitude bin (75 m above the MPL system altitude).

The next step in the algorithm is to improve the estimate of R_A (determination of $R_{A\,new}$). The new value for R_A is determined using the backscattering coefficient profile calculated in the previous step (with $R_A = 1$) and the independently measured AOD, τ_A. $R_{A\,new}$ is calculated using the following equation,

$$R_{A\,new} = \frac{\int_{z_L}^{z_m} \beta_A(z')dz'}{\tau_A} \tag{A.2}$$

with τ_A from the independent measurement. The backscattering coefficient profile is now recalculated, using $\beta_A(x=z_m) = 0$, but with $R_A = R_{A\,new}$. This step is continued until successive values of R_A and $R_{A\,new}$ differ negligibly (percent difference between R_A and $R_{A\,new}$ less than 0.5). The final backscattering coefficient profile and R_A are then used to calculate the extinction coefficient profile, $\sigma_A(z)$. The extinction coefficient profile is then numerically integrated from z_L to z_m, and then subtracted from τ_A at each altitude step, to produce an AOD profile, $\tau_A(z)$. Thus the final data products from the algorithm are the extinction coefficient and AOD profiles and R_A.

Errors in the Results from the Lidar Inversion Algorithm

This algorithm was tested with artificial lidar data to study the effects of errors caused by the algorithm and the assumption of a constant R_A (Welton, 1998). Both a single and a two aerosol species atmosphere were tested. The results show that in a single aerosol species atmosphere (with constant R_A) the algorithm accurately calculates the $\beta_A(z)$ profile and the correct R_A (and thus accurate $\sigma_A(z)$ and AOD profiles) even if the concentration of the aerosols varies vertically and the aerosols are separated into different layers. For cases with two aerosol species with different R_A values and different backscattering coefficient profiles, the results show that the algorithm was found to calculate an R_A value that was an accurate average of the two different true R_A values whether the species were in one continuous layer (but not mixed together) or separated into two distinct layers. For real situations, different aerosol species are often mixed together and it is expected that the final BER calculated will be dependent more on the relative amounts of each aerosol and will not produce a direct average of the different individual BER values. However, the algorithm will produce an accurate columnar value of the R_A in real situations. This is an important result since other ground-based instruments that also measure R_A related quantities, such as the aerosol phase function, also produce columnar values because they measure the entire atmospheric column.

Errors were present in the resulting $\beta_A(z)$ profiles when the constant R_A inversion algorithm was applied to an inhomogeneous R_A atmosphere. The initial $\beta_A(z)$ profile values near z_m are correct but successive values of β_A deviate from the correct value, this and the calculation of an average R_A then effect the calculation of the $\sigma_A(z)$ profile. The algorithm forces the final $\sigma_A(z)$ profile to integrate to the correct τ_A value. The value, β_A/R_A will be iterated continually, until the correct τ_A value is reached. If the R_A value used is incorrect, then the resulting β_A profile will have errors.

These types of R_A related errors have been studied by other researchers in depth (Klett, 1985; Sasano et al., 1985; Kovalev, 1993; Kovalev and Moosmuller, 1994). In order to attempt to overcome errors associated with the choice of a constant R_A, these researchers have constructed algorithms using range dependent R_A values. However, for these algorithms an R_A profile, from model or data, must be used. The choice was made to use a constant R_A algorithm for this study since neither data, nor models of R_A, were available during the lidar campaigns.

Acknowledgments

This research is a contribution to the International Global Atmospheric Chemistry (IGAC) core project of the International Geosphere-Biosphere Programme (IGBP) and is part of the IGAC Aerosol Characterization Experiments (ACE). The authors extend great appreciation to E. Cuevas, R. Juega Buide, and the rest of the Izaña observatory staff for their support during ACE-2. Thanks is also given to O. Dubovik for providing the cimel phase functions, and to A. Chapin for invaluable work in preparing the micro-pulse lidar system for field use. Funding for the measurements and analyses presented in this work was provided by the National Aeronautics and Space Administration, US National Science Foundation, Office of Naval Research, European Commission DG XII (Environment and Climate), Max Planck Society, and the National Oceanic and Atmospheric Administration.

References

Carlson, T.N., and Prospero, J.M. 1972. The large-scale movement of Saharan air outbreaks over the Northern Equatorial Atlantic. *J. Appl. Meteorol.* **11**, 283-297.

Fernald, F.G., Herman, B.M., and Reagan, J.A. 1972. Determination of aerosol height distributions by lidar. *J. Appl. Meteorol.* **11**, 482-489.

Fernald, F.G. 1984. Analysis of atmospheric lidar observations: some comments. *Appl. Optics* **23**, 652-653.

Formenti, P., Andreae, M.O., and Lelieveld, J. 1998. Saharan Dust Occurrence at a mid-tropospheric site in Tenerife. *J. Aerosol Sci.* **29**, S1047-S1048.

Formenti, P., Andreae, M.O., and Lelieveld, J. 1999. Measurements of aerosol optical depth in the North Atlantic free troposphere: results from ACE-2. *Tellus*, submitted this issue.

Heintzenberg, J., and Russell, P.B. 1999. An Overview of the ACE 2 Clear Sky Column Closure Experiment (CLEARCOLUMN). *Tellus*, submitted this issue.

Hansen, J.E., and Travis, L.D. 1974. Light scattering in planetary atmospheres. *Space Sci. Reviews* **16**, 527-610.

Holben, B.N., Eck, T.F., Slutsker, I., Tanre, D., Buis, J.P., Setzer, A., Vermote, E., Reagan, J.A., Kaufman, Y.J., Nakajima, T., Lavenu, F., Jankowiak, I., and Smirnov, A. 1998. AERONET-A federated instrument network and data archive for aerosol characterization. *Rem. Sens. Environ.* **66**, 1-16.

Karyampudi, V.M., and Carlson, T.N. 1988. Analysis and numerical simulations of the Saharan Air Layer and its effects on easterly wave distrubances. *J. Atmos. Sci.* **45**, 3102-3136.

Klett, J.D. 1985. Lidar inversion with variable backscatter/extinction ratios. *Appl. Optics* **24**, 1638-1643.

Kovalev, V.A. 1993. Lidar measurement of the vertical aerosol extinction profiles with range-dependent backscatter-to-extinction ratios. *Appl. Optics* **32**, 6053-6065.

Kovalev, V.A., and Moosmuller, H. 1994. Distortion of particulate extinction profiles measured with lidar in a two-component atmosphere. *Appl. Optics* **33**, 6499-6507.

Marenco, F., Santacesaria, V., Bais, A.F., Balis, D., di Sarra, A., Papayannis, A., and Zerefos, C. 1997. Optical properties of tropospheric aerosols determined by lidar and spectrophotometric measurements (Photochemical Activity and Solar Ultraviolet Radiation campaign). *Appl. Optics* **36**, 6875-6886.

Mishchenko, M.I., Travis, L.D., Kahn, R.A., and West, R.A. 1997. Modeling phase functions for dustlike tropospheric aerosols using a shape mixture of randomly oriented polydisperse spheroids. *J. Geophys. Res.* **102**, 16831-16847.

Prospero, J.M., Schmitt, R., Cuevas, E., Savoie, D., Graustein, W., Turekian, K., Volz-Thomas, A., Oltmans, S., Levy, H., and Diaz, A. 1995. Temporal variability of ozone and aerosols in the free troposphere over the Eastern North Atlantic. *Geophys. Res. Letts.* **22**, 2925-2928.

Raes, F., Van Dingenen, R., Cuevas, E., Van Velthoven, P.F.J., and Prospero, J.M. 1997. Observations of aerosols in the free troposphere and marine boundary layer of the subtropical Northeast Atlantic: Discussion of processes determining their size distribution. *J. Geophys. Res.* **102**, 21315-21328.

Raes, F., Bates, T., Verver, G., Vogelenzang, D., and Van Liedekerke, M. 1999. The Second Aerosol Characterization Experiment (ACE-2): introduction, meteorological overview and main results. *Tellus*, submitted this issue.

Sasano, Y., Browell, E.V., and Ismail, S. 1985. Error caused by using a constant extinction/backscattering ratio in the lidar solution. *Appl. Optics* **24**, 3929-3932.

Schmid, B., Livingston, J.M., Russell, P.B., Durkee, P.A., Jonsson, H.H., Collins, D.R., Flagan, R.C., Seinfeld, J.H., Gassó, S., Hegg, D.A., Öström, E., Noone, K.J., Welton, E.J., Voss, K.J., Gordon, H.R., Formenti, P., and Andreae, M.O. 1999. Clear sky closure studies of lower tropospheric aerosol and water vapor during ACE-2 using airborne sunphotometer, airborne in-situ, space-borne, and ground-based measurements. *Tellus*, submitted this issue.

Smirnov, A., Holben, B.N., Slutsker, I., Welton, E.J., and Formenti, P. 1998. Optical Properties of Saharan Dust During ACE 2. *J. Geophys. Res.* **103**, 28079-28092.

Spinhirne, J.D. 1993. Micro pulse lidar. *IEEE Trans. Geosci. Remote Sens.* **31**, 48-55.

Spinhirne, J.D., Rall, J., and Scott, V.S. 1995. Compact eye-safe lidar systems. *Rev. Laser Eng.* **23**, 26-32.

Welton, E.J. 1998. Measurements of Aerosol Optical Properties over the Ocean Using Sunphotometry and Lidar. *Ph.D. Dissertation.* University of Miami, Coral Gables, 1-150.

List of Figure Captions

Figure 1. Schematic diagram of the micro-pulse lidar system (not to scale).

Figure 2a. Aerosol total mass concentrations ($\mu g\ m^{-3}$) measured during the early mornings of June 29 and July 15 1997 at IZO.

Figure 2b. Aerosol extinction coefficients (m^{-1}) measured during the early mornings of June 29 and July 15 1997 at IZO.

Figure 3a. Overlap functions, O(z), calculated on June 29 and July 15 1997.

Figure 3b. Afterpulse functions, A(z), calculated on June 29 and July 15 1997.

Figure 4. The measured MPL signal, a calculated Rayleigh lidar signal, and the final calibrated MPL signal are shown for 00:00 GMT on June 30, 1997.

Figure 5. Three-day attenuated backscatter signal (ABS) (m sr)$^{-1}$ time series from June 29 through July 1, 1997. Each major tickmark separates the days, and each minor tickmark is one hour (GMT).

Figure 6a. Attenuated Backscatter Signals (m sr)$^{-1}$ on June 29, 1997. Each profile is a 15 minute average, starting 15 minutes prior to the time shown. The 06:15 GMT (before sunrise) profile shows no evidence of upslope aerosols and is representative of a clean, Rayleigh-only lidar profile. Upslope aerosols are visible up to approximately 5 km for the 07:15 GMT and 10:15 GMT profiles (during daytime).

Figure 6b. Attenuated Backscatter Signals (m sr)$^{-1}$ on June 29, 1997. Each profile is a 15 minute average, starting 15 minutes prior to the time shown. Upslope aerosols are visible up to approximately 5 km for the 17:15 GMT and 19:15 GMT profiles (during daytime). The 22:15 GMT (after sunset) profile shows no evidence of upslope aerosols and is representative of a clean, Rayleigh-only lidar profile.

Figure 7a. Lidar aerosol extinction coefficient (m^{-1}) profiles at 08:15, 10:15, 17:15, and 18:15 GMT on June 29, 1997. The columnar AOD for each profile is 0.017, 0.018, 0.015, and 0.014 respectively. The calculated columnar backscatter-extinction ratios (sr^{-1}) for each profile are 0.018, 0.038, 0.031, and 0.017 respectively. The Rayleigh extinction coefficient profile is shown for comparison. The average aerosol extinction coefficient measured by the IZO nephelometer from 07:00 to 19:00 GMT is also shown.

Figure 7b. Lidar aerosol optical depth (AOD) profiles at 08:15, 10:15, 17:15, and 18:15 GMT on June 29, 1997. The columnar AOD for each profile is 0.017, 0.018, 0.015, and 0.014 respectively. The calculated columnar backscatter-extinction ratios (sr^{-1}) for each profile are 0.018, 0.038, 0.031, and 0.017 respectively. The average AOD measured by the Teide shadowband is also shown.

Figure 8. Horizontal lidar profiles of the natural logarithm of the attenuated backscatter coefficient $(m\ sr)^{-1}$. A 15 minute average horizontal profile at 10:45 GMT on June 29 is shown along with a calculated Rayleigh horizontal profile for the IZO altitude.

Figure 9. Three-day attenuated backscatter signal (ABS) $(m\ sr)^{-1}$ time series from July 16 through July 18, 1997. Each major tickmark separates the days, and each minor tickmark is one hour (GMT).

Figure 10. Lidar aerosol extinction coefficient (m^{-1}) profiles at 08:15, 10:15, 17:15, and 18:45 GMT on July 17, 1997. The columnar AOD for each profile is 0.161, 0.205, 0.226, and 0.217 respectively. The calculated columnar backscatter-extinction ratios (sr^{-1}) for each profile are 0.026, 0.048, 0.073, and 0.027 respectively. The Rayleigh extinction coefficient profile is shown for comparison.

Figure 11a. Lidar aerosol extinction coefficient (m^{-1}) profiles at 10:15 and 18:45 GMT on July 17, 1997. The columnar AOD for each profile is 0.205 and 0.217 respectively. The calculated columnar backscatter-extinction ratios (sr^{-1}) for each profile are 0.048 and 0.027 respectively. The average aerosol extinction coefficients measured by the IZO nephelometer from 07:00 to 18:00 GMT (daytime) and after 18:00 GMT are also shown.

Figure 11b. Lidar aerosol optical depth (AOD) profile at 18:45 GMT on July 17, 1997. The columnar AOD is 0.217 and the calculated columnar backscatter-extinction ratio (sr^{-1}) is 0.027. The AOD profile measured with AATS-14 from 18:30 to 18:45 GMT, and the AOD measured by the IZO cimel and the Teide shadowband, are also shown.

Figure 12. Horizontal lidar profiles of the natural logarithm of the attenuated backscatter coefficient $(m\ sr)^{-1}$. A 15 minute average horizontal profile at 11:15 GMT and a 5 minute average horizontal profile at 18:50 GMT on July 17 are shown along with a calculated Rayleigh horizontal profile for the IZO altitude.

Figure 13. Schematic representation of the lidar inversion algorithm.

Figure 1

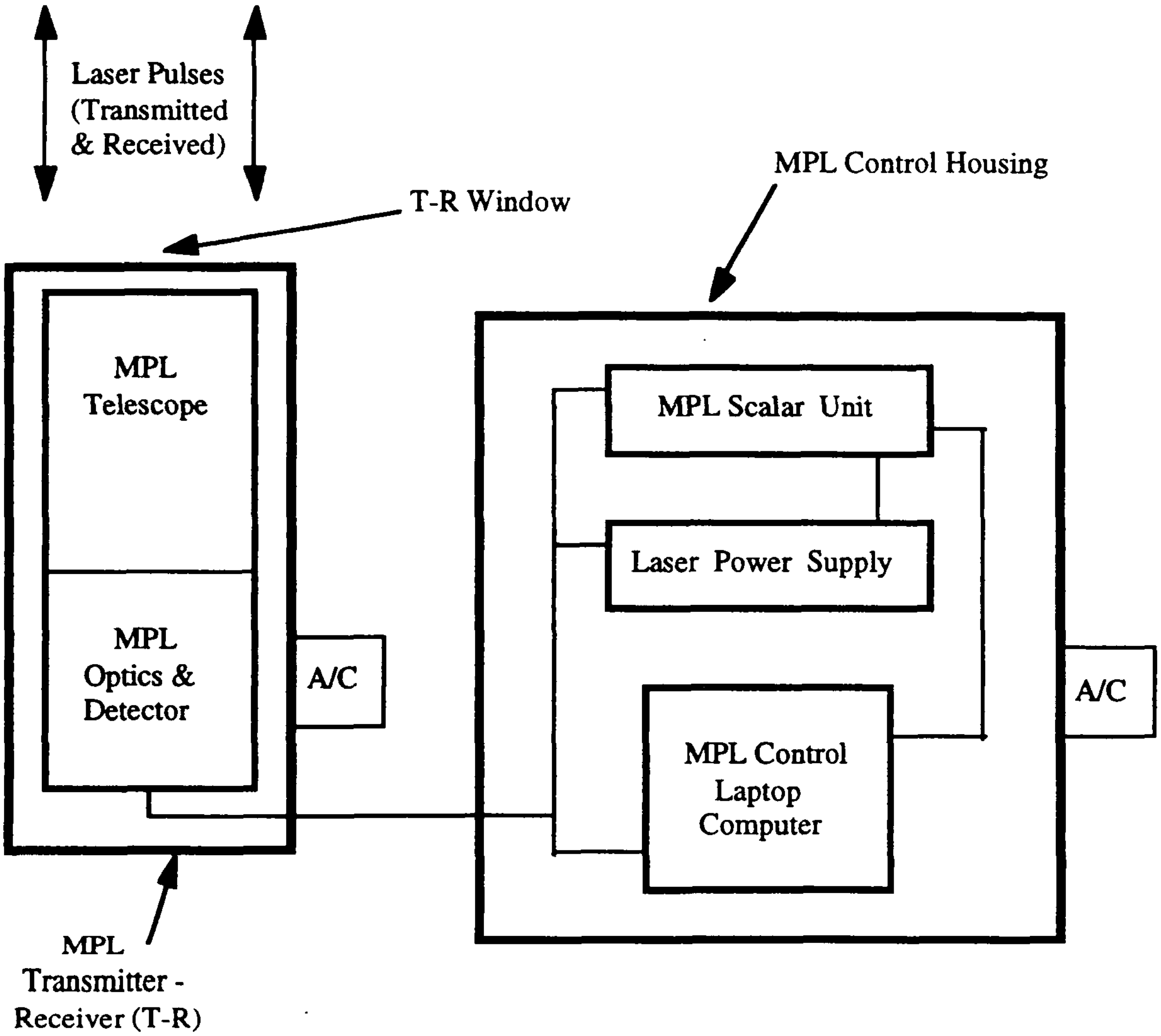

Figure 1. Schematic diagram of the micro-pulse lidar system (not to scale).

Figure 2a

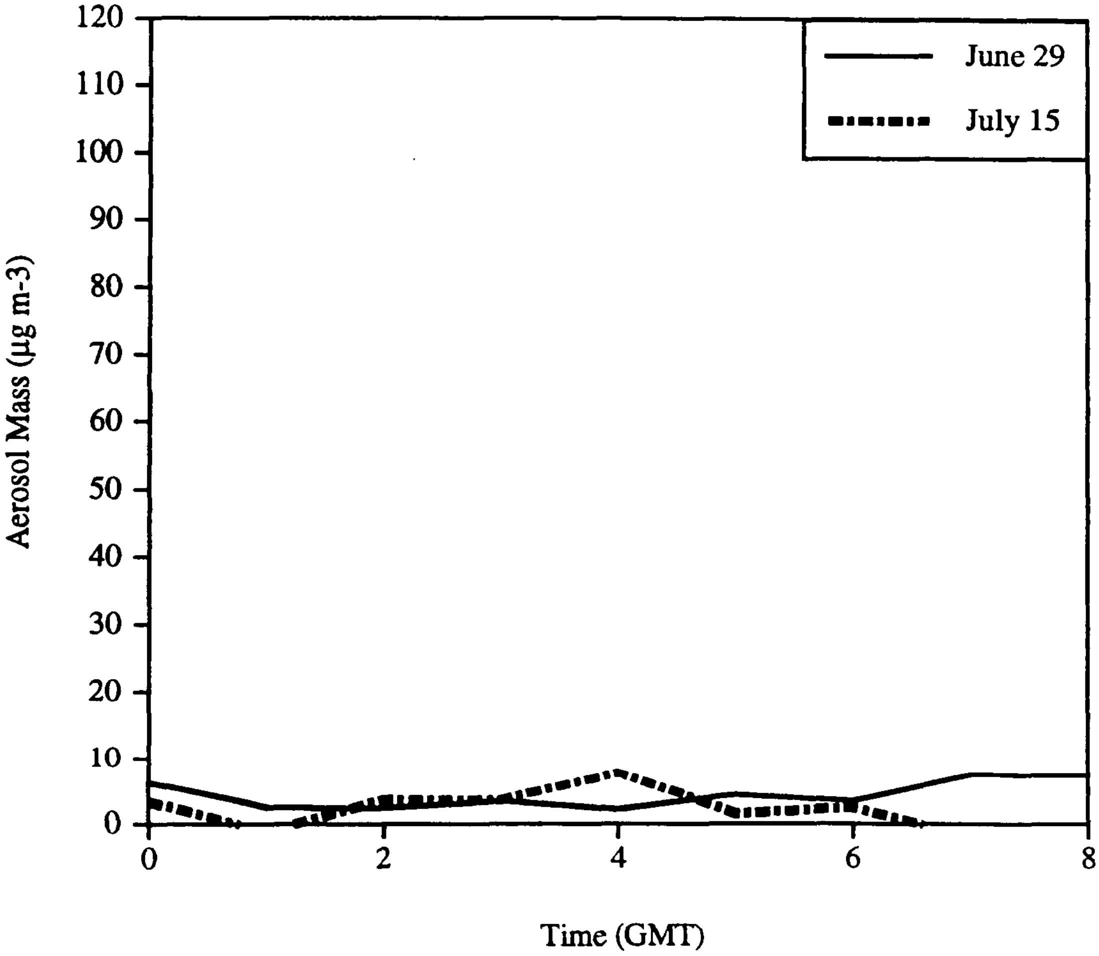

Figure 2a. Aerosol total mass concentrations measured during the early mornings of June 29 and July 15 1997 at IZO.

Figure 2b

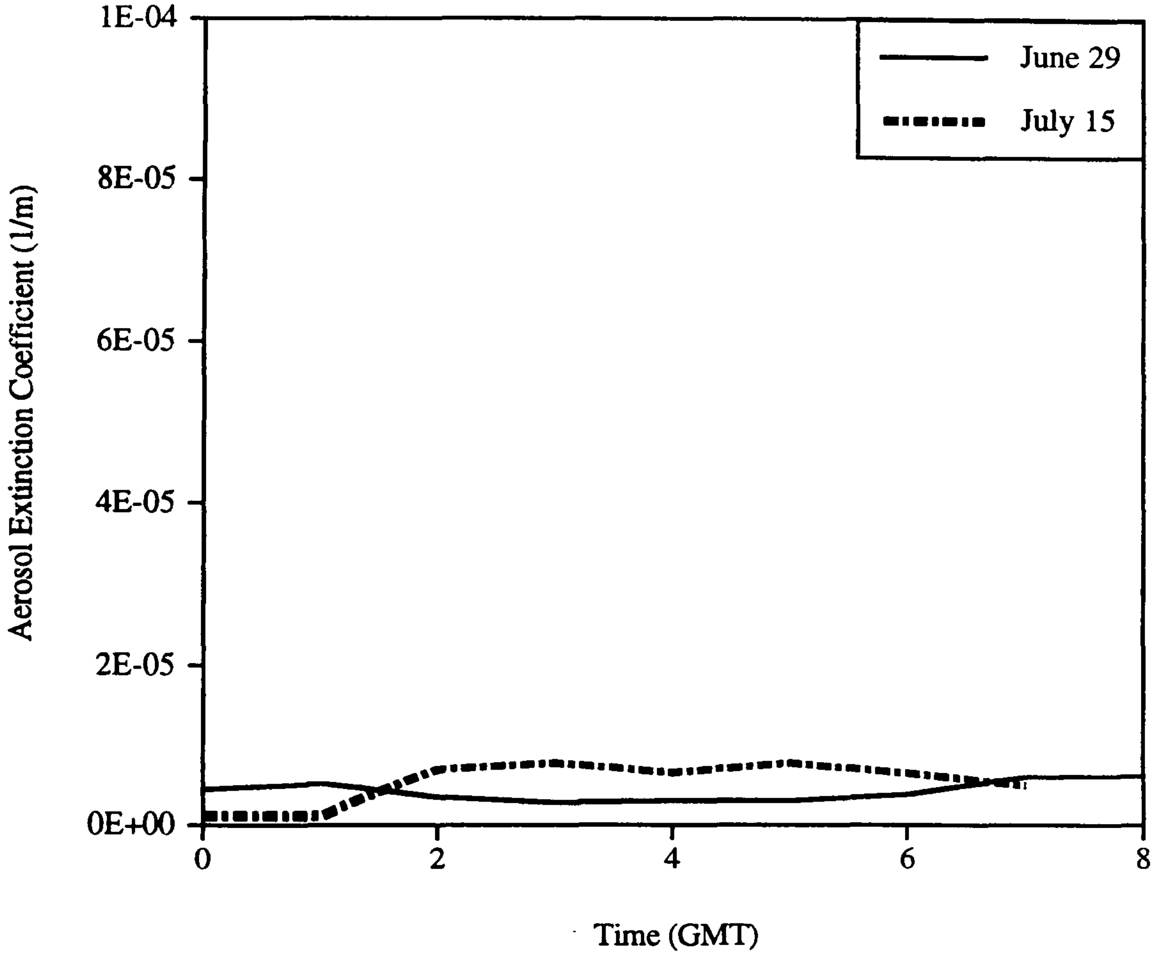

Figure 2b. Aerosol extinction coefficients measured during the early mornings of June 29 and July 15 1997 at IZO.

Figure 3a

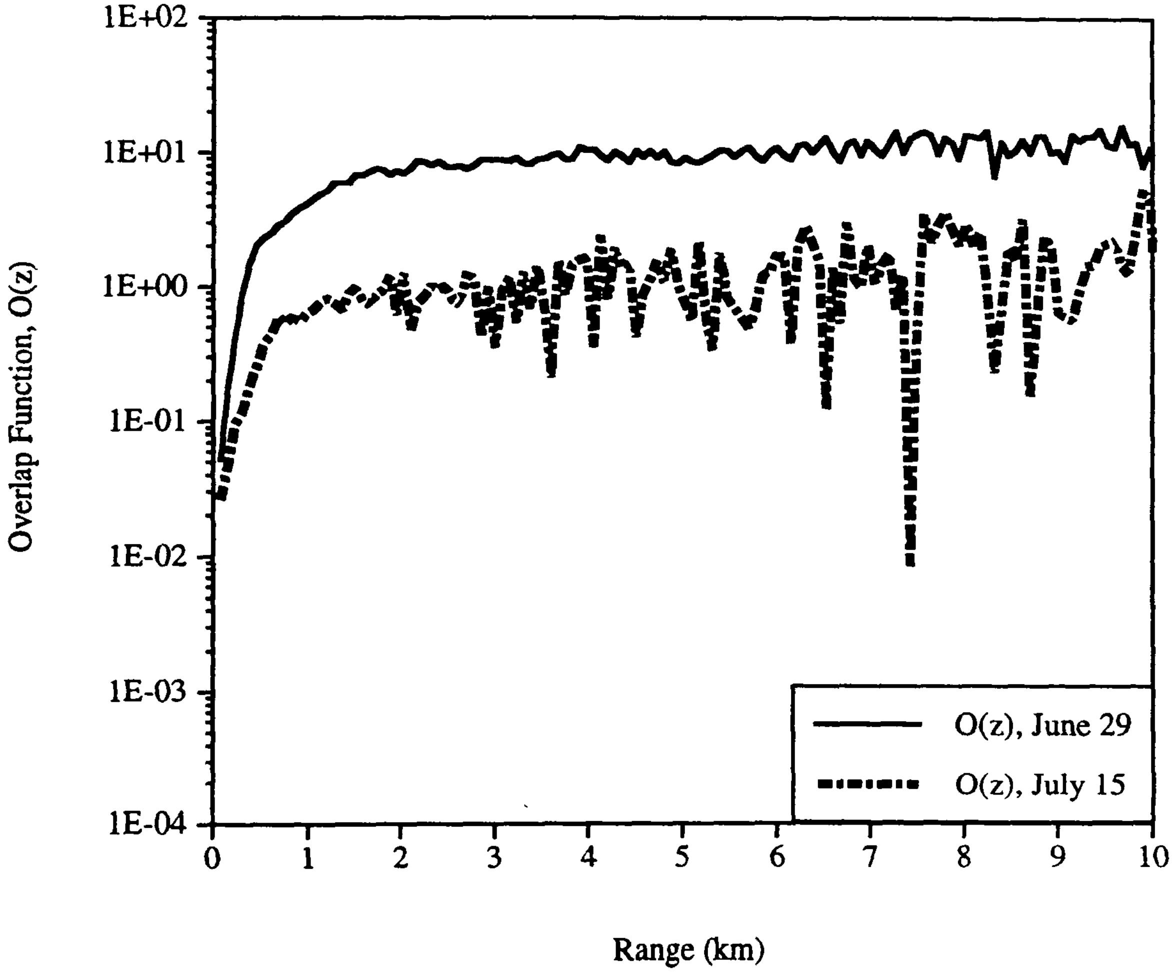

Figure 3a. Overlap functions, O(z), calculated on June 29 and July 15 1997.

Figure 3b

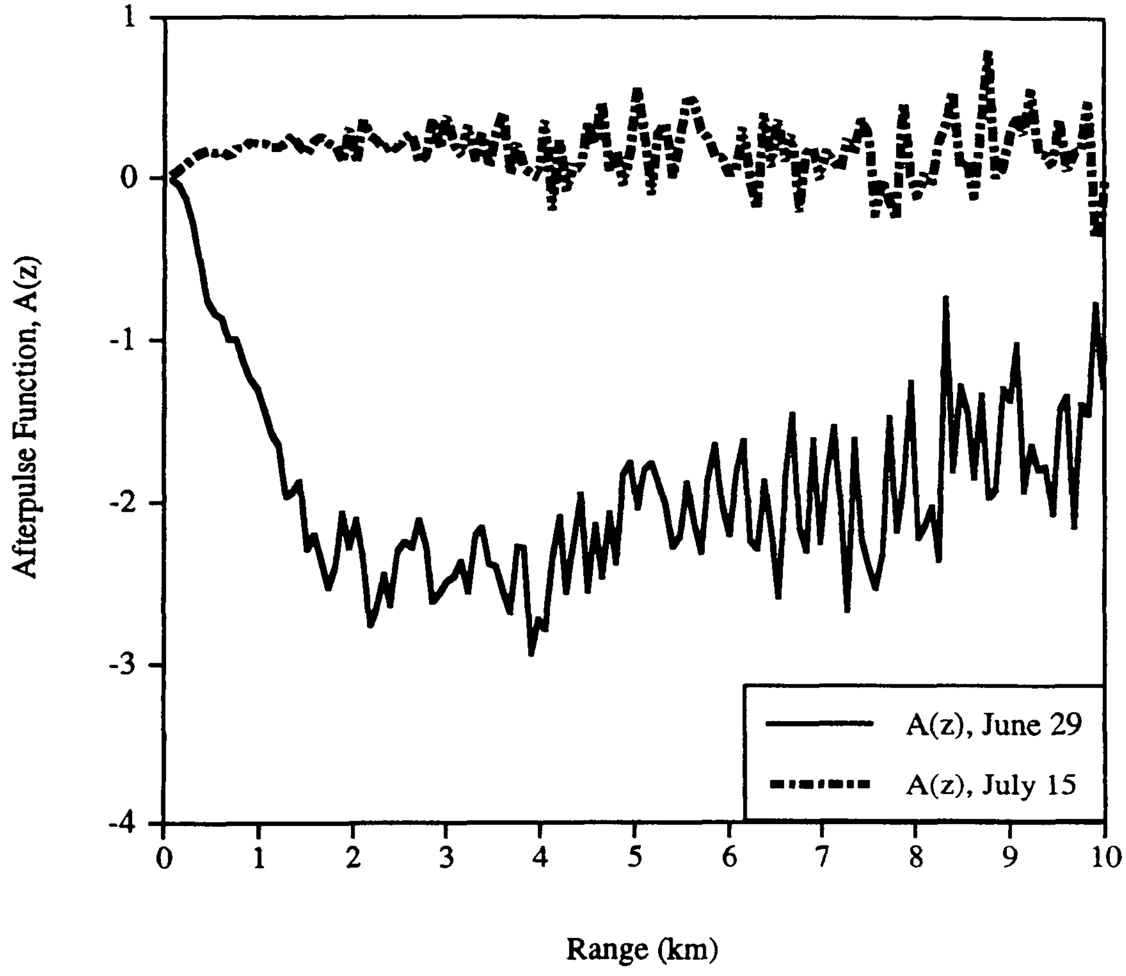

Figure 3b. Afterpulse functions, A(z), calculated on June 29 and July 15 1997.

Figure 4

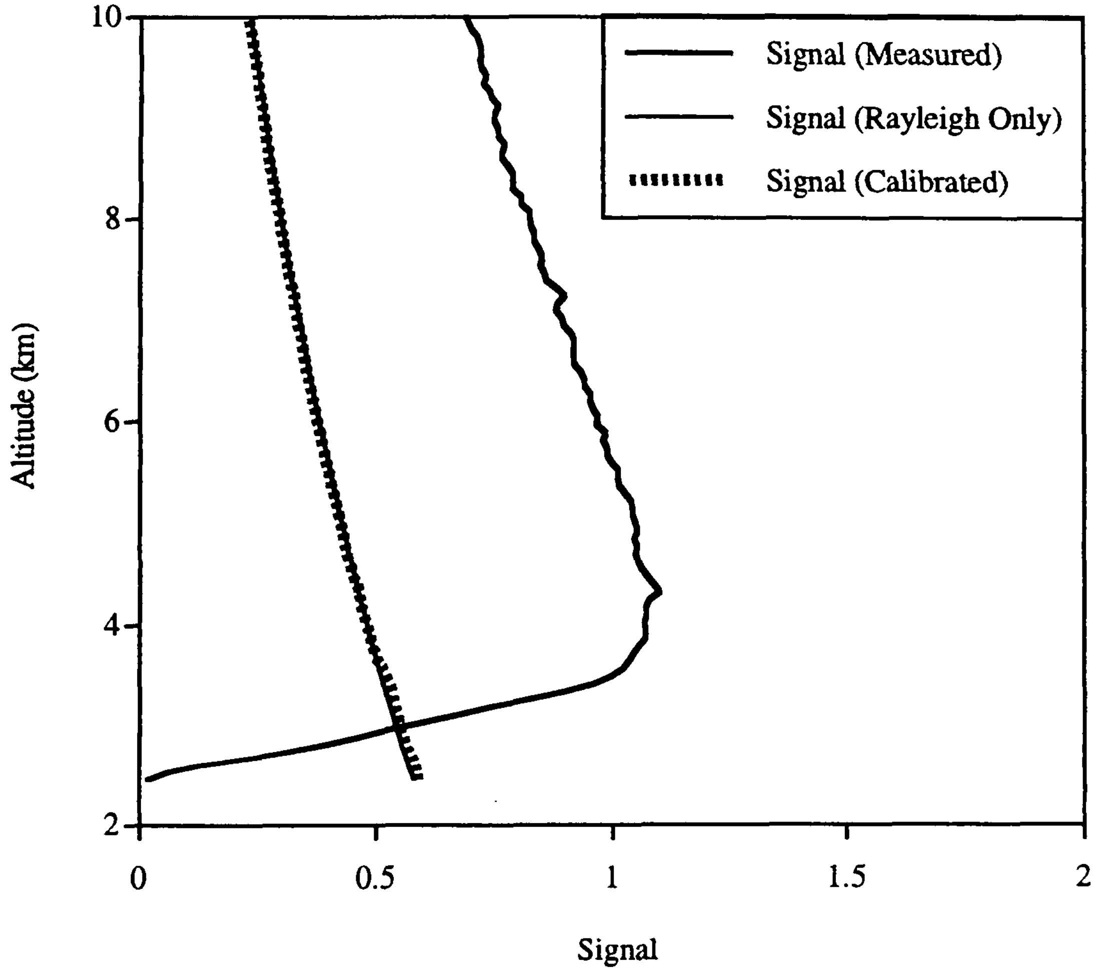

Figure 4. The measured MPL signal, a calculated Rayleigh lidar signal, and the final calibrated MPL signal are shown for 00:00 GMT on June 30, 1997.

Figure 5

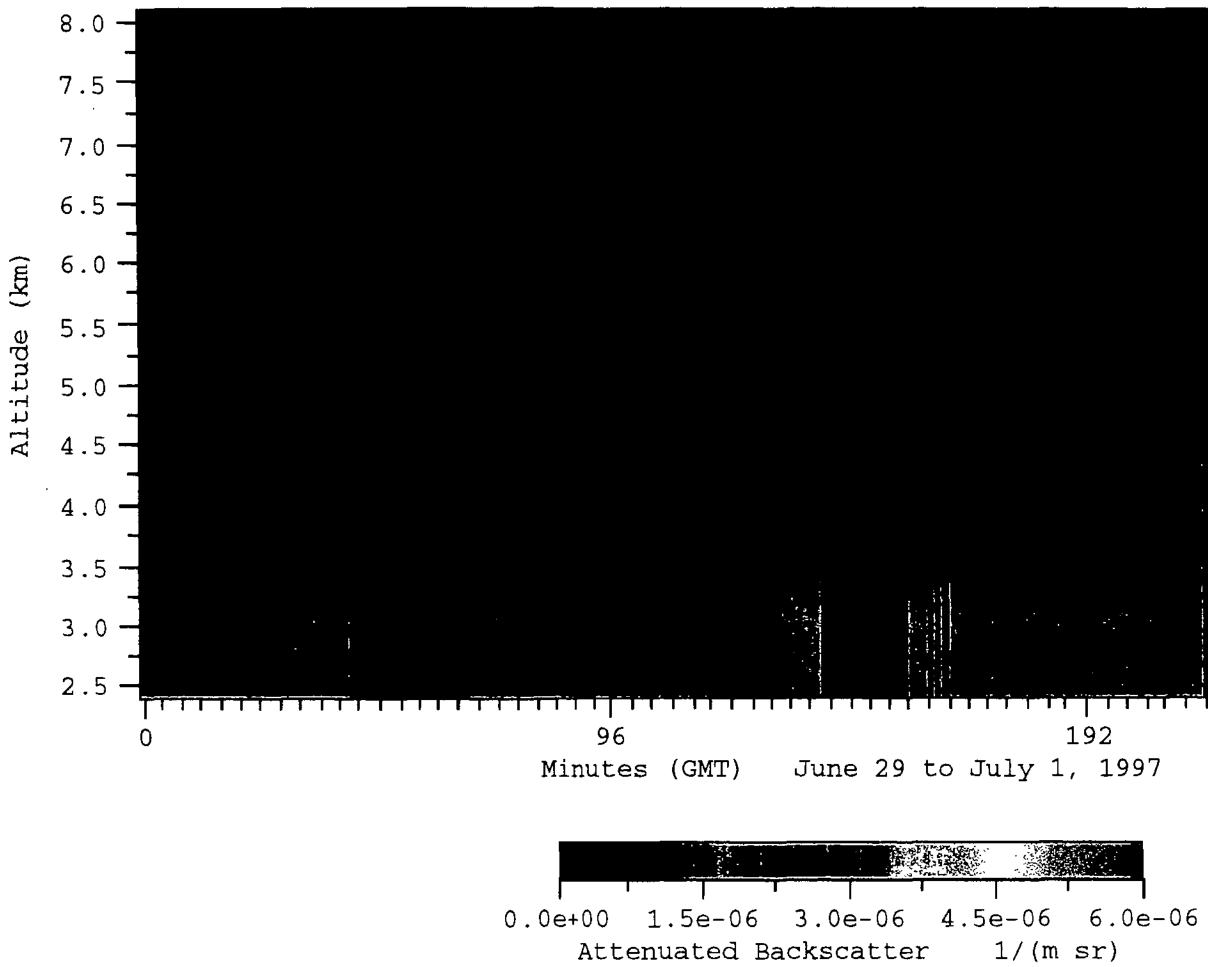

Figure 5. Three-day attenuated backscatter signal (ABS) $(m\ sr)^{-1}$ time series from June 29 through July 1, 1997. Each major tickmark separates the days, and each minor tickmark is one hour (GMT).

Figure 6a

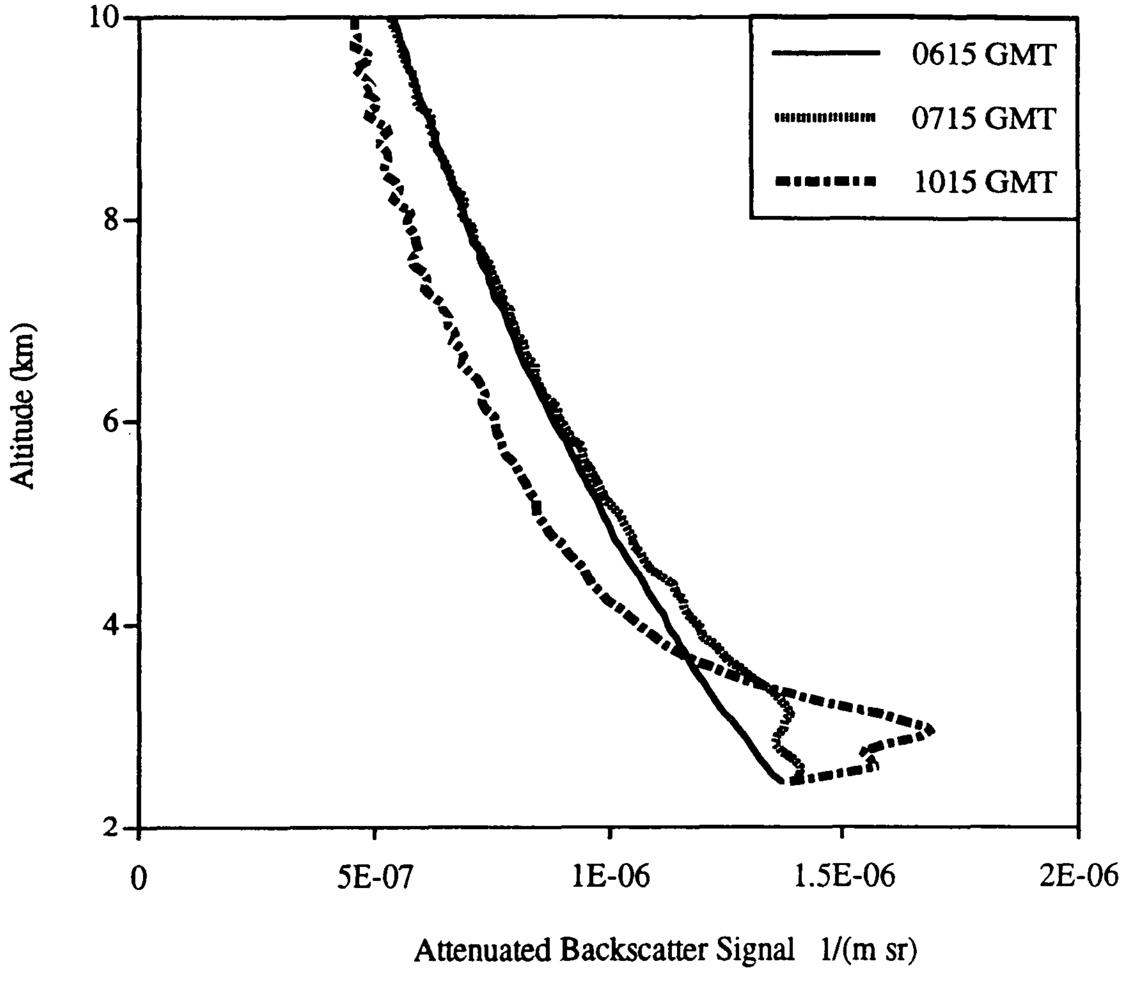

Figure 6a. Attenuated Backscatter Signals, 1/(m sr), on June 29, 1997. Each profile is a 15 minute average, starting 15 minutes prior to the time shown. The 06:15 GMT (before sunrise) profile shows no evidence of upslope aerosols and is representative of a clean, Rayleigh-only lidar profile. Upslope aerosols are visible up to approximately 5 km for the 07:15 GMT and 10:15 GMT profiles (during daytime).

Figure 6b

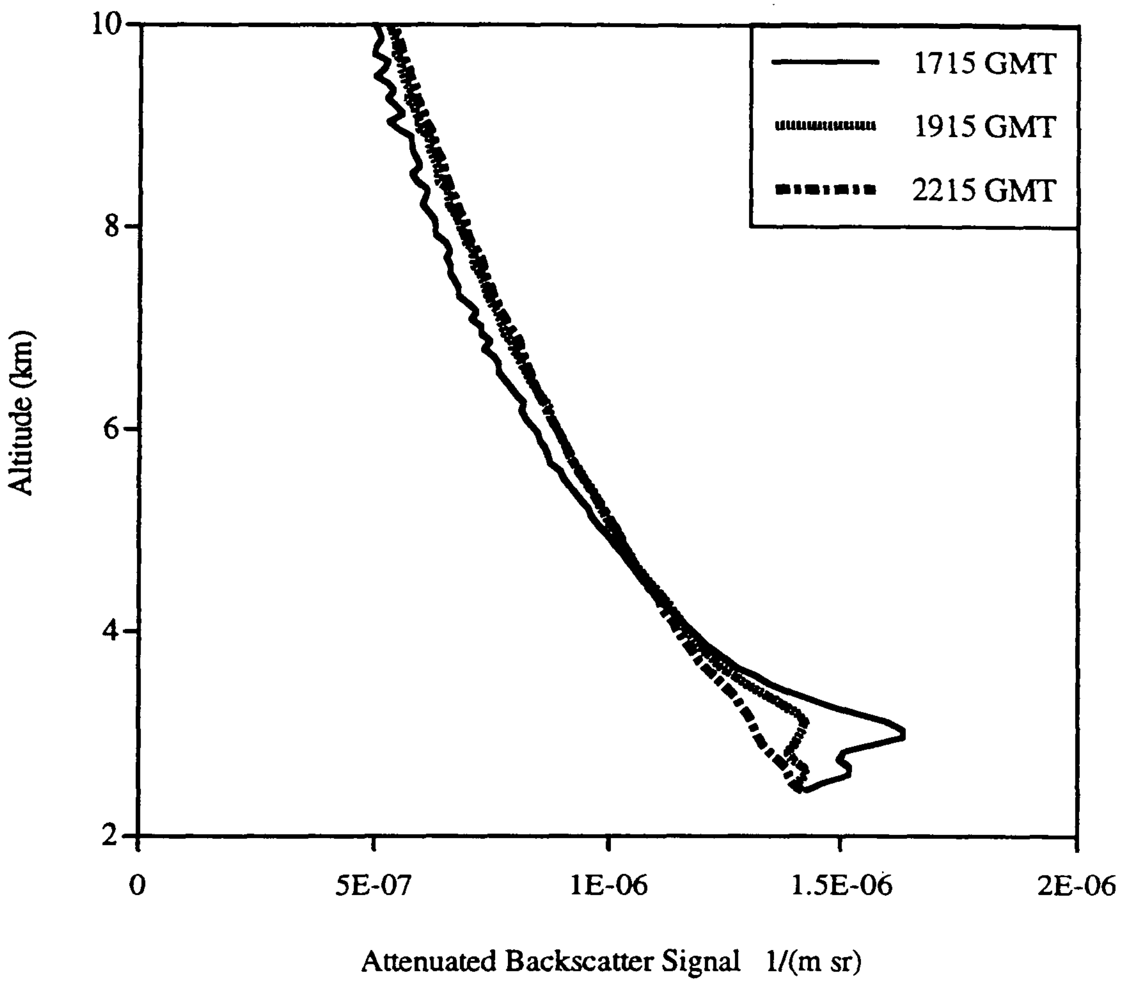

Figure 6b. Attenuated Backscatter Signals, 1/(m sr), on June 29, 1997. Each profile is a 15 minute average, starting 15 minutes prior to the time shown. Upslope aerosols are visible up to approximately 5 km for the 17:15 GMT and 19:15 GMT profiles (during daytime). The 22:15 GMT (after sunset) profile shows no evidence of upslope aerosols and is representative of a clean, Rayleigh-only lidar profile.

Figure 7a

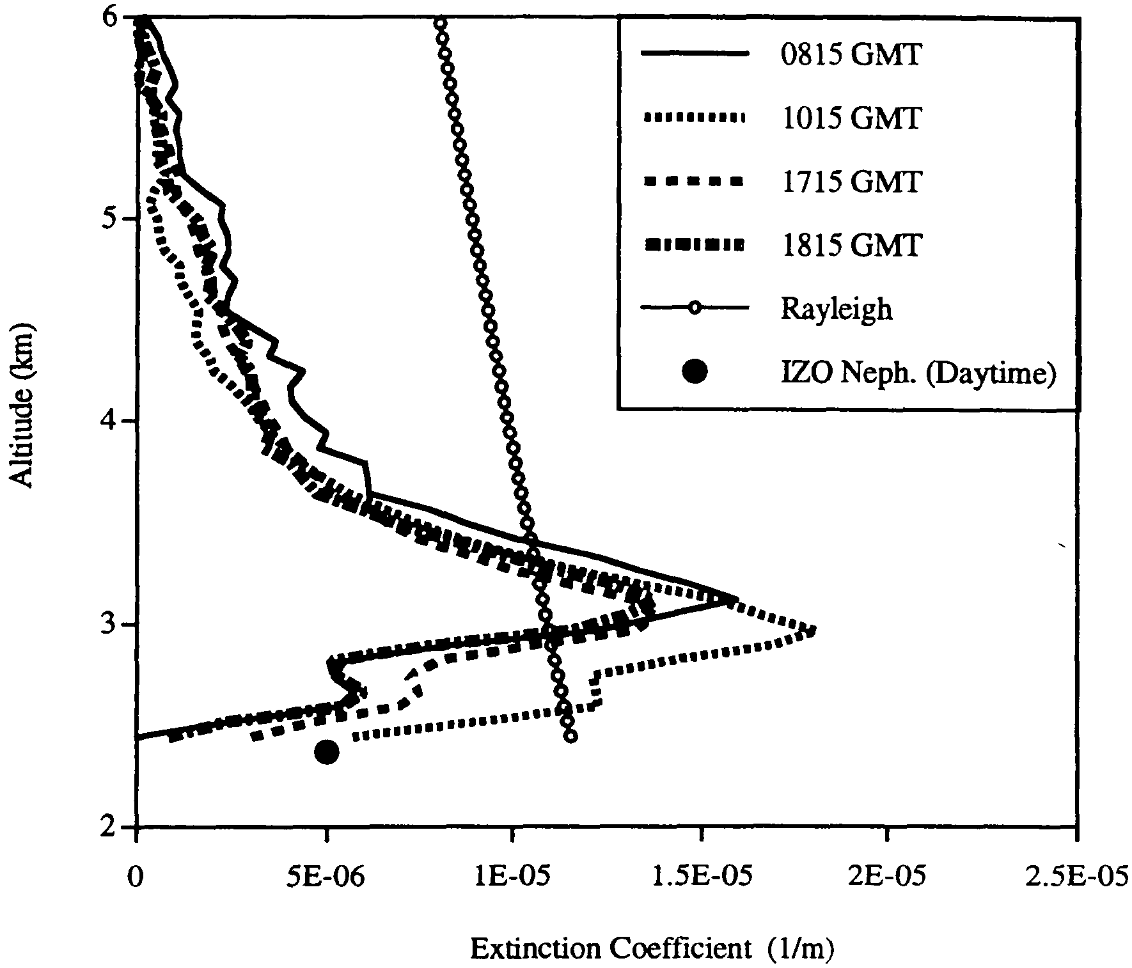

Figure 7a. Lidar aerosol extinction coefficient (1/m) profiles at 08:15, 10:15, 17:15, and 18:15 GMT on June 29, 1997. The columnar AOD for each profile is 0.017, 0.018, 0.015, and 0.014 respectively. The calculated columnar backscatter-extinction ratios (1/sr) for each profile are 0.018, 0.038, 0.031, and 0.017 respectively. The Rayleigh extinction coefficient profile is shown for comparison. The average aerosol extinction coefficient measured by the IZO nephelometer from 07:00 to 19:00 GMT is also shown.

Figure 7b

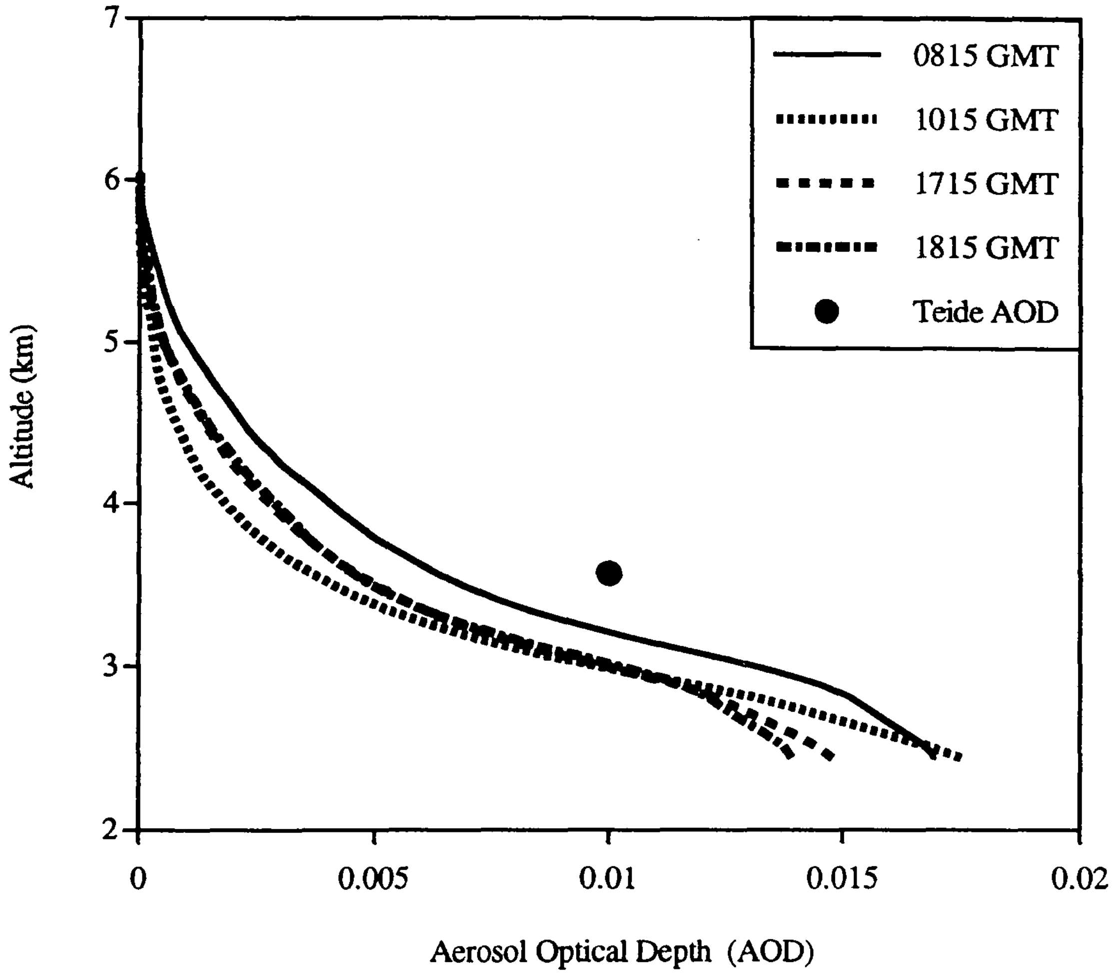

Figure 7b. Lidar aerosol optical depth (AOD) profiles at 08:15, 10:15, 17:15, and 18:15 GMT on June 29, 1997. The columnar AOD for each profile is 0.017, 0.018, 0.015, and 0.014 respectively. The calculated columnar backscatter-extinction ratios (1/sr) for each profile are 0.018, 0.038, 0.031, and 0.017 respectively. The average AOD measured by the Teide shadowband is also shown.

Figure 8

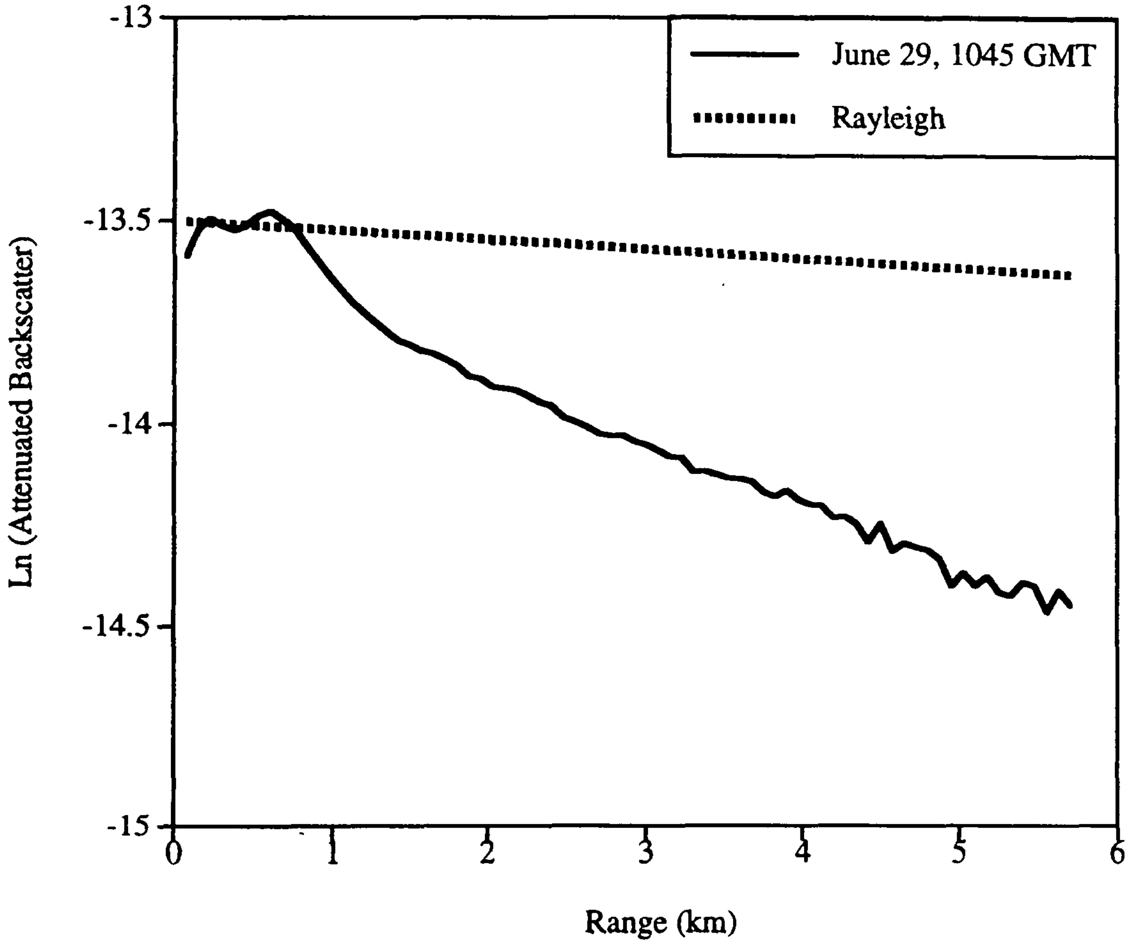

Figure 8. Horizontal lidar profiles of the natural logarithm of the attenuated backscatter coefficient, 1(m sr). A 15 minute average horizontal profile at 10:45 GMT on June 29 is shown along with a calculated Rayleigh horizontal profile for the IZO altitude.

Figure 9

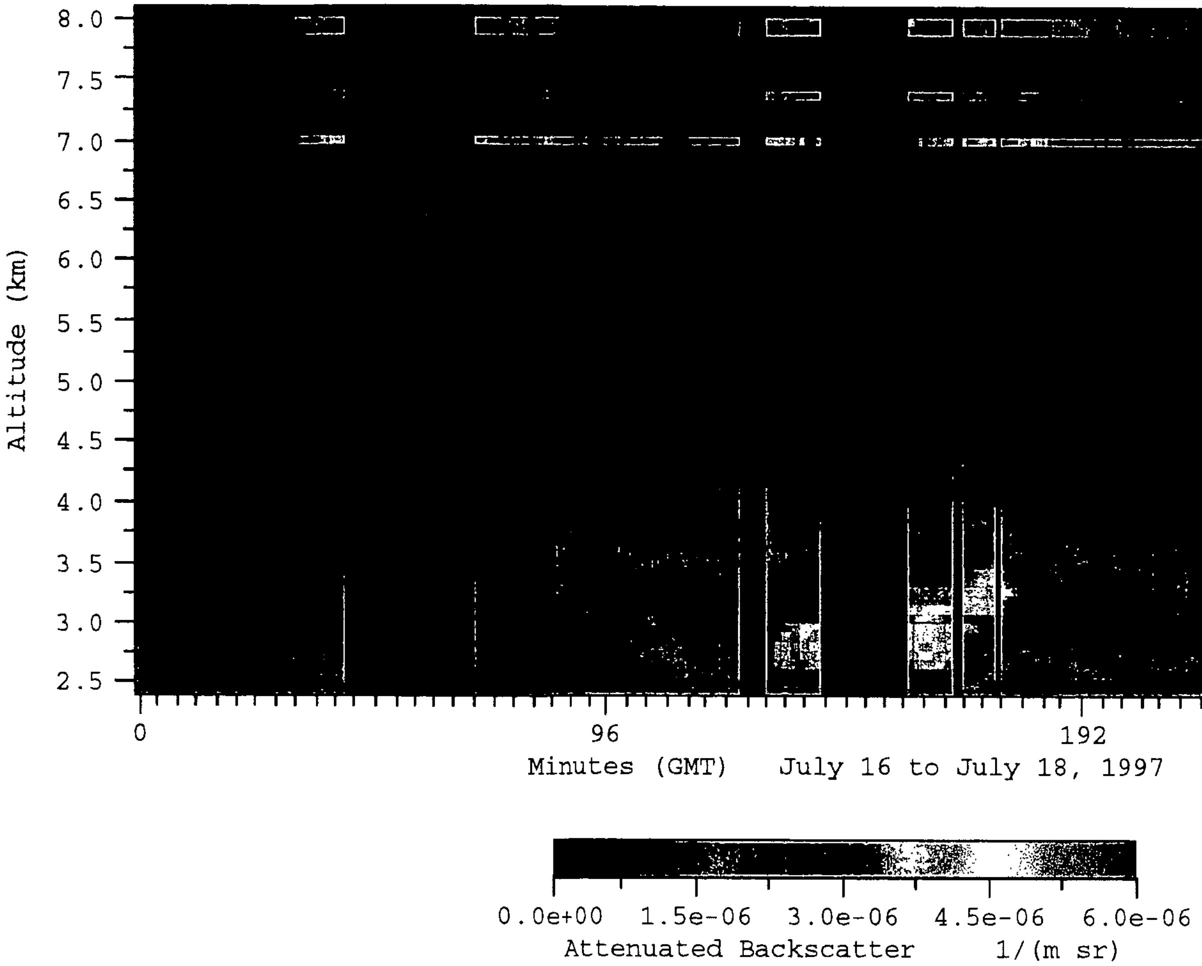

Figure 9. Three-day attenuated backscatter signal (ABS) $(m\ sr)^{-1}$ time series from July 16 through July 18, 1997. Each major tickmark separates the days, and each minor tickmark is one hour (GMT).

Figure 10

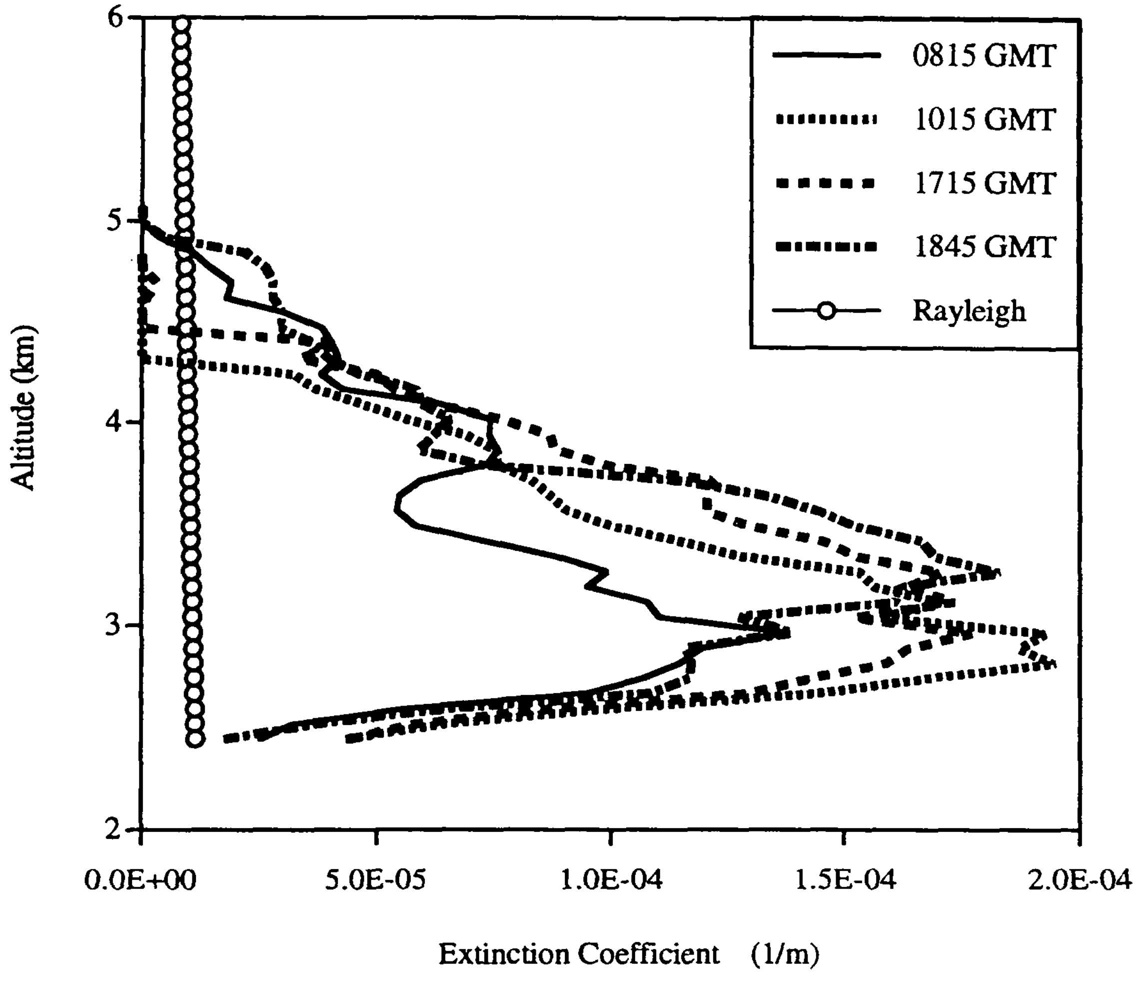

Figure 10. Lidar aerosol extinction coefficient (1/m) profiles at 08:15, 10:15, 17:15, and 18:45 GMT on July 17, 1997. The columnar AOD for each profile is 0.161, 0.205, 0.226, and 0.217 respectively. The calculated columnar backscatter-extinction ratios (1/sr) for each profile are 0.026, 0.048, 0.073, and 0.027 respectively. The Rayleigh extinction coefficient profile is shown for comparison.

Figure 11a

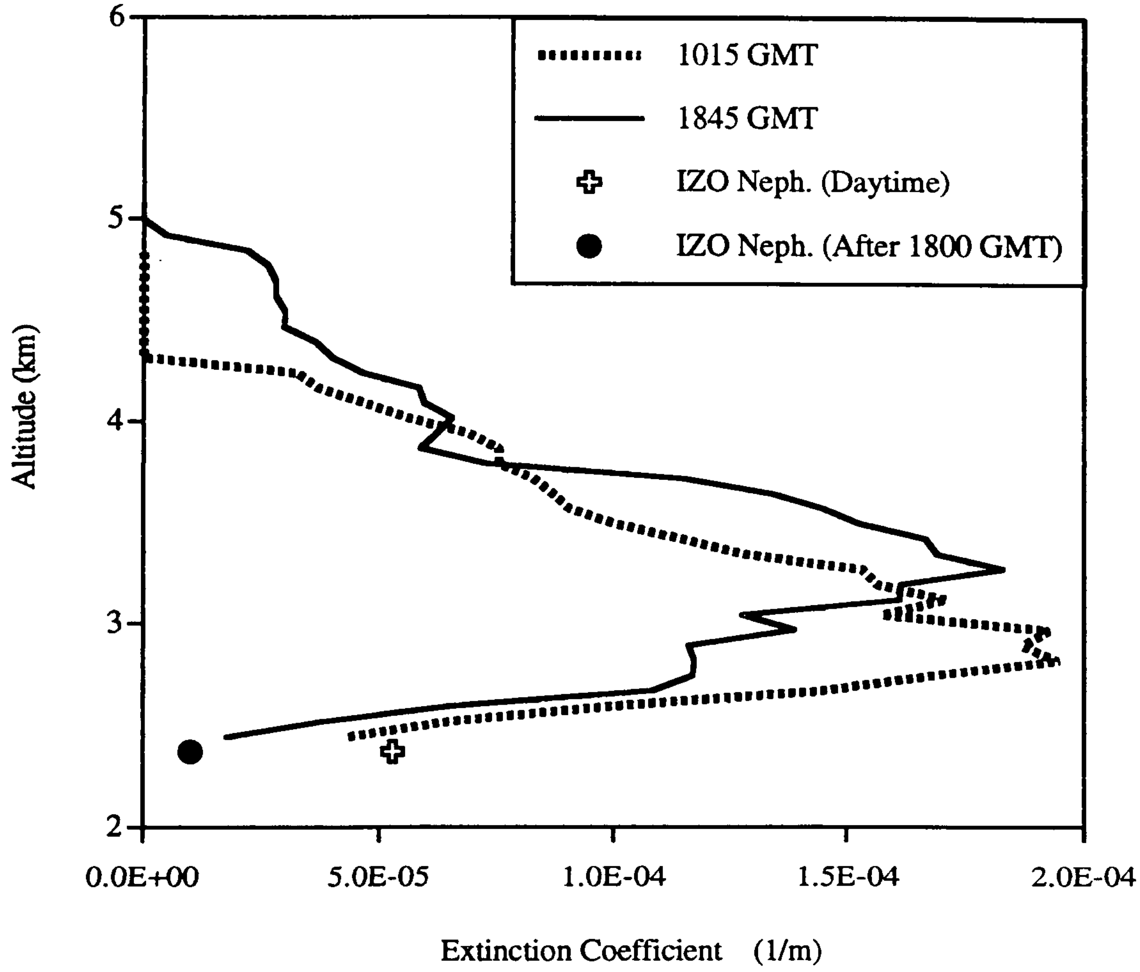

Figure 11a. Lidar aerosol extinction coefficient (1/m) profiles at 10:15 and 18:45 GMT on July 17, 1997. The columnar AOD for each profile is 0.205 and 0.217 respectively. The calculated columnar backscatter-extinction ratios (1/sr) for each profile are 0.048 and 0.027 respectively. The average aerosol extinction coefficients measured by the IZO nephelometer from 07:00 to 18:00 GMT (daytime) and after 18:00 GMT are also shown.

Figure 11b

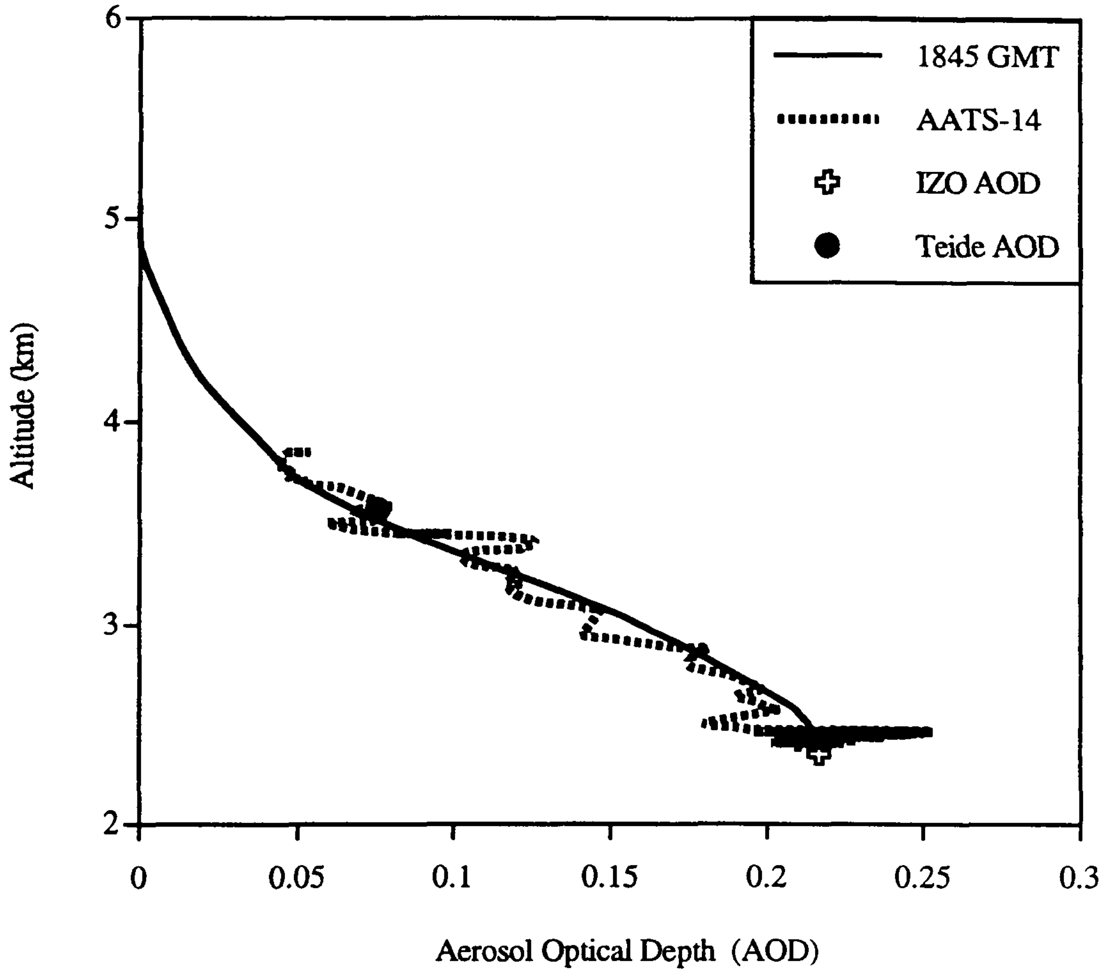

Figure 11b. Lidar aerosol optical depth (AOD) profile at 18:45 GMT on July 17, 1997. The columnar AOD is 0.217 and the calculated columnar backscatter-extinction ratio (1/sr) is 0.027. The AOD profile measured with AATS-14 from 18:30 to 18:45 GMT, and the AOD measured by the IZO cimel and the Teide shadowband, are also shown.

Figure 12

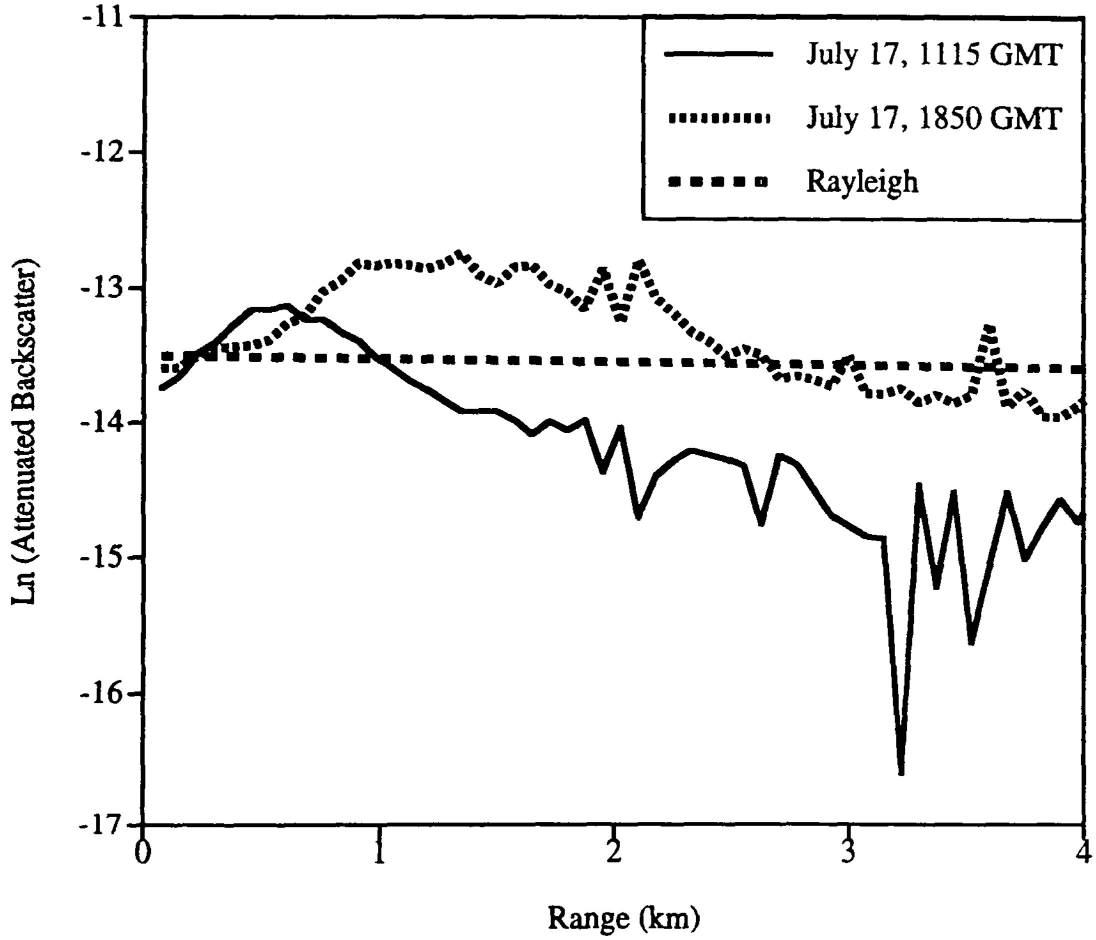

Figure 12. Horizontal lidar profiles of the natural logarithm of the attenuated backscatter coefficient, 1(m sr). A 15 minute average horizontal profile at 11:15 GMT and a 5 minute average horizontal profile at 18:50 GMT on July 17 are shown along with a calculated Rayleigh horizontal profile for the IZO altitude.

Figure 13

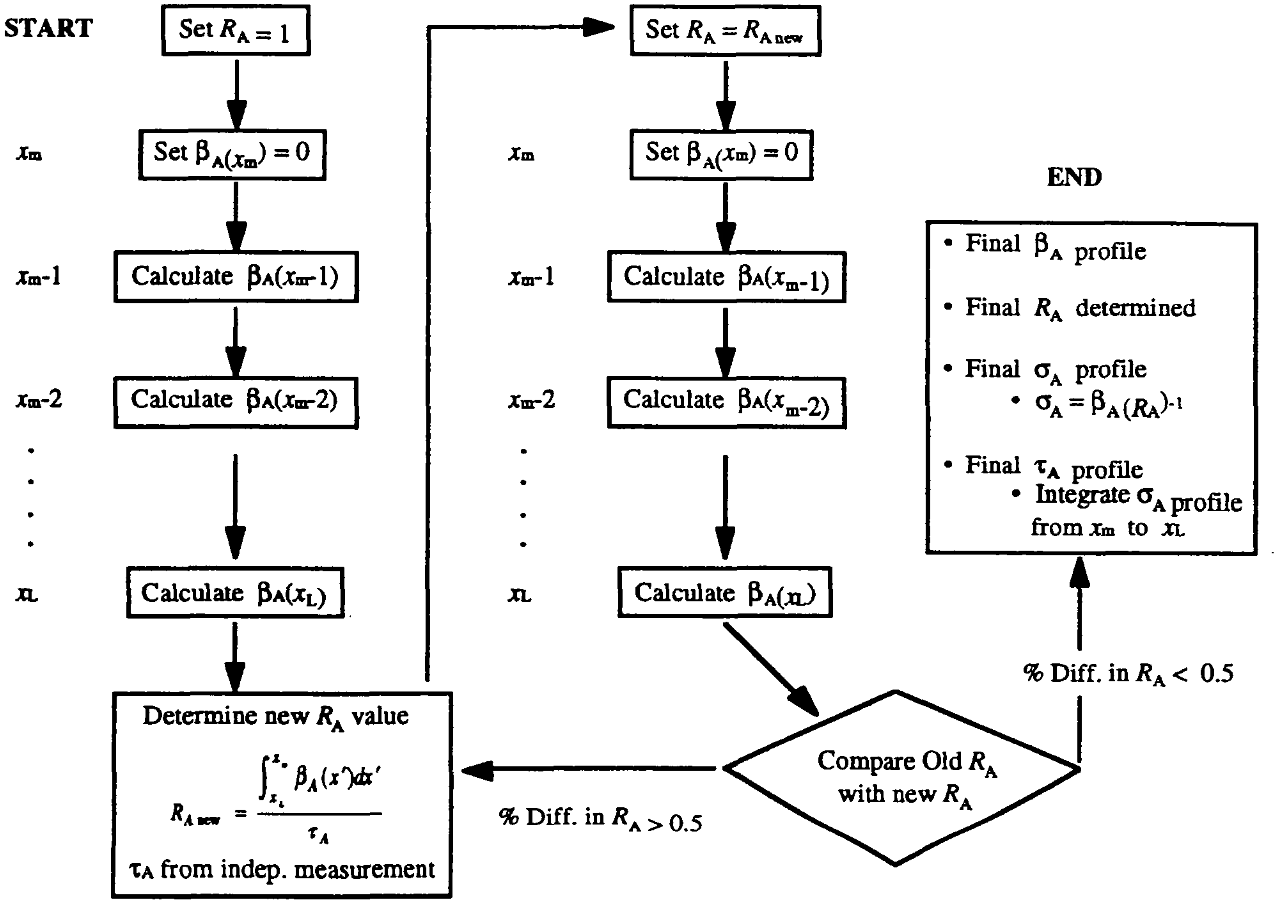

Figure 13. Schematic representation of the lidar inversion algorithm.